Grey Wolf Optimization Algorithm Based Maximum Power Point Tracking, and Voltage Control of Stand-alone PV System with Storage Device: Application to Multi-Service Access Node

Keneni Alemayehu Aga

A Thesis Submitted to

The Department of Electrical Power and Control Engineering

School of Electrical Engineering and Computing

Presented in Partial Fulfillment of the Requirement for the Degree of Master's in Electrical Power and Control Engineering (Control Engineering)

Office of Graduate Studies

Adama Science and Technology University

June, 2024

Adama, Ethiopia

Grey Wolf Optimization Algorithm Based Maximum Power Point Tracking, and Voltage Control of Stand-alone PV System with Storage Device: Application to Multi-Service Access Node

Keneni Alemayehu Aga

Advisor: Dr. Endalew Ayenew

A Thesis Submitted to

The Department of Electrical Power and Control Engineering

School of Electrical Engineering and Computing

Presented in Partial Fulfillment of the Requirement for the Degree of Master's in Electrical Power and Control Engineering (Control Engineering)

Office of Graduate Studies

Adama Science and Technology University

June, 2024

Adama, Ethiopia

DECLARATION

I declare that this thesis entitled "**Grey Wolf Optimization Algorithm Based Maximum Power Point Tracking, and Voltage Control of Stand-alone PV System with Storage Device: Application to Multi-Service Access Node**" is my work and has not been submitted to any university for a similar purpose. The reference used in this proposal are duly recognized by appropriate citations.

Keneni Alemayehu		
Name of Student	Signature	Date

RECOMMENDATION

I, the advisor of this thesis, hereby certify that I have read the revised version of the thesis entitled "**Grey Wolf Optimization Algorithm Based Maximum Power Point Tracking, and Voltage Control of Stand-alone PV System with Storage Device: Application to Multi-Service Access Node** prepared under my guidance by **Keneni Alemayehu** submitted in partial fulfillment of the requirements for the degree of Mater's of Science in Electrical Power and Control Engineering (Control Engineering). Therefore, I recommend the submission of revised version of the thesis to the department following the applicable procedures.

Dr. Endalew Ayenew		
Major Advisor	Signature	Date

APPROVAL PAGE

I, the advisor of the thesis entitled "**Grey Wolf Optimization Algorithm Based Maximum Power Point Tracking, and Voltage Control of Stand-alone PV System with Storage Device: Application to Multi-Service Access Node**" and developed by **Keneni Alemayehu**, hereby certify that the recommendation and suggestions made by the board of examiners are appropriately incorporated into the final version of the thesis.

Dr. Endalew Ayenew		
Major Advisor	Signature	Date

We, the undersigned, members of the Board of Examiners of the thesis by **Keneni Alemayehu** have read and evaluated the thesis entitled "**Grey Wolf Optimization Algorithm Based Maximum Power Point Tracking, and Voltage Control of Stand-alone PV System with Storage Device: Application to Multi-Service Access Node**" and examined the candidate during open defense. This is, therefore, to certify that the thesis is accepted for partial fulfillment of the requirement of the degree of Master of Science in Electrical Power and Control Engineering

Chairperson	Signature	Date
Internal Examiner	Signature	Date
External Examiner	Signature	Date

Final approval and acceptance of the thesis is contingent upon submission of its final copy to the Office of Postgraduate Studies (OPGS) through the Department Graduate Council (DGC) and School Graduate Committee (SGC).

Department Head	Signature	Date
School Dean	Signature	Date
Office of Postgraduate, Dean	Signature	Date

ACKNOWLEDGEMENT

Firstly, I express my gratitude to the Almighty God for granting me the fortitude, chance, and enabling me to embark on and successfully accomplish this thesis. Additionally, I extend my appreciation to Adama Science and Technology University, specifically the School of Electrical Engineering and Computing, as well as the Power and Control Engineering department, for providing me with the opportunity to participate in this Master's program. I am filled with immense joy as I convey my profound appreciation to **Dr. Endalew Ayenew**, my advisor and mentor, for his sincere support and continuous guidance. His unwavering assistance, insightful advice, and constant inspiration have been of immeasurable value throughout the completion of this thesis, and I am extremely grateful for his contributions.

TABLE OF CONTENTS

CONTENTS **PAGE**

LIST OF TABLES

TABLE **PAGE**

LIST OF FIGURES

FIGURE **PAGE**

LIST OF ACRONYMS

ADF	Adaptive Fuzzy Logic
ASTU	Adama Science and Technology University
a-Si	Amorphous Silicon
BDC	Bidirectional Converter
BSS	Battery Storage System
CRF	Current Ripple Factor
CIS	Cupper Indium Silicon
C-Si	Crystalline Silicon
DC	Direct Current
FF	Fill Factor
FLC	Fuzzy Logic Control
GP	Global Peak
HC	Hill Climbing
HF	High Frequency
MPP	Maximum Power Point
MPPT	Maximum Power Point Tracking
M-C-Si	Mono Crystalline Silicon
MSAN	Multi-service access node
P&O	Perturb and observe

PTV	Personal Televisions
PID	Proportional Integral Derivative
PV	Photovoltaic
P-C-Si	Poly Crystalline Silicon
RES	Renewable Energy Sources
STC	Standard Test Condition
VOIP	Voice Over Internet Protocol
ZCS	Zero Current Switching
ZVS	Zero Voltage Switching

ABSTRACT

Current energy sources that show the most promise are renewable sources. Among the more encouraging forms of renewable energy sources is solar energy. The weather (temperature and radiation) has a significant impact on how well a PV module or array operates. Therefore, maximum power point tracking (MPPT) techniques are necessary to guarantee that the PV array generates the highest power feasible at all times and independent of the external conditions. The PV system's produced energy needs to be stored in order to be used during night time and cloudy days. To store PV generated energy, it is necessary to control the storage device with appropriate controller. In this thesis work a PV system of three modules of series connection is designed to supply a constant voltage for telecommunication multiservice access node. The storage battery and PV are both connected to a DC-bus via boost converter and bidirectional non-isolated converter respectively. The load terminal (multi-service access node) is connected to DC-bus via a buck converter. The maximum power of the designed PV system is tracked by grey wolf optimization based MPPT method. The Grey Wolf MPPT algorithm determines the point at which maximum power is present by using PV voltage and current as inputs. Then the algorithm generates duty cycle for operation of boost converter. The proposed MPPT technique was tested against 600W PV system under three various shading scenarios. The efficiency of the technique to track a maximum power under standard test condition is found to be 99.98%. Under shading condition of irradiation 1000W/m^2, 900W/m^2 and 700W/m^2 and constant temperature of 25°C, is found to be 99.83% and under shading condition of irradiation 1000W/m^2, 400W/m^2 and 600W/m^2 and temperature of 20°C, 18°C and 19°C is found to be 99.8%. The bidirectional converter determines the charge/discharge of the battery such that to keep DC-bus voltage at 72V. The converter is controlled by double loop optimal PI controller. If PV can generate a voltage more than 72V the converter will act in buck-mode to charge the battery by keeping DC-bus voltage at 72V. It will act in boost to discharge the battery mode if PV generate voltage less than 72V. The buck-converter takes DC-bus voltage as an input and produce a constant voltage of 48V for the load. The buck converter's voltage output is controlled by an optimal PID controller. Parameters of the controllers are optimized by PSO. The overall system supplies a constant voltage of fast response time and less oscillation for the load with buck converter's rise time and settling time being 0.78 and 1.98 second respectively.

Key words: - *Grey Wolf MPPT, Non-isolated bidirectional converter, PI, PID PSO, Boost-Converter, Buck-converter.*

CHAPTER ONE

1. INTRODUCTION

1.1 Background of the Sudy

Renewable energy sources have been gaining popularity and developing quickly throughout many countries. When compared to non-renewable energy sources, renewable energy sources (RES) are, clean, and environmentally friendly (Premkumar et al., 2020). Photovoltaic (PV) systems are one of well-known, promising, and cutting-edge RESs now in use for the generation of energy.

Solar generated energy is transformed into electrical energy by Solar photovoltaic (PV) systems. Sun energy is more extensively available globally than other renewable energy sources such as wind, geothermal, hydropower, and others. In photovoltaic (PV) systems, the maximum power point (MPP) is the point at which the product of the current (I) and voltage (V) of the solar panel is at its highest. This point represents the maximum power that the solar panel can deliver to the load under specific conditions of sunlight and temperature. If parts of the photovoltaic (PV) solar panel become shaded by external objects like clouds, buildings, or trees, the panel's output power may become suboptimal. This shading causes unequal irradiance across different PV cells in the panel. Some cells receive less sunlight than others.

When solar cells are shaded in this way, it disrupts the panel's ability to generate maximum output power from the available light. Cloud cover, nearby structures, or foliage that casts shadows can all introduce non-uniform irradiation across PV cells. This non-optimal irradiance distribution among cells within the panel results in reduced power harvesting compared to evenly illuminated cells without shading effects. When some PV cells in the array are shaded while others receive full sunlight, it prevents the array from maximizing power extraction from the available solar resource.

The uneven irradiance across cells due to shading results in suboptimal power output from the PV system. This reduced power generation has downstream effects on the overall energy system efficiency since less power is harvested than could otherwise be achieved under uniform illumination without shading interference. The power generation and system efficiency are both compromised because of the non-optimal power capture caused by shaded conditions within the PV array (Jirada et al., 2018). When some PV cells in an array get shaded while others receive full sunlight, the P-V curve generated by the system exhibits one true maximum power point (global peak) but also multiple lower local peak points. However, developing techniques to reliably track and maintain operation at the global peak power output under these non-uniform irradiance conditions remains a significant challenge that researchers are still working to address.

The presence of multiple peak values on a PV curve resulted from partial cell shading, creates difficulties for maximum power point tracking algorithms to discern and latch onto the highest overall power generation point rather than a suboptimal local peak (Pattathu et al., 2020, Jirada et al., 2018). It is unavoidable, particularly for PV systems located in cities and regions with a high frequency of slowly moving clouds (Pal & Mukherjee, 2020). If the control system is unable to adequately address and respond to the situation of partial shading within a PV panel, then the whole PV system shift from its intended optimal mode of regulated operation to an unregulated state.

Searching for an MPP is primarily concerned with controlling an output power obtained from a DC-DC converter. It sets up to normalize the operating voltage at its ideal value. This is achievable by adjusting the converter's duty cycle. To place the PV parameters in the PV module's optimal functioning range, the duty cycle must be adjusted. Consequently, it is thought that Maximum Power Point Tracking is a crucial phase in all PV systems. The converter’s duty cycle can be adjusted to do this. Adjusting the duty cycle is necessary to place the PV parameters into the PV module's optimal functioning range. As a result, all PV systems are thought to require Maximum Power Point Tracking (MPPT) regulation at some point.

To obtain better performance and increased efficiency of solar PV systems, a few modeling strategies have been offered in various literature, including one-diode configuration, two diode configuration, and three diode configurations (Malarvili et al., 2021). In addition, several MPP strategies have been put forth to maximize power and improve efficiency. In fact, accurate calculation of the current-voltage and power-voltage properties of a PV cells is critical to their efficiency and performance (Chen et al., 2016).

Many solar PV researches have made use of traditional optimization techniques including Incremental Conductance (INC), hill climbing, and other MPPT algorithms. Nevertheless, in the event of partial shade, these methods are ineffective (Chaieb & Sakly, 2015). Because there is only a single global peak and many local peaks, it is unable to track the maximum power.

Thus, rather of tracking the global peak, the above algorithms typically track the local peak. Knowledge-based controllers with superior calculation capabilities, such as fuzzy logic controllers, can more easily track the global peak and help alleviate the shortcomings of the traditional MPPT tracking method (Dehghani et al., 2021).

Finding the membership ranges and scaling factors takes time, even though the PV system with this controller produces higher outputs. The determination of the global peak (GP) during PSCs is the main goal of this study. This article presents the grey wolf optimization method, a soft computing approach that is garnering significant attention from the scientific community due to its increased robustness and speedier convergence when compared to conventional optimization strategies for MPPT.

GWO algorithm initializes with a random population of duty cycle ratios as the positions of the grey wolves. These duty cycles are applied to the PWM controller of the DC-DC boost converter connected to the PV array. The converter adjusts the PV voltage (Vpv) according to each duty cycle. The instantaneous current (Ipv) flowing from the PV array is measured. Using the measured Vpv and Ipv values, the actual power (P) output of the PV array is calculated. This power output is used to evaluate the "fitness" of each wolf/duty cycle.

In GWO, the fitness function aims to maximize PV power output. Based on the calculated powers, the top three duty cycles with highest power become the alpha, beta and delta positions respectively. Using GWO algorithms mathematical equations, the rest of duty cycles are updated based on the information of the top three positions. New duty cycles are then applied to the converter and the process iterates, with real-time Vpv, Ipv and power measurements at each step. This continues iteratively until the duty cycle corresponding to maximum measured PV power is obtained, indicating convergence at the MPP.

To supply a constant voltage to a load, control methods, such as the proportional-integral-derivative (PID) control (Park & Cho, 2014), fuzzy logic control (Jayaprakash & Ramakrishnan, 2015), feedback linearization control (Sulligoi et al., 2014), and sliding mode control (Ling et al., 2018, Louassaa et al., 2023 Hamza Sahraoui et al., 2015) are frequently investigated in relation to PV system voltage regulation technology.

In this thesis work PV system and storage battery were connected to a DC-bus through DC-DC boost converter and non-isolated bidirectional DC-DC converter respectively. The load terminal was connected to DC-bus through buck-converter. As discussed above the boost converter is used in maximum power point tracking, while bidirectional converter and buck-converter are controlled by optimal PI and PID controller respectively. Voltage at which the target load is to be supplied i.e., multiservice access nodes must be properly controlled. However, while attempting to meet the requirements, the controllers indicated above run into problems.

When a PID controller is used the tuning of its parameters is a big issue. Conventional SMC is prone to chattering effect, and fuzzy logic controller requires expert knowledge and finding the membership function is another problem. To overcome the above-mentioned problems this thesis designs the optimal PI controller whose optimal parameters are obtained by Particle Swarm Optimization Algorithm. To ensure the continuous supply of electricity to the load, battery storage system is applied. When solar radiation varies and temperature fluctuate, a storage device with a bidirectional converter can compensate the difference.

Numerous researchers proposed power systems from various renewable energy sources, various storing devices, and various load types (Senapati et al., 2019). In a standalone power system, nonlinear control is required when there are more converters and constant power loads that is predominant. For controlling inductor current and load bus voltage when there are fewer converters available, an individual linear PI controller seems to be a viable choice.

1.2 Statement of the Problem

Conventional MPPT techniques like Perturb and Observe (P&O) and Incremental Conductance (INC) have traditionally been used to track the maximum power from PV systems. While effective initially, they have limitations under rapidly changing environmental conditions. When solar irradiance and temperature vary significantly, or when modules are partially shaded, the PV output power characteristics exhibit multiple local maxima instead of a single clear global maximum. In such scenarios, P&O and INC struggle to lock onto the true MPP. Fuzzy logic control has also been applied for MPPT, but developing optimal membership functions and scaling factors can be complex and time-consuming.

Although output is higher, efficiency is still impacted under non-uniform conditions. To enable continuous power supply for loads, energy storage batteries are commonly integrated with charge/discharge controllers. Bidirectional DC-DC converters are often used to regulate battery charging from and discharging to the DC bus. However, previous charge/discharge controllers typically employ manual parameter tuning which affects battery performance and reliability over time. Controller parameters are manually adjusted in a trial-and-error manner, which may not find the optimum settings. To address these challenges (MPPT, and battery control), this research work proposes a new Grey Wolf Optimization (GWO) approach for MPPT an optimal dual loop PI controller for battery control.

By searching the power-voltage characteristics, GWO tracks the global MPP faster and with higher accuracy even under rapid irradiation and temperature changes or partial shading. Additionally, an optimal dual-loop PI controller is designed for the bidirectional converter to efficiently regulate the battery state-of-charge in a closed-loop manner. The PI parameters are automatically tuned using Particle Swarm Optimization for optimal controller performance. This ensures fast, stable and optimal regulation of battery charge/discharge without need for manual tuning iterations. Overall, the proposed control approach improves the system efficiencies and reliability.

1.3 Objectives of the Study

1.3.1 General Objective

To design a grey wolf optimization algorithm based MPPT and optimal voltage controller to stand alone PV system with storage battery.

1.3.2 Specific Objectives

- ✓ Apply grey wolf optimization algorithm to harvest peak power from PV system
- ✓ Under both constant and varying irradiation circumstances, extract the maximum output power.

- ✓ Design an optimal PI controller to non-isolated bidirectional converter and an optimal PID controller to buck-converter.
- ✓ Check for the proper operation of the bidirectional converter controller during charge and discharge condition along with different MPPT techniques.

1.4 Scope of the Study

The range of this work includes application of grey wolf optimization to MPPT algorithm to obtain maximum electrical power from PV system under various atmospheric circumstances. The GWO algorithm calculates maximum power which can be extracted from PV system and accordingly generates duty cycle for boost converter. The PV system is integrated to DC-bus via boost converter.

Storage batteries are used in conjunction with the optimal PI controller to provide a steady supply of electricity. The battery is linked to the DC-bus via a bidirectional DC-DC converter. The charge-discharge mode of the battery is achieved by non-isolated bidirectional DC-DC converter. PSO-optimized PI controller is designed to control the bidirectional DC-DC converter. Lastly, multi-service access node (MSAN) is integrated to the DC-bus via buck-DC-DC converter. The buck-converter's duty cycle is regulated by optimal PID controller to supply constant DC voltage to MSAN. The whole system is designed on MATLAB 2019/Simulink environment.

1.5 Motivation of the Study

As the telecommunications industry expands to remote areas, reliable power is needed to run MSANs that form the backbone of data networks. In many rural and off-grid locations, connection to the national power grid is either unavailable or unreliable. Diesel generators are commonly used but are costly to operate and maintain over the long run. They also produce greenhouse gas emissions and noise pollution. The thesis proposes designing a (PV) power system integrated to battery storage to generate a clean, sustainable and cost-effective alternative for powering MSANs even in the most remote areas without grid connectivity. Therefore, study in this area ensures the available electric power to improve sustainability of telecom service.

1.6 Significance of the Study

For the PV system, the robust MPPT algorithm that has been suggested outperforms the other traditional algorithm control system in terms of monitoring maximum global peak, and output power efficiency. In regions with varying weather, the implementation of this strong control system is extremely beneficial. The proposed battery charge/discharge control is beneficiary since it is simple for implementation and designed with optimal controller. It is highly efficient compared to isolated topologies like flyback converter. Fast dynamic response with PI control. Properly tuned PI controller can provide quick regulation of output voltage during charging/discharging transients. Simple design and lower cost. Non-isolated topology is simpler to design and implement than isolated topologies. Lower component counts also reduce costs. The proposed photovoltaic (PV) solar and battery energy storage system is significant as it provides a clean, independent and reliable backup power solution for MSANs. By harnessing solar energy and optimally managing an onboard battery bank, it can ensure continuous power supply to MSANs around the clock. Maximum power point tracking and an optimal controller further enhance the renewable energy system's performance and cost-effectiveness.

1.7 Organization of the Thesis

Chapter 2 presents overview of PV system, MPPT algorithms, PV system output voltage control, and storage battery. Chapter 3 discusses materials used for the thesis and system modeling as well. Chapter 4 presents controllers design for the system. In chapter 5 the result of simulation is presented and finally in the last chapter summary and recommendation is made.

CHAPTER TWO

2. BACKGROUND AND LITERATURE REVIEW

This chapter covers the background data on the PV system's electrical characteristics. Traditional Maximum Power Point Tracking (MPPT) methods, like incremental conductance (INC) and perturbation and observation (P&O) were also discussed. Furthermore, battery charge-discharge control and voltage regulation were covered.

2.1 Photovoltaic System

According to Taguchi et al. (2019), the history of PV began in 1839 when French physicist Alexandre-Edmond first introduced the PV phenomenon. But in 1883, Charles Fritts made the first photovoltaic cell, which had an efficiency of about 1%, by covering the selenium in a thin layer of gold from the junction. Bell Laboratories was the first to design the modern PV cell in 1954 (Taguchi et al., 2019). It was composed of semiconductor material based on silicon with an efficiency of about 4.5%. Due to spatial applications that need their own energy supply at all costs, the significance of PV sources expanded significantly during that time.

Later, in 1984, Arco unveiled the first silicon amorphous (a-Si) solar cell, and in 1986, the first thin-film photovoltaic module was created. The photovoltaic cell gained popularity as a power source for consumer electronics in the 1980s, finding use in radios, lanterns, watches, calculators, cameras, and other tiny battery charging applications (Taguchi et al., 2019).

The photovoltaic effect is a solar cell's most significant feature, which occurs when sunlight's photons strike a semiconducting material's surface and are absorbed, causing electron mobility. Current passes through the circuit as a result. Hence, PV cell functions as a current source. The two main factors that affect a PV cell's ability to generate current are temperature and irradiance. Figure 2.1 illustrates the basic workings of a conventional solar cell.

A p-n junction semiconductor diode is essentially what a solar cell is. Single-junction and multi-junction solar cells can be distinguished from one another based on their junction structure. In contrast to a multi-junction arrangement, which forms the junction using semiconductor materials with varying bandgap energies, a single-junction cell just utilizes one layer of lightabsorbing material. In the series, there are one or more junctions with progressively smaller band gaps after the top junction, which has a larger band gap than the others.

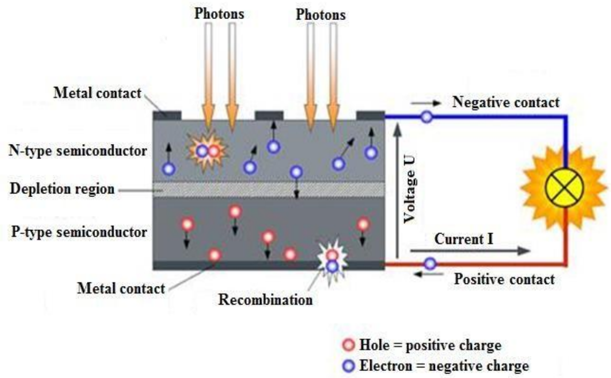

Figure 2.1: Operation of the solar cell (Curevac et al., 2014)

Large-energy photons will be absorbed at the top junction, and then small-energy photons at the junctions that come next. PV cells fall into one of two categories: thin-film cells or crystalline silicon (c-Si) cells, depending on the material used in their production. The following categories comprise the c-Si technology:

a) A silicon cell that is either monocrystalline or single crystalline (m-c-Si)
b) Multi- or polycrystalline silicon cells (p-c-Si)

Likewise, thin-film technology is categorized as follows:

a) silicon cell with amorphous structure (a-Si)
b) Gallium arsenide (GaAs) cell
c) Cadmium telluride (CdTe) cell
d) Di selenide (CIS) cell with copper indium (gallium)

Thin-film technologies, which fabricate solar cells using organic materials or carbon-based dyes and polymers (also called solar plastics), are frequently regarded as the nascent PV technology. Their primary benefit is that they are pliable and can bend without breaking, in contrast to Si, which is brittle. They are also incredibly affordable and light. They are currently highly inefficient, though. The only commercially produced Si cells these days are mc-Si, p-c-Si, and to a lesser extent, a-Si cells. C-Si technology is the foundation of 85–90% of global photovoltaic manufacturing (Shivendra Singh, 2020).

A single photovoltaic cell generates a very small voltage, about 0.5 to 0.6 volts. Therefore, to improve the voltage and current ratings, respectively, PV modules or panels are made up of PV cells linked in parallel or series.

To attain greater power output, numerous PV modules are connected in parallel and series configurations and deployed in an array field to form PV arrays (Tang et al., 2021). The cell, module, and array of PV structures are depicted in Figure 2.2. Every string of a module connected in series with blocking diodes in an array's parallel connection ensures that, if a string fails, the failed string won't absorb the power output of the remaining series strings.

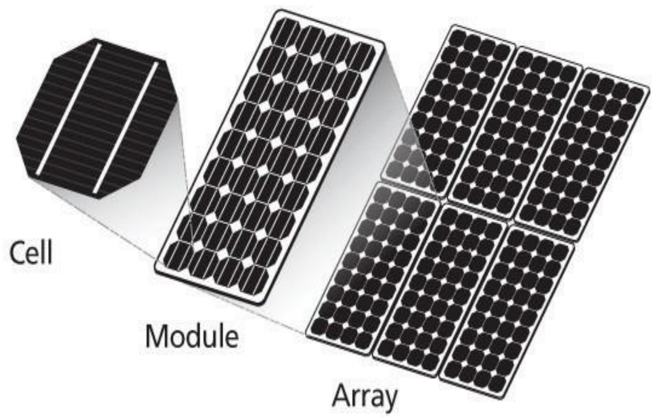

Figure 2.2: Cell, module, and array of PV (Betha Karthik Sri Vastav et al., 2017)

Furthermore, bypass diodes are linked to every module, so that, as seen in Figure 2.3, the modules' output that remain in string will skip the failing module if any one of the modules fails. These days, bypass diodes are included within PV modules (Vieira et al., 2020). Peak watts, or total power output, is the basis for rating the PV modules. The power generated at the PV module's output under standard test conditions (STC), which are defined as irradiance of 1000 W/m^2 and a module operating temperature of 25 °C, is measured in peak watts.

PV systems consist of more than just the PV module; MPPT controllers, inverters, batteries, and super-capacitors are among the other crucial parts of the system. The PV components' efficiency and dependability have increased over the course of many years of development. PV system performance and lifespan are impacted by several environmental elements, including humidity and temperature, presence of pollutants, corrosion, and so forth. The PV system's efficiency is mainly determined by three factors: convertor’s efficiency, the MPPT algorithm, and the PV module or panel.

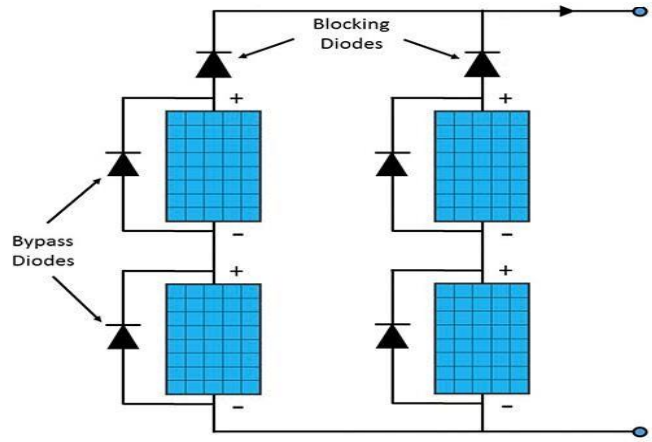

Figure 2.3: Series-parallel connection of modules (Chao-Ming Huang & Shin-Ju Chen, 2020)

Enhancing the efficiency of the module and convertor is a challenging task because it relies on current technology and may call for more expensive components overall. Alternatively, it is far simpler and less expensive to increase the MPPT algorithm's efficiency using various strategies. These MPPT control algorithms can also be applied to the current system to improve its performance. Because of the solar cell's voltage-current (I-V) nonlinearity as well as the characteristics of power-voltage (P-V), which change with temperature and irradiance, the MPPT algorithm must be implemented.

Typically, characteristic curves have a single point where the entire system produces its maximum power and runs as efficiently as possible. Temperature and radiation levels fluctuate throughout the day and across the seasons. In addition, irradiation fluctuates quickly because of shifting atmospheric elements like clouds. As a result, several MPPT methods have been developed and put into practice in order to retrieve the module's maximum power point (MPP), as documented in the literature. These algorithms vary in terms of cost, complexity, speed, accuracy, and range of operation (Tang et al., 2021).

2.2 Characteristics of PV Module

The PV module's electrical properties have been depicted by the characteristics of I-V and P-V curves. Because a p-n junction diode is a component of the photovoltaic energy conversion process, PV cells and modules typically have non-linear properties (Belhachat & Larbes, 2017). The two primary variables that impact properties the PV module are temperature and irradiance.

The open-circuit voltage (Voc) and short-circuit current (Isc) are two further features that are essential to the PV module's performance.

The term "short circuit current" (Isc) refers to the maximum current generated by the module when its terminals are shorted together. There will be no voltage across that module under this state. At these places, there is no output power because there is no voltage or current under the open circuit voltage and short circuit current, respectively (Zhao et al., 2020). At the maximum voltage-current product, the module produced the most power. The distinctive curves demonstrate how unique this point is, which is referred to as an MPP.

The fill factor (FF) can be determined by Voc, Isc, MPP voltage (V_{MPP}), and I_{MPP}. The maximum power (PMPP) to the product of the short circuit current and the open-circuit voltage is the definition of the FF. This is the most important component to consider when assessing the solar cell's performance.

$$FF = \frac{V_{MPP} \times I_{MPP}}{V_{OC} \times I_{SC}} \tag{2.1}$$

A high FF indicates a high-grade cell with little internal power losses. The PV cell performs better the closer the FF gets to unity. Between (0.6 and 0.8) is a nice FF.

The conversion efficiency of a solar cell or solar module is defined as the ratio of output power to input power. The power generated by solar radiation is considered the input power, while the power acquired at the MPP is considered the output power.

$$\eta = \frac{P_{MPP}}{P_{in}} = \frac{V_{MPP} \times I_{MPP}}{P_{in}} = \frac{V_{OC} \times I_{SC} \times FF}{P_{in}} \tag{2.2}$$

2.3 Factors Affecting Photovoltaic Modules

Making informed decisions about how to minimize those challenges and estimate how to regulate them will be made easier with an understanding of the factors that influence PV features. Multiple factors impact the efficiency of PV systems. Among the elements that affect solar systems are these three: temperature, irradiance, and shade.

2.3.1 Effect of Temperature

PV modules' performance is significantly impacted by its temperature. It is shown that temperature has the biggest impact on terminal voltage. As the temperature drops, the PV Voltage rises. This is unexpected because one would think that as the temperature rises, the PV array will become more efficient. The energy gap of semiconductor materials varies with temperature, which is the reasons the PV array performs better at lower temperatures. The material's band gap energy rises as temperature increase. Valence shell electrons will need more photon energy to go into the conduction band as the band gap energy rises.

2.3.2 Effect of Irradiation

The maximum amount of electricity that photovoltaic arrays may produce limits their efficiency. Because PV arrays depend on variables that are not consistent, the quantity of electricity taken out from a PV module can be highly variable. One significant factor influencing a solar array's performance is irradiance. This term is used to describe the quantity of radiation that strikes a particular surface. In a photovoltaic system, it is the amount of solar energy that the array absorbs over its surface area.

2.3.3 Shading Effect

The string performs worse (partially shadowed) if none of the solar cells in a series-connected string are lighted evenly because of neighboring structures' shade, birds on the array, falling tree leaves, and other elements. A portion of a PV array's cells are probably shaded if it is spread out across a wide area. A series-connected string of cells has a single current flowing through each cell. Despite producing less photon current, the shaded cells must nonetheless transport the same amount of current as the well-lit cells.

Reverse biased cells have the potential to act as loads, sapping the energy from fully lit cells. If the system is not adequately protected, a hotspot issue may occur, and in certain situations, the system possibly sustains irreversible harm. This issue is resolved by a bypass diode, which creates a practical current channel around any cells that are darkened. One bypass diode should be included in every solar cell, but they are too costly.

2.4 Conventional MPPT Algorithms

2.4.1 Perturb and Observe Algorithm

The P&O approach is widely utilized MPPT method in commercial PV devices because it is simple to implement. In some literary study, the P&O is also known as Hill Climbing (HC). According to some literature, the P&O and HC MPPT algorithms differ from one another in the fact that the voltage is perturbed in the former case, while the duty cycle of the PWM signal is perturbed in the latter. Because both terms refer to the same technique—varying the PV module's output voltage by feeding a disturbance in the duty cycle to the converter—they are synonymous. The duty cycle (D) of the algorithm is slightly perturbed, and the module power is then observed as a result. If the power rises in response to a change in D, the perturbation ought to stay there. On the other hand, if the shift in D results in a drop in power, the disturbance in the following cycle will be in the other direction.

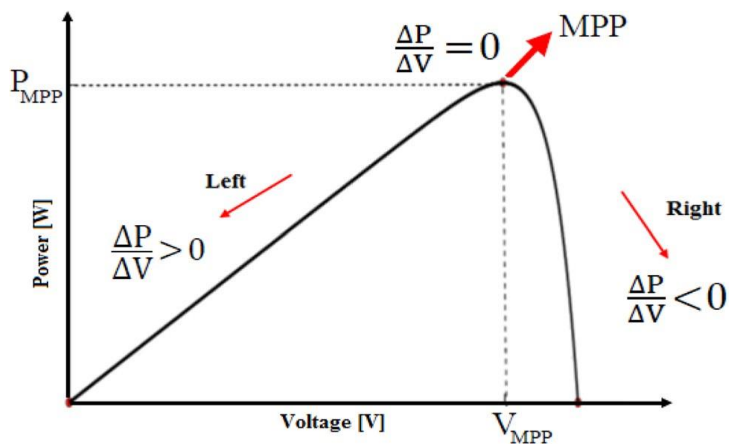

Figure 2.4: PV Module characteristics curve (Mohamed & Abd El Sattar, 2019)

As seen in Figure 2.4, the MPP is reached when the dP/dV equals zero. More disturbance to the right is necessary to achieve MPP if dP/dV>0, which indicates that the current operating point is to the left of MPP. If dP/dV is not equal to zero, MPP is to the right of the operating point, and further disturbance to the left is required to achieve MPP.

The approach converges to MPP in this manner across many perturbations. The P&O MPPT algorithm is limited in two significant ways. First, even when the system reaches a steady state, it continues oscillation about the MPP, which could result in an output power loss.

Second, tracking the incorrect MPP may occur due to this method's inability to function effectively during abrupt changes in the insolation level. It is necessary to maintain very tiny perturbation sizes to minimize oscillation around MPP; however, doing so slows down the rate of convergence, meaning it will take the system longer to reach MPP. To accelerate convergence, a high perturbation value is selected, which increases the system's power losses. The P&O flow chart is illustrated in Figure 2.5

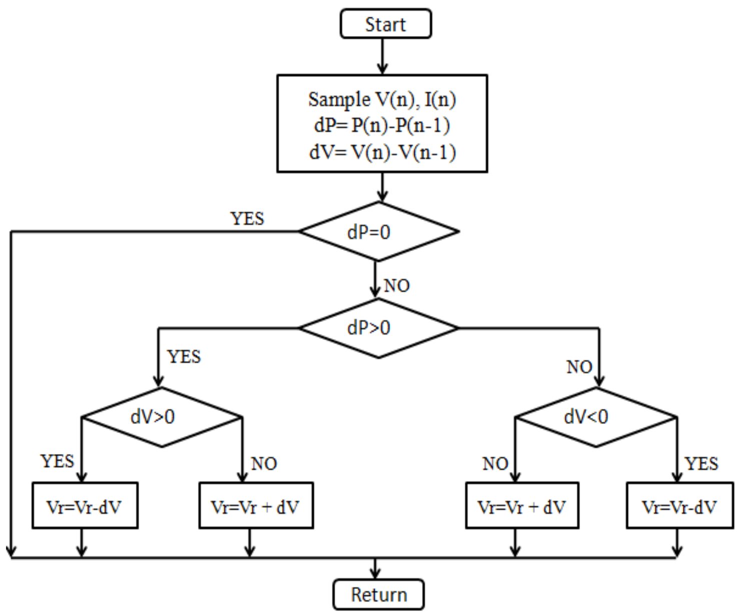

Figure 2.5: Flow diagram for traditional P&O (Chinna Kullay Reddy et al., 2018)

When dP>0 and dV>0 thus $\frac{dP}{dV} > 0$ boost the duty cycle, D=D+ΔD

When dP<O and dV<0 thus $\frac{dP}{dV} < 0$, reduce the duty cycle, D=D-ΔD

When ΔP_{PV}=0 and ΔV_{PV}=0, keep the duty cycle D, ΔD=0 and D=D

2.4.2 Incremental Conductance MPPT Algorithm

In light of the finding that the MPP has been attained when the PV curve's slope equals zero, as depicted in Figure 2.6, the INC algorithm operates. By computing the conductance and incremental conductance instantaneously and comparing them, this technique tracks the maximum power operating point of the module. The following formulas are used to illustrate this approach.

$$\left.\begin{array}{ll} \dfrac{dP}{dV}=0 & at\,MPP \\ \dfrac{dP}{dV}>0 & left\,of\;MPP \\ \dfrac{dP}{dV}<0 & right\,of\;MPP \end{array}\right\} \tag{2.3}$$

$$\frac{dP}{dV}=\frac{d(I\times V)}{dV}=I+V\,\frac{dI}{dV} \tag{2.4}$$

From Equation (2.3) and (2.4), we get

$$\left.\begin{array}{ll} \dfrac{dI}{dV}+\dfrac{I}{V}=0 & at\,MPP \\ \dfrac{dI}{dV}+\dfrac{I}{V}>0 & at\,left\,of\;MPP \\ \dfrac{dI}{dV}+\dfrac{I}{V}<0 & at\,right\,of\;MPP \end{array}\right\} \tag{2.5}$$

This method senses the voltage and current at the same time. As a result, changes in voltage or current indicate changes in temperature and sunlight (insolation). Therefore, under a range of environmental conditions, this approach can follow the MPP. This technique addresses the limitation of the P&O MPPT algorithm under various environmental circumstances. Figure 2.6 displays the INC flow chart.

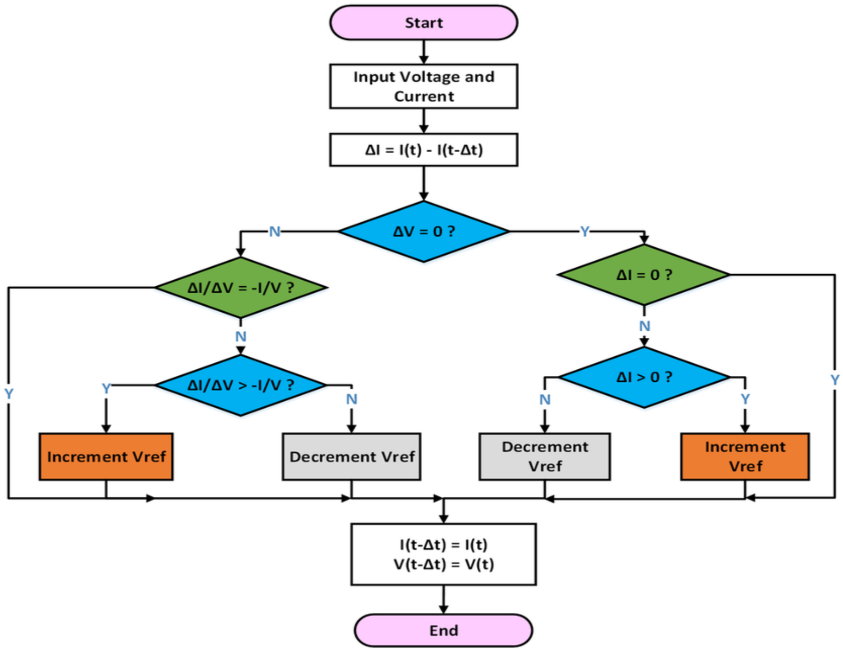

Figure 2.6: Flow chart of INC MPPT (Masood et al., 2021)

2.5 Battery Storage System

Electrical energy from solar radiation is produced using photovoltaic cells. Only during the day is solar energy available, and its strength is influenced by the surrounding conditions, such as cloud, and etc. When there is an abundance of solar energy, it is stored using a storage element to get over this problem. When load demand can't be met by solar power alone, stored energy will be used. The most widely utilized storage element is the battery, because it stores energy through an electrochemical process and responds quickly to both charging and discharging conditions. In addition, batteries are more power- and energy-efficient than other types of technologies for storing energy, including compressed air systems and ultra-capacitors. The power reliability of the PV power generating system is enhanced by the flexible energy management that the BSS may offer (Li et al., 2013).

2.6 Related Works

2.6.1 MPPT Techniques

Many studies employing various techniques and optimizations, respectively, are published on the MPPT under partial shading situations and parameter estimations.

This section reviews relevant studies according to performance measuring criteria such as tracking time efficiency, power output under fluctuating irradiance, and temperature. According to the literature (Parvaneh & Khorasani, 2020), a hybrid fuzzy logic and P&O MPPT controller was studied. Taking varied irradiations into consideration, the efficiency of the suggested approach was examined.

A fuzzy logic-based controller has been designed by the authors to help the traditional P&O method and finds the global peak power. Consequently, the efficiency and output power were improved over the P&O method. However, it exhibits steady-state output power variation and a tracking time that is not as robust as anticipated. By utilizing soft computing approaches on the fuzzy logic side and looking for the best parameter values, the outcome can be further enhanced.

The literature suggests a novel adaptive fuzzy logic controller (ALFC) to regulate a solar PV system using MPPT when partial shade is present (Laxman et al., 2021). The best range of fuzzy membership functions was found by applying grey wolf optimization (GWO). In contrast to conventional P&O algorithms and FLC, the suggested controller produces higher output power and efficiency. The limitations of this study include finding the optimal range of scaling factors. Furthermore, the controller was validated in low-power applications; therefore, the optimization and adaptation might not be feasible for applications requiring medium- to high-power.

One other limitation of this work is the verification of the optimization outcomes, including error and transient parameter analysis. By reducing the limitations and downsides, the findings of this study can be enhanced even more. There has been literature implementation of FL-based MPPT controller performance analysis (Khan et al., 2022). Under constant temperature and various irradiation settings, the analysis was carried out.

In that study, there was minimal optimization of scaling factors. Comparing the suggested FL algorithm to classical algorithms, the output power effectively tracks the global peak. No shading condition has been provided. Consequently, it is impossible to confirm whether the result is robust. Comparably, a PV system's output power analysis has been discussed in literature employing a FL MPPT controller (Malarvili et al., 2021). The fuzzy logic controller assisted in identifying the optimal global peaks of the output power through the usage of a particle swarm optimization (PSO) algorithm.

Nonetheless, the power output result exhibits some oscillations in the transient period and greater tracking time, as can be observed from the literature. This work is moving more slowly than the previously stated literature (Laxman et al., 2021). Additionally, the controller only checked the irradiation condition in one scenario; low power circumstances were not checked for controller performance.

The work only includes analysis of the transient behavior and scaling factor optimization. The researchers in the literature (Elkholy & Abou El-Ela, 2019) looked at a List Square Fitting (LSF)-based parameter estimation algorithm. From relevant literature, the PV modules' measured voltage and current are obtained. When contrasted with other publications, the outcome was superior (Yuan et al., 2014). Nevertheless, output power analysis is the study's shortcoming, though, as it is restricted to parameter estimate only. Using evolutionary algorithms can also enhance the calculated parameters even more.

In (Nazeri et al., 2022) maximum power point tracking based on P&O was studied. Due to cell/module mismatch, the PV array P-V curve becomes non-smooth in partial shadowing and has several local maxima. The smooth curve is assumed by the usual P&O algorithm. The P&O algorithm could bounce between nearby local maxima as a result of the disturbances rather than converging on the global peak. In the event that the perturbation shifts the operating point from the global peak to a local peak in the vicinity, the P&O will become stuck there upon detecting an increase in power.

In (Gomathi B & Sivakami P, 2021) incremental conductance MPPT was designed to obtain the maximum output power of PV system. However, under changing irradiance incremental conductance can still oscillate between nearby local maxima failing to lock firmly on the global MPP.

2.6.2 Battery and Load voltage Control

The PV power generating system's power quality is improved by the flexible energy management solutions that the battery storage system may offer. Regardless of changes in source or load power, the lead-acid battery's main purpose is to provide steady power to the load. Utilizing a lead-acid battery with two modes of operation, this stand-alone PV system: when solar power is insufficient, it must be discharged to supply local load or charged to reserve extra energy from PV source when there is extra energy from PV system. The primary objective of the battery converter is to establish and maintain a steady common DC bus voltage. To sustain the DC bus and BSS powered continuously while maintaining a constant load voltage, a bidirectional buck-boost DC-DC converter is employed.

The lead-acid battery automatically charges or discharges to keep the DC-bus voltage steady. No matter if the battery is charging or discharging, the voltage powering the load stays constant and stable. This system uses a 72V DC voltage as its reference. When considering battery voltage, the DC bus voltage is much higher. Lower voltage batteries offer significant advantages.

The main component of the system that is utilized to charge/discharge battery is bidirectional DC-DC converter. There are a wide range of designs of bidirectional converters (Sathishkumar et al., 2020). Regular bi-directional converters struggle to deliver high voltage gain and good efficiency at the same time. This is because of power losses in the switches and leakage in the coils. The bi-directional converter's galvanic isolation results in extra losses because of magnetic losses.

The (Shreelakshmi M. P & Moumita Das and Vivek Agarwal, 2014) bi-directional converter employs a simple design consisting of two switching elements. Its circuit complexity and slow response are its drawbacks. However, it has a high gain and great efficiency. (Santra et al., 2021) suggest a converter with a high frequency transformer for bi-directional power conversion. The high-frequency (HF) transformer adjusts the AC voltage level during operation. It steps down the voltage for charging and allows the DC voltage from the battery to pass through to the output at a higher voltage during discharge. Then, it moves on to a secondary full bridge converter, which functions as a buck/boost converter after acting as an inverter during discharging and a diode rectifier during charging. Although this circuit appears simple, it is difficult and expensive to design.

The bi-directional converter proposed by (L.H.P.N. Gunawardena & D.R. Nayanasiri, 2019) employs a relatively simple design consisting of three switching elements. This converter manages the magnetic coupling's leakage inductance, which stores energy and is essential to the realization of a power converter. The BDC suggested in (Satyam Kumar Singh et al., 2019) consists of one inductor, two capacitors, and four switches.

Mode-selecting switches S1 and S2 operate in buck/boost mode, whereas power flow control switches S3 and S4 are employed in this mode. One of the drawbacks of this converter design is its ON state switching loss. The LCL Resonant BDC proposed in (Pavan Singh Tomar, Ashok Kumar Sharma, et al., 2018) employs non-isolated converters and soft switching. There are three inductors, four switches, and four capacitors in this converter. ZCS is used by this converter to turn on and off diodes, while ZVS is used to turn on switches. Switches and diodes are stressed by the BDC duty ratio, which leads to reverse recovery loss and very low conversion efficiency in such an operation.

In (Ramos-Paja et al., 2020) a cuck-converter was designed to control battery charge/discharge to keep DC-bus voltage constant. It designed non-linear SMC to control the converter. However, the controller design lacks optimal parameters and resulted in slow response of the system. In (Andres Ramos-Paja et al., 2021) a flyback-converter was designed to charge/discharge a battery; however, the performance of the system was not so good because of, lower efficiency than non-isolated topologies due to transformer losses. Battery charge/discharge was done through a SEPIC converter with PID controller in (Putri et al., 2022). It was designed with automatic disconnection of the battery when the battery was fully charged. However, the settling time of the system was too slow due to manual tuning of the PID parameters.

Non-isolated converters are compatible, have excellent efficiency, and have less magnetic bulk (Burcu Gundogdu and Daniel Thomas Gladwin, 2018). Since it must run at a high frequency to meet the requirements for a high-power density, soft switching is employed to reduce switching losses. (Pavan Singh Tomar, Manaswi Srivastava, et al., 2018) describes a BDC with switching cells that has two inductors, three switches, and four capacitors to produce a high conversion ratio. Nevertheless, the converter is large and costly due to the extremely high-value capacitors and inductors. As mentioned in (Aiguo Sun et al., 2014), BDCs with inductor couplings offer strong voltage conversion ratios even at very high duty ratios.

One disadvantage of this converter is that if the inductor is not properly connected, it can cause large conduction losses, stress on active switches, and electromagnetic interference (EMI) when it operates at an extreme duty ratio. Various controllers were applied to a DC-DC buck converter in literatures. In (W.J. Gil-Gonzalez, 2019) passivity-based PI controller was designed to control the output voltage of a DC-DC buck converter. The controller was robust to disturbances compared to the conventional controllers. However, the controller may not be universally applicable due to parasitic elements and non-idealities in real-world components affecting the ideal passive model.

This work presents a non-isolated bi-directional DC-DC converter with two active switches, two capacitors, and one inductor to control the battery's charge/discharge mode. The converter is controlled by an Optimal PI controller. It provides higher efficiency compared to an isolated converter due to the absence of a transformer. This results in less power losses and better utilization of the available solar and battery power. Less power lost in the converter leaves more available at the DC bus for the MPPT controller to maximize harvesting from the PV module. While the MPPT performance itself is not directly improved, it has more usable power to work with. An optimal PI controller has optimized proportional-integral gains that allow it to precisely control the duty cycle of the bidirectional converter for fast battery charging/discharging. Precise duty cycle control ensures the DC bus voltage is well-regulated, maintaining maximum solar energy harvesting by the MPPT controller. Faster tracking of optimal duty cycle by an optimal PI controller result in less power fluctuation on the DC bus. This stabilizes the MPPT algorithm and allows it to operate at peak efficiency, maximizing solar energy utilization.

CHAPTER THREE

3. MATERIALS AND METHODS

3.1 Overview

This chapter discusses mathematical modelling and controller design for PV system for application of DC load, specifically multi-service access node. It includes mathematical modeling of PV system, grey wolf optimization based MPPT, mathematical modeling of boost converter for MPPT application, non-isolated bidirectional DC-DC converter's mathematical modeling along with optimal PI controller design for battery charge-discharge purpose and finally discuss mathematical modeling of an optimal buck converter design for output voltage control.

3.2 Materials Used

For the research work, MATLAB/2019, Microsoft Office 2019, and Math Type 7.0 equation writer and Mendeley Reference Manager were utilized. Technical toolboxes and Simulink are included with MATLAB software.

3.3 Methods

The methodology that has been used, as depicted in Figure 3.1, is utilized to achieve objectives of this study. Initially, the related works are read and problem is identified. Secondly, the system components' mathematical model is done. Thirdly, the proposed controllers are designed as per the mathematical model of respective component. In the fourth step simulation and result analysis is held. Lastly, conclusion and documentation are carried out.

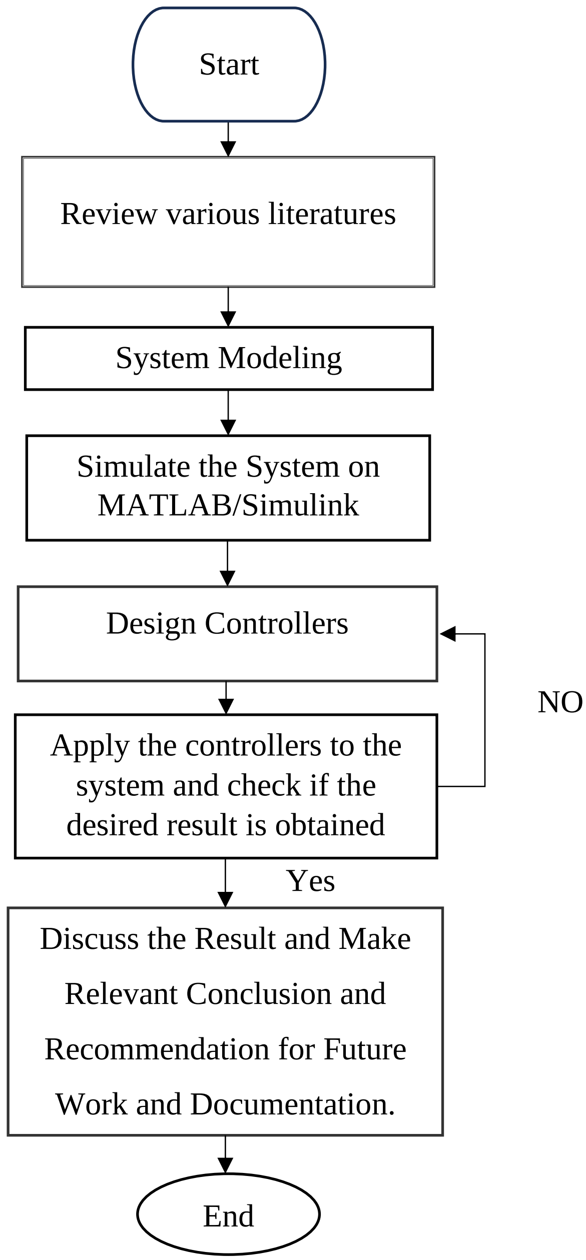

Figure 3.1: Work flow of the thesis

3.4 Block Diagram of the Research

The block diagram of the proposed research work is as illustrated in Figure 3.2

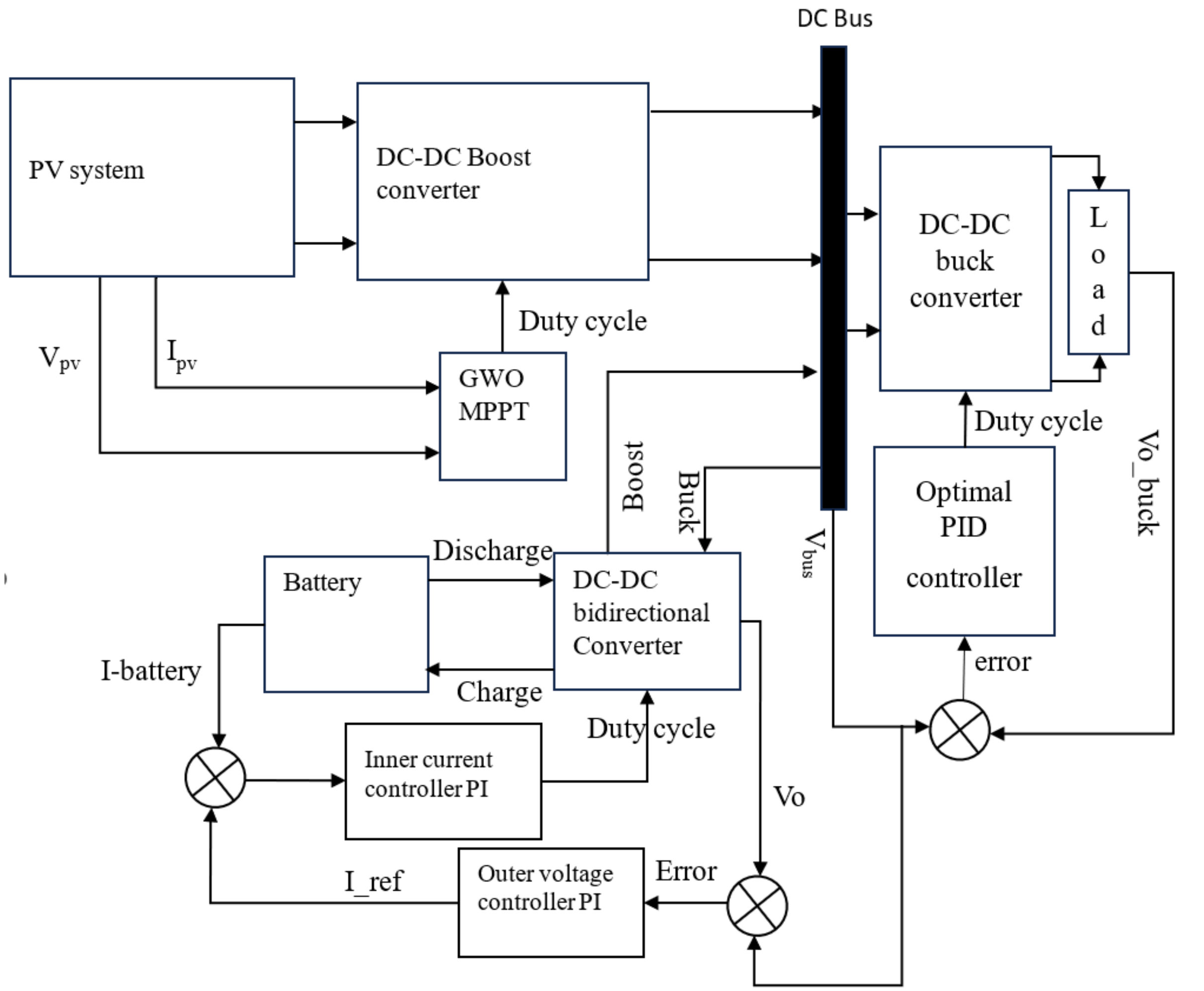

Figure 3.2: Block schematic of the thesis

The block diagram shows a 1kW photovoltaic (PV) solar system comprising various power electronic converters connected to a DC bus and storage battery. A new maximum power point tracking (MPPT) technique based on Grey Wolf Optimization (GWO) is used to extract maximum power from the PV panels. This GWO technique takes the PV current and voltage as inputs. It then searches for the point of maximum power output by calculating the PV array's power for different operating conditions.

Based on the calculated power, the algorithm generates a duty cycle for the boost converter connected to the PV panels. This boost converter adjusts the PV voltage to ensure the panels operate at their maximum power point. The converter feeds the extracted solar power to the DC bus. A storage battery is also integrated using a bidirectional DC-DC converter connected between the battery and DC bus. This helps provide continuous power supply to the load. The converter's state of charge control uses a double-loop PI controller.

The outer voltage control loop regulates the DC bus voltage at 72V. It generates a reference current signal for the inner current loop. During charging, a negative current setpoint directs excess solar power to the battery if the bus voltage exceeds 72V. During discharging, a positive current setpoint draws power from the battery to maintain the bus voltage if it drops below 72V. Accounting for errors, the inner current loop then produces duty cycle signals to properly charge or discharge the battery via the bidirectional converter. A telecom multi-service access node (MSAN), which aggregates various subscriber connections, represents the load. It requires a -48V DC power supply. So, a buck converter steps down the higher DC bus voltage to the required 48V for the MSAN. Particle swarm optimization algorithm is used to optimize the parameters of the double-loop PI controller regulating the battery charging/discharging process and a PID controller controlling buck-converter.

3.5 Mathematical Model of PV System

Simulating a PV system effectively involves knowing characteristic curves of I-V and P-V across various environmental factors like temperature and irradiance levels. For representing a solar cell electrically (Chao-Ming Huang & Shin-Ju Chen, 2020) as depicted in Figure 3.3, the parallel connection of an exponential diode and a constant current source can be thought of as a solar cell circuit.

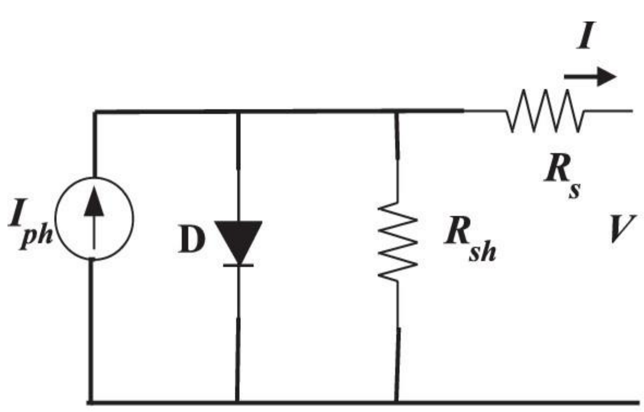

Figure 3.3: Single-diode model of PV cell (Chao-Ming Huang & Shin-Ju Chen, 2020)

The single-diode model's electrical circuit, when analyzed using Kirchhoff's Current Law (KCL), allows us to derive an equation for the photovoltaic cell's output current, as shown by:

$$I = I_{ph} - I_D - I_{sh} \tag{3.1}$$

where I, represents the output current of PV cell, I_{sh} represents current passing through the resistor R_{sh}, I_{ph} represents photo current, and I_D represent the current flowing in the diode. Equation (3.1) is capable of calculating the Shockley equation, which is the term that represents the current flowing through the diode.

$$I_D = I_O \left\{ \exp\left[\frac{q\left(V + I \times R_s\right)}{A \times k \times T} \right] - 1 \right\} \tag{3.2}$$

$$I = I_{ph} - I_o \left\{ \exp\left[\frac{q\left(V + I \times R_s\right)}{A \times k \times T} \right] - 1 \right\} - \frac{\left(V + I \times R_s\right)}{R_{sh}} \tag{3.3}$$

Where T represents the cell's operating temperature, A represents the idealization constant of the diode D, k represents the Boltzmann constant (k = 1.38 10 J / K ×10 -23), Io is the saturation current, and q is the electron charge (q = 1.60 x10-19 C). The amount of sunlight (irradiation) and the operating temperature significantly influence the photogenerated current. Equation (3.4) provides a definition for it.

$$I_{ph} = \left[I_{scn} + K_i \left(T - T_n \right) \right] \frac{G}{G_n} \tag{3.4}$$

Here, T stands for the ambient temperature, Tn stands for the nominal temperature, *G* signifies the real-time solar irradiance, and *ki* represents short circuit current's coefficient.

Isc denotes the solar cells short-circuit current, measured under specific controlled conditions: a cell temperature of 25°C (Tn) and a sunlight intensity of 1,000 watts per square meter (Gn). These conditions are known as Standard Test Conditions (STC). A mathematical definition of the solar cell's saturation current can be found in Equation (3.5).

$$I_o = I_{rr} \left(\frac{T}{T_n} \right)^3 \exp\left[\frac{q \times Eg}{k \times A} \left(\frac{1}{T_n} - \frac{1}{T} \right) \right] \tag{3.5}$$

where Eg denotes the band gap energy (Eg = 1.10 eV) of the silicon photovoltaic cell and *Irr* signifies the reverse saturation current of the solar cell at a specific temperature (Tn) and under a certain level of solar irradiance (Gn). The remaining parameters have the same definitions. In this context, *Ns* signifies the number of photovoltaic (PV) cells linked together in series, while Np denotes the number of these cells connected in parallel. The output current of a photovoltaic module is given by Equation (3.6).

$$I = N_p I_{ph} - N_p I_o \left\{ \exp\left[\frac{q\left(N_s \times V + \left(N_s / N_p\right) I \times R_s\right)}{N_s \times A \times k \times T} \right] - 1 \right\} - \frac{N_s \times V + \left(N_s / N_p\right) I \times R_s}{\left(N_s / N_p\right) R_{sh}} \qquad (3.6)$$

3.6 Boost Converter Model

The boost converter, widely recognized as the most popular DC-DC converter, increases the voltage delivered to the load (Vo) compared to the source voltage (Vs). As seen in Figure 3.4, a boost converter consists of an output capacitor connected in parallel to the load, diode and a transistor, and a boost inductor (Mirza Fuad Adnan, Mohammad Abdul Moin Oninda, Mirza Muntasir Nishat, et al., 2017).

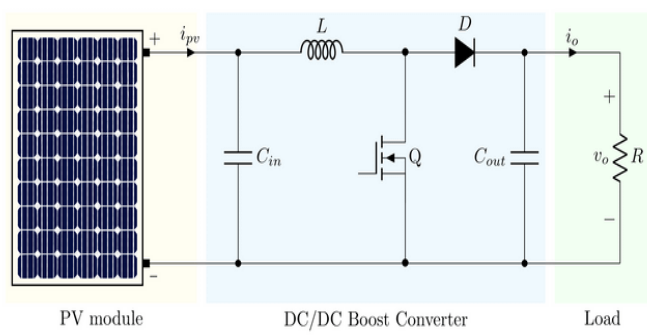

Figure 3.4: Boost converter circuit diagram (Kumar et al., 2017)

Because MOSFET has higher switching frequency as compared to IGBT, it is favored in low voltage situations. The boost converter can operate in the following modes: At t = 0s, mode 1 starts. When the transistor activates, it allows more current to flow from the input. This current increases gradually and charges the inductor (L) by building up a magnetic field that stores energy. At t = t1, when the transistor gets turned off, mode 2 starts. A quick reduction of current in the inductor L causes it to create a back emf that is opposite in polarity to that of Mode 1. The voltage powering the load and charging the capacitor (C) comes from the combined voltage of the inductor (L) and the source (Vs), minus a small voltage drop caused by the diode (D) when it conducts. Figure 3.5 illustrates the switching period of the converter.

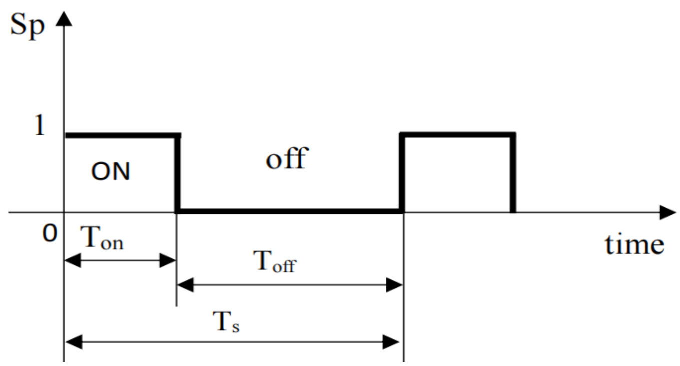

Figure 3.5: Switching period of boost converter

The related boost converter circuit models during the two states of the switch—ON and OFF, respectively—are shown in Figures 3.6 and 3.7.

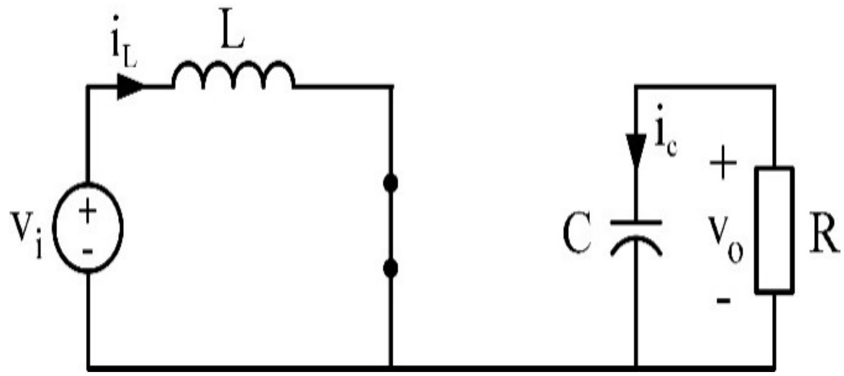

Figure 3.6: Circuit diagram of the boost converter in ON period of the switch (Evren Isen, 2021)

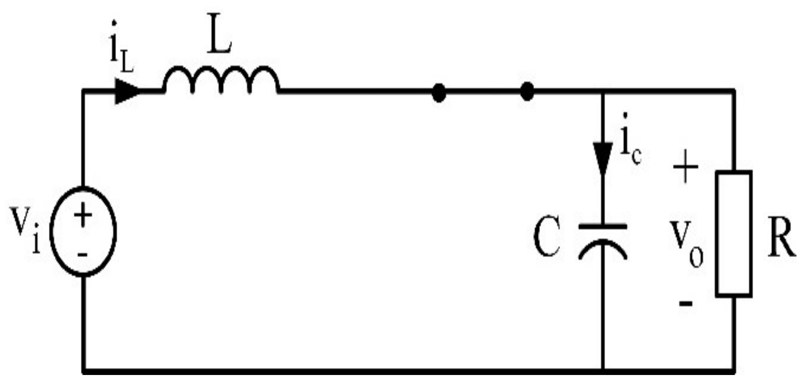

Figure 3.7: Circuit diagram of the boost converter in OFF period of the switch (Evren Isen, 2021)

Time of a transistor can be provided by:

$$Mode1 \quad T_{on} = D \times T_s \tag{3.7}$$

$$Mode2 \quad T_{off} = \left(1 - D\right) T_s \tag{3.8}$$

The voltage induced in the inductor (L):

$$Mode1 \quad L\frac{di_L}{dt} = V_i \tag{3.9}$$

$$Mode2 \quad L\frac{di_L}{dt} = -\left(V_i - V_o\right) \tag{3.10}$$

Putting Equation (3.7) and (3.8) into Equation (3.9) and (3.10) :

$$Mode1 \quad L\frac{\Delta i}{D \times T_s} = V_i \tag{3.11}$$

$$Mode2 \quad L\frac{\Delta i}{\left(1 - D\right) T_s} = V_o - V_i \tag{3.12}$$

Ripple current Δi, is given by:

$$Mode1 \quad \Delta i_{on} = \frac{V_i \times D \times T_s}{L} \tag{3.13}$$

$$Mode2 \quad \Delta i_{off} = \frac{\left(1 - D\right)\left(V_i - V_s\right) T_s}{L} \tag{3.14}$$

By equating the ripple current equations and of mode1 and mode 2

$$\Delta i_{on} = \Delta i_{off} \tag{3.15}$$

$$V_i \times D = V_o - V_i - D \times V_o + D \times V_i \tag{3.16}$$

$$V_i = V_o - D \times V_o \tag{3.17}$$

$$V_i = \left(1 - D\right) V_o \tag{3.18}$$

$$\frac{V_o}{V_i} = \frac{1}{1 - D} \tag{3.19}$$

Where:

V_i Input voltage from PV, V

V_o Output voltage, V

t_{on} MOSFET ON, sec

t_{off} MOSFET OFF, sec

T_s Switching period, sec

D Duty cycle

Δi Ripple current

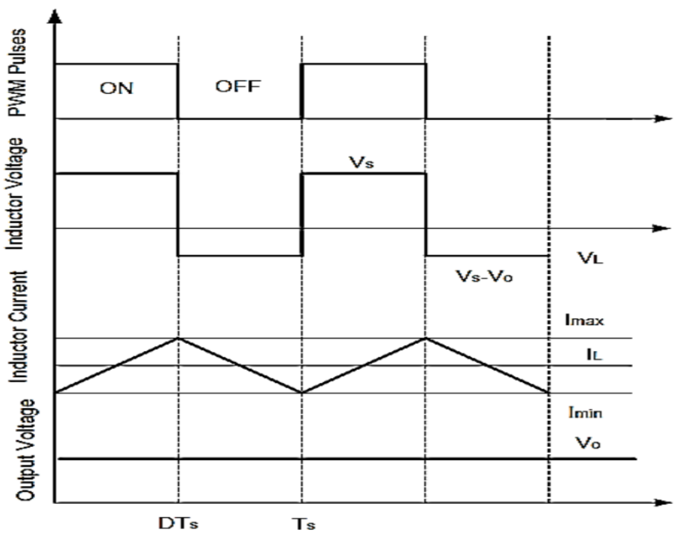

Figure 3.8: Boost Converter's Output wave form (Mirza Fuad Adnan, Mohammad Abdul Moin Oninda, & Nafiul Islam, 2017).

3.6.1 Discontinuous and Continuous Conduction Mode

DC-DC converters utilize two distinct operating principles. During continuous conduction mode (CCM), the current flowing through the inductor always remains above zero throughout a single switching cycle. In discontinuous current mode (DCM), the current in the inductor falls to zero before the completion of a single switching cycle. Equation (3.20) can be used to get the inductance value that will allow the boost converter to function in continuous mode, provided that inductance L > Lmin.

$$L_{\min} = \frac{\left(1-D^2\right)D\times R}{2f_s} \tag{3.20}$$

This equation considers several key parameters: fs (switching frequency of the switch), D (duty cycle), R (output resistance), and Lmin (minimum inductance). The output capacitance value that provides the desired output voltage ripple is as follows:

$$C_{\min} = \frac{D}{2 \times R \times f_s} \tag{3.21}$$

In this case, C_{min} stands for the minimal output capacitance, R for the load resistance, and fs for the switching frequency.

3.6.2 Design of boost converter

By manipulating the duty cycle within the Pulse Width Modulation (PWM) signal, driving the converter switch maximizes power transfer. The MPPT system's duty cycle would range from30% to 70%. To find the expected maximum voltage output, apply the formula below:

$$V_o = \frac{V_{in} - V_T \times D}{1 - D} - V_d \tag{3.22}$$

Where:

D denote duty cycle, V_d represent diode saturation voltage, V_T terminal voltage of PV

Current Ripple Factor: The International Electrotechnical Commission (IEC) harmonics standard states that the CRF should have a boundary of 20% to 40%.

$$CRF = \frac{\Delta I_L}{I_o} = 30\% \tag{3.23}$$

Voltage Ripple Factor: The voltage ripple factor is used to measure the converter's DC side harmonics.

$$VRF = \frac{\Delta V_o}{V_o} = 5\% \tag{3.24}$$

Capacitor Voltage Ripple: The result of the inductor's ripple current pouring into the bypass capacitor.

$$\Delta V_c = \frac{I \times D}{f_s C} \tag{3.25}$$

Switching Frequency: The frequency range for low power applications is typically 20–40 kHz medium. Consequently, the switching frequency used to evaluate the MPPT's performance is set at 25 KHz. Larger frequencies result in greater switching loss; hence, a moderate frequency was chosen to effectively address such issues.

In this system to test the MPPT of the system an input voltage of 156.8V, output voltage 178.8V and power of 600W is taken. The input voltage of 156.8V is within the typical operating range of a solar panel array under standard test conditions (STC) of 1000 W/m2 irradiance and 25°C cell temperature. This ensures the testing of the MPPT performance under operating voltages. The output voltage of 178.8V, which is around 14% higher than the input, falls within the expected voltage boost range that MPPT techniques can provide (Kchaou et al., 2017).

Step 1: Calculate the duty cycle

$$D = 1 - \frac{V_{in}}{V_{out}} = 1 - \frac{156.8}{178.8} = 0.12 \tag{3.26}$$

Step 2: Calculate ripple current

$$\Delta I_L = 0.25 \times \frac{P_{out}}{V_{out}} = 0.25 \times \frac{600}{178.8} = 0.84 \tag{3.27}$$

Step 3: Calculate L_{min}

$$L_{\min} = \frac{\left(1 - D^2\right) D \times R}{2 f_s} = \frac{\left(1 - 0.12^2\right) \times 0.12 \times 53}{2 \times 25000} = 0.0181 mH \tag{3.28}$$

Step 4: Calculate ripple voltage

$$V_{ripple} = 5\% V_o = 0.05 \times 178.8 = 8.94 \tag{3.29}$$

Step 5: Calculate C_{min}

$$C \min = \frac{D}{2 f_s \times R} = \frac{0.12}{2 \times 25000 \times 53} = 0.04528 \mu F \tag{3.30}$$

Step 6: Calculate load resistance R

$$R = \frac{V_{out}}{I_{out}} = \frac{178.8}{3.356} = 53\Omega \tag{3.31}$$

Table 3.1: Summary of boost converter parameters

Parameters	Symbol	Value
Highest possible input voltage	V_{inm}	156.8V
Lowest possible output voltage	V_{om}	178.8V
Highest possible input current	I_{inm}	3.83A
Highest possible output current	I_{om}	3.356A
Duty ratio at the highest power output	D_{mp}	0.12
Switching frequency	f_s	25kHz
Output filter capacitor	C_{dc}	0.4676mF
Inductance	L	1.1478mH
Load resistance	R	53Ω

3.7 Battery Model

An independent solar power system simulation, in which power balance between generation and demand is maintained, heavily relies on battery modeling. Batteries in general can be represented by three models: the equivalent circuit model, the electrochemical model, and the experimental model. However, the equivalent circuit model, which is best suited for dynamic simulation, makes the assumption that the battery is made up of a series resistance and a controlled voltage source, as seen in Figure below. This work uses a basic lead-acid battery model since it is more cost-effective and readily available in larger sizes for renewable energy systems. Modeling a lead-acid battery using the charging and discharging equation is a widely accepted method for simulating sources of renewable energy, like solar and for use in electric vehicle applications (Senapati et al., 2019).

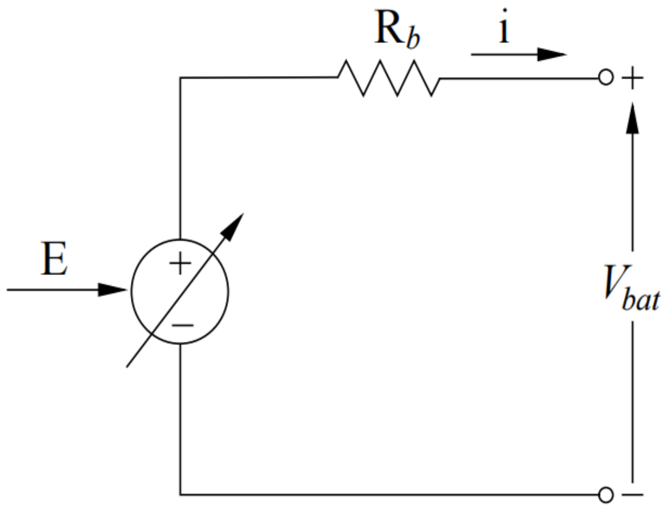

Figure 3.9: Battery equivalent circuit (Li et al., 2013)

Using the analogous circuit above, we can write:

$$V_{bat} = E - R_b i \tag{3.32}$$

Where:
For discharging:

$$E = E_0 - K \frac{Q}{Q-it} \times it - K \frac{Q}{Q-it} \times i * + Exp(t) \tag{3.33}$$

For charging:

$$E = E_0 - K \frac{Q}{Q-it} \times it - K \frac{Q}{it - 0.1Q} \times i * + Exp(t) \tag{3.34}$$

$$E\dot{x}p(t) = B|i(t)|(-Exp(t) + A \times u(t)) \tag{3.35}$$

Where:
V_{bat} Battery's actual voltage at a given time (V), E denotes controlled voltage (V), i represent the charging or discharging current of the battery (A), internal resistance of the battery (Ω) is denoted by R_b, E_0 denotes constant open circuit potential (V), $i*$ represents filtered battery current (A), it actual battery charge, K polarization constant (V/Ah), Q battery capacity (Ah), A exponential zone amplitude (V) , B denotes exponential zone time constant inverse $(Ah)^{-1}$, $Exp(t)$ represents exponential zone voltage (V), $i(t)$ represents battery current, $u(t)$

represents charge or discharge mode ($u(t)$ =0 for discharge mode and $u(t)$ =1 for charge mode).

3.7.1 Battery and PV Array Size for Multi-Service Access Node

It was necessary to determine the load's power usage in order to size the battery bank. Systems that are stand-alone are designed with batteries that can store the energy generated by the array and use it as needed by the system loads. The power consuming load in this thesis study is Multi-Service Access Node, which is rated as 1kW load. Multi-service access nodes, or MSANs, are essential for combining data from several access channels and continuously delivering convergent network services. These nodes must operate continuously for 24 hours a day; hence a continuous backup power source is required. To achieve continuous power supply for this system battery is designed so that it is able to supply power 18hrs per day. In the remaining hours it is assumed that PV arrays is enough to supply power. The required battery capacity, and quantity as well are calculated as following:

$$Total\ load\ =\ 1kW. \tag{3.36}$$

$$Energy\ consumed\ per-day\ =\ 1000wx18hr\ =\ 18,000Whr \tag{3.37}$$

A battery that can supply 18,000Whr is needed for the given load every single day. But we want to have enough time for buck-up or days of autonomy. So, typically a good figure is 2 days of autonomy. Therefore, total battery capacity must be able to supply:

18,000Whrx2 = 36,000Whr.

In this paper 60V, 120Ah Lead-Acid battery is selected. A single battery of this kind can supply: 60Vx120Ah = 7200Whr. Number of batteries required = 36,000Whr/7200Whr = 5. Therefore, to supply a continuous power for MSAN we need 5, 60V,120Ahr batteries. Accordingly, the PV array that can charge 36,000Whr must be designed for charging of the batteries. The total PV size required for charging the battery and instant supply of power to the load can be calculated by summing up the PV size needed for battery charging and instant supply of power to the load. Assume there is 6hr sunshine per-day. Therefore, the PV array wattage is designed as:

$$PV_{power} = \text{total battery energy per-day/sunshine hours+} \\ \text{PV for instant power supply} \tag{3.38}$$

$$PV_{power} = 36{,}000Wh / 6hr + \frac{1kw \times 6hr}{6hr} = 7000W \tag{3.39}$$

3.8 Mathematical Modeling of Bidirectional DC-DC Converter

Buck and boost converters are combined to provide a bi-directional dc-dc converter topology. The core functionality of a bidirectional DC-DC converter is achieved through three distinct building blocks: the modulator, the controller, and the power stage (plant). In this case, a suggested modeling technique is applied that starts with the independent modeling of each component and ends with their combination into a whole model.

State-space averaging was utilized to represent the power stage. The controllers are then designed after that. All the transfer functions needed for design are produced by the combined small-signal model. A buck and a boost converter are combined in a half-bridge design to provide a non-isolated bi-directional dc-dc converter. While charging the battery, this converter lowers the voltage and performs the duties of a buck converter. As the battery is draining, it increases voltage and acts as a boost converter. Figure 3.10 displays the schematic diagram for the bidirectional DC-DC converter. Continuous conduction mode of the converter is assumed. To facilitate energy transfer, a bidirectional DC-DC converter is positioned between DC-bus and battery storage.

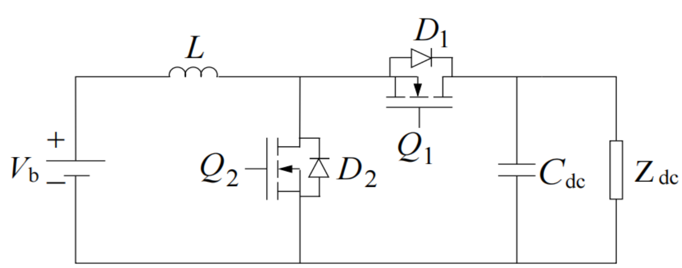

Figure 3.10: Diagram for non-isolated bidirectional converter circuit (R. D. Bhagiya & Patel2019)

From the above Figure:

- ✓ V_b represents battery voltage.
- ✓ Z_{dc} represents internal resistance of the DC-bus

- ✓ C_{dc} represents DC-bus side capacitor
- ✓ Q_1 and Q_2 are MOSFET switches
- ✓ L represents inductor
- ✓ D1 and D2 represent freewheel diodes

The circuit depicted in Figure 3.10 has been considered for the state-space modeling of a bidirectional DC-DC converter. There are two main modes of operation for it: boost mode and buck mode. Once more, there are four subintervals in these two modes, which vary according to the MOSFETs' and diodes' ON and OFF states. However, of the four states in this circuit, two are the same as the other two. Therefore, depending on the MOSFETs' ON/OFF state, the following two states are used for state-space modeling.

A. Step-up Mode

This mode of operation can be used when battery discharges power to a connected DC bus load. Voltage step-up mode is used by the converter. Q1 and D2 are always off, however Q2 and diode D1 can be switched on and off based on the duty cycle. Two sub-intervals can be identified within this mode based on the conduction of Q2 and D1.

First Interval: D1 off Q1 off D2 off. A low-voltage battery charges the inductor in this mode, and the current flows through the inductor continuously until the gate pulse from the Q2 is eliminated. Furthermore, switch Q1 is in an off state and no current flows through it due to the reverse bias of diode D1.

Second Interval: Q1-off, D1-on; Q2-off, D2-off. In this state, Q2 and Q1 are both off, therefore they can be thought of as open circuits. Now that the inductor's current cannot vary rapidly, the voltage across it reverses polarity and in response to the input voltage, the inductor starts to operate in series. The diode D1's forward bias causes the output capacitor Cdc to have a greater voltage, which is why the inductor current charges it. This causes an increase of voltage output. The step-up mode equivalent circuit for a bi-directional converter, as illustrated in Figure 3.11

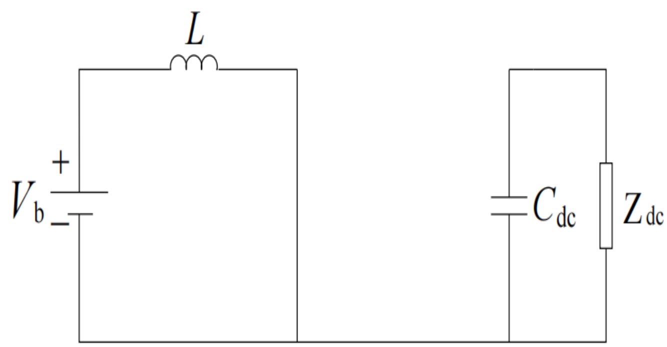

Figure 3.11: Circuit diagram during step-up mode(R. D. Bhagiya & Patel, 2019)

The KVL and KCL formulas are used to generate the following equations based on the circuit above with the switch Q2 only turned on.

$$\begin{aligned} L\frac{di_L}{dt} &= V_b \\ C_{dc}\frac{dV_{dc}}{dt} &= -\frac{V_{dc}}{Z_{dc}} \end{aligned} \tag{3.40}$$

After re-arranging the equations above:

$$\begin{aligned} \frac{di_L}{dt} &= \frac{V_b}{L} \\ \frac{dV_{dc}}{dt} &= -\frac{V_{dc}}{C_{dc}\times Z_{dc}} \end{aligned} \tag{3.41}$$

Writing the above equations into state space representation:

$$\begin{aligned} \dot{X} &= A_1X + B_1U \\ Y &= C_1X + E_1U \end{aligned} \tag{3.42}$$

Let $i_L=x_1$ and $V_{dc}=x_2$,

$$\begin{aligned} \begin{bmatrix} \dot{x}_1 \\ \dot{x}_2 \end{bmatrix} &= \begin{bmatrix} 0 & 0 \\ 0 & \dfrac{-1}{C_{dc}Z_{dc}} \end{bmatrix} \begin{bmatrix} x_1 \\ x_2 \end{bmatrix} + \begin{bmatrix} \dfrac{1}{L} \\ 0 \end{bmatrix} [V_b] \\ Y &= [0 \quad 1]\left[\begin{bmatrix} x_1 \\ x_2 \end{bmatrix}\right] \end{aligned} \tag{3.43}$$

$$A_1 = \begin{bmatrix} 0 & 0 \\ 0 & \dfrac{-1}{C_{dc}Z_{dc}} \end{bmatrix} \quad B_1 = \begin{bmatrix} \dfrac{1}{L} \\ 0 \end{bmatrix} \; C_1 = \begin{bmatrix} 0 & 1 \end{bmatrix} \; E_1 = 0 \tag{3.44}$$

B. Step-down Mode

Diode D2 and switch Q1 can conduct depending on the duty cycle, but switch Q2 and diode D1 remain always off in this mode. This mode can be further divided into two stages depending on whether switch Q1 or diode D2 conducts electricity.

First Interval: (Q1-on, D1-off; Q2-off, D2-Off) Q1 is ON in this mode, therefore it may be said that there is a short circuit. With the higher voltage bus charging the inductor, the output capacitor will be charged.

Second interval: (Q1, D1 and Q2-off, and D2-on). Q2 and Q1 are both off in this mode. Again, because the inductor current is not changeable instantaneously, the freewheeling diode D2 discharges it. In relation to the input voltage, a step-down in the voltage across the load occurs. Figure 3.12 illustrates this step-down method of operation.

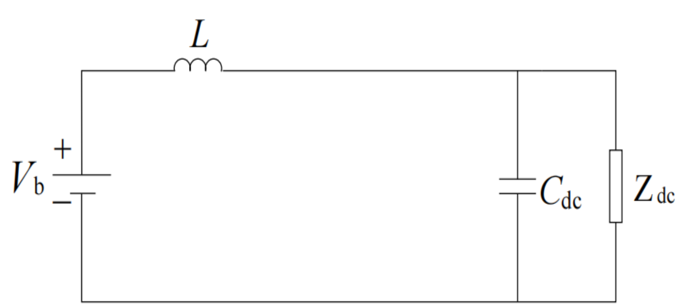

Figure 3.12: Circuit diagram during step-down mode(R. D. Bhagiya & Patel, 2019)

The KVL and KCL formulas are used to get the following equations for the circuit shown above when switch Q1 is only on.

$$\left. \begin{aligned} L\frac{di_L}{dt} &= V_b - V_{dc} \\ C_{dc}\frac{dV_{dc}}{dt} &= i_L - \frac{V_{dc}}{Z_{dc}} \end{aligned} \right) \tag{3.45}$$

$$Y = V_{dc}$$

After re-arranging the above equations:

$$\left.\begin{aligned}\frac{di_L}{dt} &= \frac{V_b}{L} - \frac{V_{dc}}{L}\\ \frac{dV_{dc}}{dt} &= \frac{i_L}{C_{dc}} - \frac{V_{dc}}{C_{dc}Z_{dc}}\end{aligned}\right) \tag{3.46}$$

Writing the above equations into state space representation:

$$\begin{aligned}\dot{X} &= A_2X + B_2U\\ Y &= C_2X + DU\end{aligned} \tag{3.47}$$

Let $i_L = x_1$ and $V_{dc} = x_2$,

$$\begin{aligned}\begin{bmatrix}\dot{x}_1\\ \dot{x}_2\end{bmatrix} &= \begin{bmatrix}0 & \dfrac{-1}{L}\\ \dfrac{1}{C_{dc}} & \dfrac{-1}{C_{dc}Z_{dc}}\end{bmatrix}\begin{bmatrix}x_1\\ x_2\end{bmatrix} + \begin{bmatrix}\dfrac{1}{L}\\ 0\end{bmatrix}\left[V_b\right]\\ Y &= \begin{bmatrix}0 & 1\end{bmatrix}\begin{bmatrix}x_1\\ x_2\end{bmatrix}\end{aligned} \tag{3.48}$$

$$A_2 = \begin{bmatrix}0 & \dfrac{-1}{L}\\ \dfrac{1}{C_{dc}} & \dfrac{-1}{C_{dc}Z_{dc}}\end{bmatrix} \quad \begin{bmatrix}\dfrac{1}{L}\\ 0\end{bmatrix} = B_2 \quad C_2 = [0\ \ 1] \qquad E_2 = 0 \tag{3.49}$$

State Space Average Model:

To obtain the state space average, we take the average of the state equation across a single switching cycle. Assume that the switches close for dT seconds and open for (1-d) T seconds. Then the average quantity is represented as:

$$\left\langle \dot{x} \right\rangle\Big|_{Ts} = \left(dA_1 + \left(1-d\right)A_2\right)\left\langle x\right\rangle_{|Ts} + \left(dB_1 + \left(1-d\right)B_2\right)\left\langle u_{in}\right\rangle\Big|_{Ts} = Fav \tag{3.50}$$

Let's add the perturbation to the above model. Then

$$\begin{aligned}\left\langle x \right\rangle &= X + \hat{x}\\ \left\langle u_{in}\right\rangle &= U + \hat{u}\\ \left\langle d\right\rangle &= D + \hat{d}\end{aligned} \tag{3.51}$$

Where, X, U, and D are steady state values of state variables and input signal.

Then Equation (3.50) becomes:

$$\begin{aligned}&\frac{d}{dt}\left(X+\hat{x}\right)=\left(\left(D+\hat{d}\right)A_1+\left(1-\left(D+\hat{d}\right)\right)A_2\right)\left(X+\hat{x}\right)_{Ts}+\\&\left(\left(D+\hat{d}\right)B_1+\left(1-\left(D+\hat{d}\right)\right)B_2\right)\left(U_{in}+\hat{u}\right)_{Ts}\end{aligned} \tag{3.52}$$

The derivative of the steady state values are zeros. Then after re-arranging Equation (3.52), Equation (3.53) is obtained.

$$\dot{\hat{x}}=Fav|_{ss}+\frac{\partial Fav}{\partial x}|_{ss}\ \hat{x}+\frac{\partial Fav}{\partial d}|_{ss}\ \hat{d}+\frac{\partial Fav}{\partial u_{in}}|_{ss}\ \hat{u}_{in} \tag{3.53}$$

$$Fav|_{ss}=0=\left(DA_1+\left(1-D\right)A_2\right)X+\left(DB_1+\left(1-D\right)B_2\right)u \tag{3.54}$$

Let’s say

$$\begin{aligned}&DA_1+\left(1-D\right)A_2=A \quad and\\&DB_1+\left(1-D\right)B_2=B\end{aligned} \tag{3.55}$$

$$A=D\begin{bmatrix}0 & 0\\ 0 & \dfrac{-1}{C_{dc}Z_{dc}}\end{bmatrix}+\left(1-D\right)\begin{bmatrix}0 & \dfrac{-1}{L}\\ \dfrac{1}{C_{dc}} & \dfrac{-1}{C_{dc}Z_{dc}}\end{bmatrix}=\begin{bmatrix}0 & \dfrac{-(1-D)}{L}\\ \dfrac{(1-D)}{C_{dc}} & \dfrac{-1}{C_{dc}Z_{dc}}\end{bmatrix} \tag{3.56}$$

$$B=D\begin{bmatrix}\dfrac{1}{L}\\ 0\end{bmatrix}+\left(1-D\right)\begin{bmatrix}\dfrac{1}{L}\\ 0\end{bmatrix}=\begin{bmatrix}\dfrac{1}{L}\\ 0\end{bmatrix} \tag{3.57}$$

$$\begin{aligned}&C=DC_1+(1-D)C_2 \quad D=\begin{bmatrix}0 & 1\end{bmatrix}+(1-D)\begin{bmatrix}0 & 1\end{bmatrix}=\begin{bmatrix}0 & 1\end{bmatrix}\\&E=DE_1+(1-D)E_2=0\end{aligned} \tag{3.58}$$

Consequently, Equation (3.50)'s solution becomes:

$$X=-A^{-}BU_{in} \tag{3.59}$$

Where:

$$X=\begin{bmatrix}X_1\\ X_2\end{bmatrix} and\, U_{in}=\begin{bmatrix}V_b\end{bmatrix} \tag{3.60}$$

$$\det A = \frac{(1-D)^2}{LC_{dc}}, \quad A^{-1} = \frac{1}{\det A}\begin{bmatrix} \frac{-1}{C_{dc}Z_{dc}} & \frac{(1-D)}{L} \\ \frac{-(1-D)}{C_{dc}} & 0 \end{bmatrix} = \begin{bmatrix} \frac{-L}{(1-D)^2 Z_{dc}} & \frac{C_{dc}}{(1-D)} \\ \frac{-L}{(1-D)} & 0 \end{bmatrix} \tag{3.61}$$

$$\begin{bmatrix} I_L \\ V_{dc} \end{bmatrix} = -A^{-1}BV_b = -\begin{bmatrix} \frac{-L}{(1-D)^2 Z_{dc}} & \frac{C_{dc}}{(1-D)} \\ \frac{-L}{(1-D)} & 0 \end{bmatrix}\begin{bmatrix} \frac{1}{L} \\ 0 \end{bmatrix} V_b \tag{3.62}$$

$$\begin{aligned} I_L &= \frac{V_b}{\left(1-D\right)^2 Z_{dc}} \\ V_{dc} &= \frac{V_b}{\left(1-D\right)} \end{aligned} \tag{3.63}$$

From Equation (3.53)

$$\begin{gathered} \frac{\partial Fav}{\partial x}|_{ss} = \frac{\partial}{\partial x}\left(\left(dA_1 + \left(1-d\right)A_2\right)\left\langle x\right\rangle_{|Ts} + \left(dB_1 + \left(1-d\right)B_2\right)\left\langle u_{in}\right\rangle|_{Ts}\right) = \\ DA_1 + \left(1-D\right)A_2 = A = \begin{bmatrix} 0 & \frac{-(1-D)}{L} \\ \frac{(1-D)}{C_{dc}} & \frac{-1}{C_{dc}Z_{dc}} \end{bmatrix} \end{gathered} \tag{3.64}$$

Therefore,

$$\frac{\partial Fav}{\partial x}|_{ss}\ \hat{x} = \begin{bmatrix} 0 & \frac{-(1-D)}{L} \\ \frac{(1-D)}{C_{dc}} & \frac{-1}{C_{dc}Z_{dc}} \end{bmatrix}\begin{bmatrix} \hat{x}_1 \\ \hat{x}_2 \end{bmatrix} \tag{3.65}$$

From Equation (3.53)

$$\frac{\partial Fav}{\partial d}|_{ss} = \left(A_1 - A_2\right)X + \left(B_1 - B_2\right)U_{in} = \begin{bmatrix} 0 & \frac{1}{L} \\ \frac{-1}{C_{dc}} & 0 \end{bmatrix}\begin{bmatrix} X_1 \\ X_2 \end{bmatrix} \tag{3.66}$$

Therefore,

$$\frac{\partial Fav}{\partial d}|_{ss}\ \hat{d} = \begin{bmatrix} 0 & \frac{1}{L} \\ \frac{-1}{C_{dc}} & 0 \end{bmatrix}\begin{bmatrix} X_1 \\ X_2 \end{bmatrix}\hat{d} \tag{3.67}$$

From Equation (3.53)

$$\frac{\partial Fav}{\partial u_{in}}|_{ss} = DB_1 + (1-D)B_2 = (B_1 - B_2)D + B_2 = \begin{bmatrix} \frac{1}{L} \\ 0 \end{bmatrix} \tag{3.68}$$

Finally, according to Equation (3.53) the AC model of the bidirectional converter is represented as below:

$$\begin{bmatrix} \dot{\hat{x}}_1 \\ \dot{\hat{x}}_2 \end{bmatrix} = \begin{bmatrix} 0 & \frac{-(1-D)}{L} \\ \frac{(1-D)}{C_{dc}} & \frac{-1}{C_{dc}Z_{dc}} \end{bmatrix}\begin{bmatrix} \hat{x}_1 \\ \hat{x}_2 \end{bmatrix} + \begin{bmatrix} 0 & \frac{1}{L} \\ \frac{-1}{C_{dc}} & 0 \end{bmatrix}\begin{bmatrix} X_1 \\ X_2 \end{bmatrix}\hat{d} + \begin{bmatrix} \frac{1}{L} \\ 0 \end{bmatrix}\hat{v}_b \tag{3.69}$$

Assume zero input perturbation, then the above Equation (3.69) is simplified to:

$$\begin{bmatrix} \dot{\hat{x}}_1 \\ \dot{\hat{x}}_2 \end{bmatrix} = \begin{bmatrix} 0 & \frac{-(1-D)}{L} \\ \frac{(1-D)}{C_{dc}} & \frac{-1}{C_{dc}Z_{dc}} \end{bmatrix}\begin{bmatrix} \hat{x}_1 \\ \hat{x}_2 \end{bmatrix} + \begin{bmatrix} 0 & \frac{1}{L} \\ \frac{-1}{C_{dc}} & 0 \end{bmatrix}\begin{bmatrix} X_1 \\ X_2 \end{bmatrix}\hat{d} \tag{3.70}$$

Taking the Laplace transform of Equation (3.70)

$$sx(s) = Ax(s) + B'd(s) \tag{3.71}$$

Where:

$$B' = \begin{bmatrix} 0 & \frac{1}{L} \\ \frac{-1}{C_{dc}} & 0 \end{bmatrix}\begin{bmatrix} X_1 \\ X_2 \end{bmatrix} \tag{3.72}$$

Then,

$$x(s) = (sI - A)^{-1}B'd(s) \tag{3.73}$$

$$x(s)=\begin{bmatrix} \dfrac{(C_{dc}Z_{dc}s+1)LC_{dc}}{(C_{dc}Z_{dc}s^2+s)LC_{dc}+C_{dc}Z_{dc}(1-D)^2} & \dfrac{-(1-D)C^2{}_{dc}Z_{dc}}{(C_{dc}Z_{dc}s^2+s)LC_{dc}+C_{dc}Z_{dc}(1-D)^2} \\ \dfrac{-C_{dc}Z_{dc}L(1-D)}{(C_{dc}Z_{dc}s^2+s)LC_{dc}+C_{dc}Z_{dc}(1-D)^2} & \dfrac{C^2{}_{dc}Z_{dc}Ls}{(C_{dc}Z_{dc}s^2+s)LC_{dc}+C_{dc}Z_{dc}(1-D)^2} \end{bmatrix} \begin{bmatrix} \dfrac{X_2}{L} \\ \dfrac{-X_1}{C_{dc}} \end{bmatrix} d(s) \quad (3.74)$$

The DC-DC bidirectional battery converter's transfer function, Gid(s), between the inductor current and the control input is: Gvi(s), between DC-load bus voltage and inductor current is derived from the DC-DC bidirectional converter's linearized average state-space equations:

$$Gid(s)=\frac{i_L(s)}{d(s)}=\frac{X_2Z_{dc}C_{dc}S+X_2+(1-D)Z_{dc}X_1}{LZ_{dc}C_{dc}S^2+LS+(1-D)^2Z_{dc}} \quad (3.75)$$

$$\hat{y}=C\hat{x}+E\hat{u}$$

However, E=0. Therefore,

$$\begin{aligned}\hat{y}&=C\hat{x}\\ y(s)&=Cx(s)\end{aligned} \quad (3.76)$$

Substituting Equations (3.58) and (3.74) into Equation (3.76) the transfer function from inductor current to DC-bus voltage is obtained as:

$$\frac{V_{dc}(s)}{i_L(s)}=\frac{Z_{dc}V_{dc}(1-D)-Z_{dc}Li_Ls}{C_{dc}Z_{dc}V_{dc}s+V_{dc}+(1-D)Z_{dc}i_L} \quad (3.77)$$

3.9 Mathematical Modeling of Buck-converter

The average DC output voltage (Vo) of a step-down or buck converter is lower than the input unregulated DC voltage (Vs). As a result, it is a converter that steps up current and steps down voltage. Figure 3.13 following displays a circuit diagram that has been simplified.

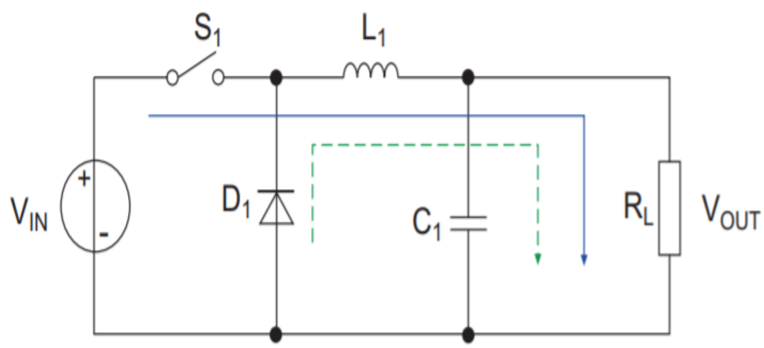

Figure 3.13: A schematic of the buck converter (Rajvir Kaur, 2020)

The transfer function of a buck converter can be derived by considering the balance of voltage across the inductor during its "on" and "off" state. Due to the energy conservation principle, the products so acquired under ON and OFF situations must be the same. Energy calculations in the ON state:

$$E_{in} = (V_{in} - V_{out})t_{on} \tag{3.78}$$

Equations for energy in the off-condition:

$$E_{out} = V_{out} t_{off} \tag{3.79}$$

$$D = \frac{t_{on}}{T} = \frac{t_{on}}{t_{on} + t_{off}} \tag{3.80}$$

Using Equation (3.80)

$$(V_{in} - V_{out})t_{on} = V_{out}(T - t_{on}) \tag{3.81}$$

$$V_{out} = V_{in}\frac{t_{on}}{T} = DV_{in} \tag{3.82}$$

If every component is ideal, the circuit should have no internal resistance and energy-free components. Using the averaging approach, the following can be obtained. When the switch is in the ON state the dynamics of the converter is given by 0<t<dT:

$$\begin{aligned} \frac{di_L}{dt} &= \frac{1}{L}(V_o - V_{in}) \\ \frac{dV_o}{dt} &= \frac{1}{C}\left(i_L - \frac{V_o}{R}\right) \end{aligned} \tag{3.83}$$

$$\dot{X} = A_1 X + B_1 U$$
$$Y = C_1 X + D_1 U \tag{3.84}$$

Let $i_L = x_1$ and $V_o = x_2$,

$$\begin{bmatrix} \dot{x}_1 \\ \dot{x}_2 \end{bmatrix} = \begin{bmatrix} 0 & \frac{1}{L} \\ \frac{1}{C} & \frac{-1}{RC} \end{bmatrix} \begin{bmatrix} x_1 \\ x_2 \end{bmatrix} + \begin{bmatrix} \frac{-1}{L} \\ 0 \end{bmatrix} [V_{in}]$$
$$Y = [0 \quad 1]\left[\begin{bmatrix} x_1 \\ x_2 \end{bmatrix}\right] \tag{3.85}$$

$$A_1 = \begin{bmatrix} 0 & \frac{1}{L} \\ \frac{1}{C} & \frac{-1}{RC} \end{bmatrix} \quad B_1 = \begin{bmatrix} \frac{-1}{L} \\ 0 \end{bmatrix} \quad C_1 = [0 \quad 1] \tag{3.86}$$

When the switch is in the OFF state the dynamics of the converter is given by $dT<t<T$:

$$\frac{di_L}{dt} = \frac{1}{L}(V_o)$$
$$\frac{dV_o}{dt} = \frac{1}{C}\left(i_L - \frac{V_o}{R}\right) \tag{3.87}$$

$$\dot{X} = A_2 X + B_2 U$$
$$Y = C_2 X + D_2 U \tag{3.88}$$

$$A_2 = \begin{bmatrix} 0 & \frac{1}{L} \\ \frac{1}{C} & \frac{-1}{RC} \end{bmatrix} \quad B_2 = 0 \quad C_2 = [0 \quad 1] \quad D_2 = 0 \tag{3.89}$$

State Space Average Model

By averaging the previously calculated state equation during the switching cycle, the state space average is produced. Assume that the switches close for dT seconds and open for (1-d) T seconds. Then the average quantity is represented as:

$$\left\langle \dot{x} \right\rangle\Big|_{Ts} = \left(dA_1 + (1-d)A_2\right)\langle x \rangle_{|Ts} + \left(dB_1 + (1-d)B_2\right)\langle u_{in} \rangle\Big|_{Ts} = Fav \tag{3.90}$$

But, $A_1=A_2$ and $B_2=0$ therefore, Equation (3.90) is simplified as:

$$\left\langle \dot{x} \right\rangle\Big|_{Ts} = \left(A_2\right)\left\langle x\right\rangle_{|Ts} + \left(dB_1\right)\left\langle u_{in}\right\rangle\Big|_{Ts} = Fav \tag{3.91}$$

$$\left\langle \begin{matrix} \dot{x}_1 \\ \dot{x}_2 \end{matrix} \right\rangle = \begin{bmatrix} 0 & \dfrac{1}{L} \\ \dfrac{1}{C} & \dfrac{-1}{RC} \end{bmatrix} \left\langle \begin{matrix} x_1 \\ x_2 \end{matrix} \right\rangle + \begin{bmatrix} \dfrac{-1}{L} \\ 0 \end{bmatrix} V_{in} d$$

$$y = [0 \quad 1] \left\langle \begin{matrix} x_1 \\ x_2 \end{matrix} \right\rangle \tag{3.92}$$

CHAPTER FOUR

4. CONTROLLER DESIGN

4.1 PID Control System

Proportional gain (Kp), integral gain (Ki) and derivative are the three control parameters of the PID controller. In order for the PID controller to function better, it has three control parameters: integral gain (Ki), derivative gain and proportional gain (Kp). The methods used to find the optimal control parameter are referred to as tuning. The mathematical expressions for the PID control algorithm are shown in Equation (4.1) and (4.2).

$$u(t) = K\left(e(t) + \frac{1}{Ti}\int_0^t e(t)d\tau + Td\,\frac{de(t)}{dt} \right) \tag{4.1}$$

$$u(t) = K_p e(t) + K_i \int_o^t e(t)d\tau + Kd\,\frac{\mathrm{de}(t)}{dt} \tag{4.2}$$

In this equation, u(t) represents the control variable, while e(t) signifies an error between the reference value and the actual value. The proportional term (Kp) provides a response proportional to the current error, leading to faster correction. The integral term (Ki) accumulates the error over time, reducing any remaining error at steady state. Four key parameters (rising time, settling time, steady-state error, and overshoot) are used to assess the performance of a DC-DC converter controller**.** These parameters evaluate how effectively the controller regulates the output voltage within a specified range.

4.1.1 Design of PSO-based PID Controller Parameters

Inspired by nature**:** PSO (Particle Swarm Optimization) emerged from simulating the fascinating behavior of birds flocking together in two dimensions. Focusing on movement: PSO utilizes a swarm of particles, representing potential solutions, that navigate the search space to discover the optimal outcome. As this is going on, every particle in their path is searching for the right particle, or gBest, which is the optimal solution. Individual particles in PSO learn from each other by considering not only their own best findings but also the best solution encountered by the entire swarm. Each particle considers its current location, velocity, and its distance to both its own best solution (pBest) and the swarm's best solution (gBest). Based on this information, it adjusts its position in the search space (Radosavljević et al., 2016). Mathematically, the PSO can be expressed using (Radosavljević et al., 2016)

$$v_i^k(t+1) = w(t)v_i^k(t) + C_1 r_1(pBest_i^k(t) - x_i^k(t)) + C_2 r_2(gBest^k(t) - x_i^k(t)) \tag{4.3}$$

$$x_i^k(t+1) = x_i^k(t) + v_i^k(t+1) \tag{4.4}$$

$$w(t) = \frac{(t_{\max} - t)(w_{\max} - w_{\min})}{(t_{\max} - 1) + w_{\min}} \tag{4.5}$$

Where w(t) representing the weighting factor of inertia, the random values r1, r2 are evenly distributed in the interval from 0 to 1, whereas C1 and C2 are acceleration factors. Where: x_i^k (t) representing the position of the i^{th} particle of the k^{th} variable at time t, v_i^k (t) represent the velocity i^{th} of particle of k^{th} variable at time (iteration) t. The four objective functions listed below will have their costs minimized by using the PSO algorithm:

$$\begin{aligned} IAE &= \int_0^\infty |e(t)|\,dt \\ ISE &= \int_0^\infty e^2(t)dt \\ ITSE &= \int_0^\infty te^2(t)dt \\ ISTSE &= \int_0^\infty t^2e^2(t)dt \end{aligned} \tag{4.6}$$

Where;

e(t) = Reference minus Actual measured value.

IAE will be utilized, in principle, to suppress the smallest errors between reference value and actual value. IAE uses the errors' absolute value in this process. Because ISE squared the error, it will simultaneously eliminate the significant errors. Because ITSE integrates the time parameter linearly, it may result in a longer settling time, but it is useful to minimize the rising time with relatively modest overshoot. That being said, because ISTSE squares the time, it will help to reduce the steady state error and settling time (Jie Mei & James L. Kirtley, 2018). The optimization problem has the following short form when expressed mathematically.

Objective function:

$$\begin{aligned} F_1 &= \min\left|\int_0^\infty |e(t)|\,dt\right| \\ F_2 &= \min\left|\int_0^\infty e^2(t)dt\right| \\ F_3 &= \min\left|\int_0^\infty te^2(t)dt\right| \\ F_4 &= \min\left|\int_0^\infty t^2e^2(t)dt\right| \end{aligned} \tag{4.7}$$

Subject to:

$$\begin{aligned} K_p^{\min} &\le K_p \le K_p^{\max} \\ K_i^{\min} &\le K_p \le K_i^{\max} \end{aligned} \tag{4.8}$$

In this research study IAE is taken as cost function to optimize the parameters of the controllers.

4.2 Grey Wolf Optimization Algorithm Based MPPT

Monitoring the MPP is essential to getting maximizing the solar power system's potential. For MPPT, there are numerous approaches. The hunting tactics and organizational structure of actual grey wolf packs are imitated by the GWO algorithm. Given their status as apex predators, grey wolves are obligated to live in packs. Grey wolves of four different kinds are used to symbolize the leadership hierarchy: omega (ω), beta (β), delta (δ), and alpha (α). The following Equations can be used to model how a hunt is conducted by grey wolves:

$$\vec{D} = |\vec{C}.\vec{X}p(t) - \vec{X}(t)| \tag{4.9}$$

$$\vec{X}(t+1) = \vec{X}p(t) - \vec{A}\vec{D} \tag{4.10}$$

Where: t is the current iteration, Xp stands for the position vector of the prey, D, A, and C indicate coefficient vectors, and X is the position vector of the grey wolf. The following is how the vectors A and C are computed:

$$\vec{A} = 2\vec{a}.\vec{r}_1 - \vec{a} \tag{4.11}$$

$$\vec{C} = 2.\vec{r}_2 \tag{4.12}$$

where the random vectors r_1, r_2 are in the interval [0, 1]. The hunt is frequently led by alpha, also referred to as leader, with beta and delta following closely behind. Delta might occasionally participate in the search as well. The pack's injured wolves are cared for by omega and delta. Therefore, we identify alpha as the potential solution that finds the prey more accurately. The hunt is terminated when the victim stops moving and is attacked by the grey wolves.

4.2.1 Application of Grey Wolf Optimization for MPPT

In this research, a Grey Wolf Optimization (GWO) with DC-DC boost converter-based maximum power point tracking (MPPT) algorithm for solar photovoltaic (PV) systems is proposed. The PV module's voltage and current are inputs to an MPPT algorithm based on GWO. It tracks the maximum power point for any operating situation by determining a duty cycle of the converter and managing the operating point.

The controller calculates the output power for the number of gray wolves, or duty ratios, by detecting Vpv and Ipv using sensors. Figure 4.1 displays the working of the suggested method. The suggested strategy has been found to be faster than the conventional approaches, with less MPP oscillation. It offers a more effective response to quickly shifting atmospheric conditions

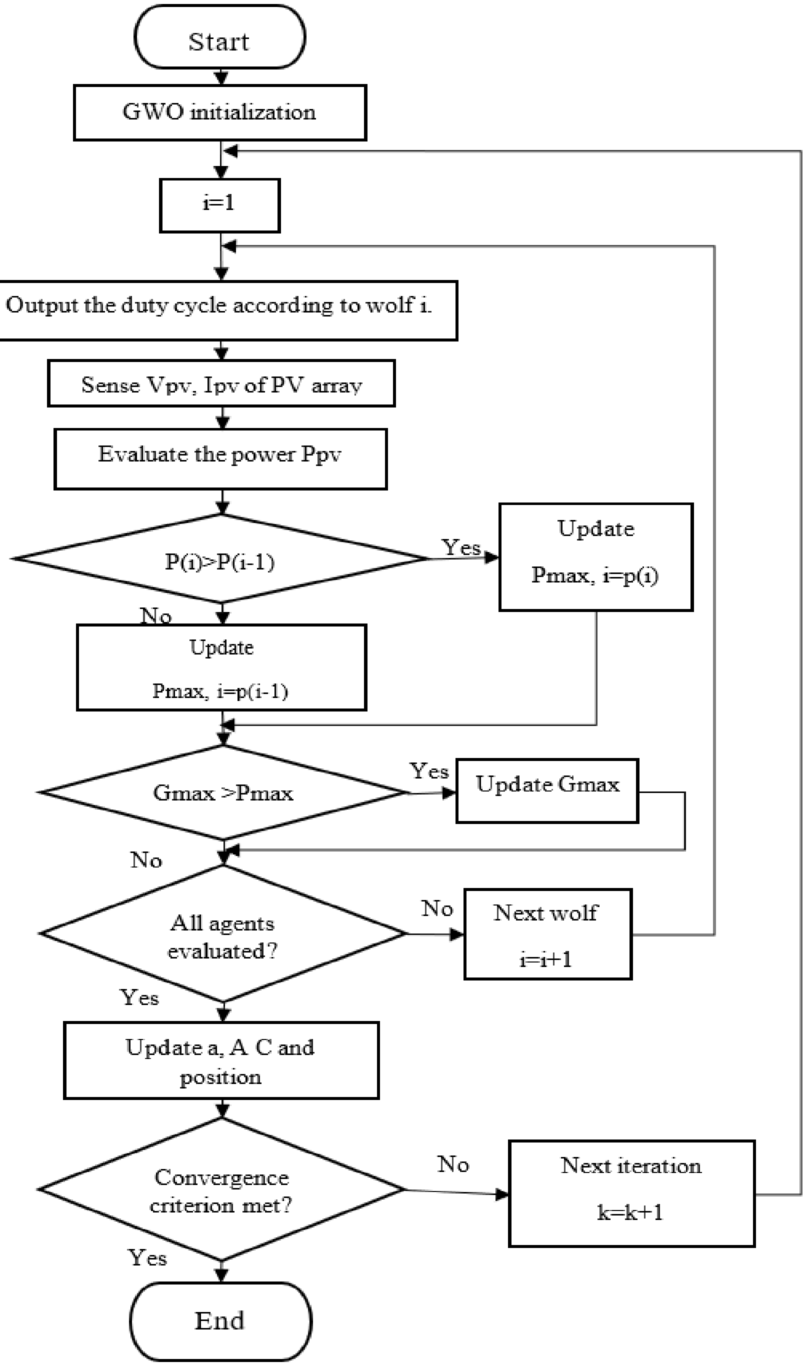

Figure 4.1: Flowchart of the suggested GWO-algorithm

During partial shading, the P-V curve is split into numerous peaks with various local peaks (LPs) and one GP. It is noteworthy that the wolves' associated coefficient vectors almost approach zero when they locate the MPP. The goal of the suggested approach is to integrate direct duty-cycle control with GWO, indicating that at the MPP, the duty cycle is kept constant. As a result, steady-state oscillations that are inherent in conventional MPPT methods are reduced and, ultimately, lowers oscillation-related power loss, leading to increased system efficiency. In order to implement the GWO-algorithm, duty cycle is referred to as a grey wolf. Consequently, can be altered in the way that follows:

$$d_k(i+1) = d_k(i) - A \cdot D \tag{4.13}$$

Fitness function is therefore expressed as:

$$P(d_k^i) > P(d_k^{i-1}) \tag{4.14}$$

The variables P, i, d, and k stand for power, iterations, duty cycle, and wolves, respectively.

4.3 Bidirectional DC-DC Converter Control

In order to compensate for power deficits or excesses in the system and regulate load bus voltage, batteries are interfaced with the DC-bus via a DC-DC bidirectional converter. To control the DC- bus voltage, a two loop PI control mechanism based on pulse width modulation is suggested. The outer loop controls DC-bus voltage, while the inner loop controls inductor current. Figure 4.2 shows double loop control strategy of bidirectional DC-DC converter.

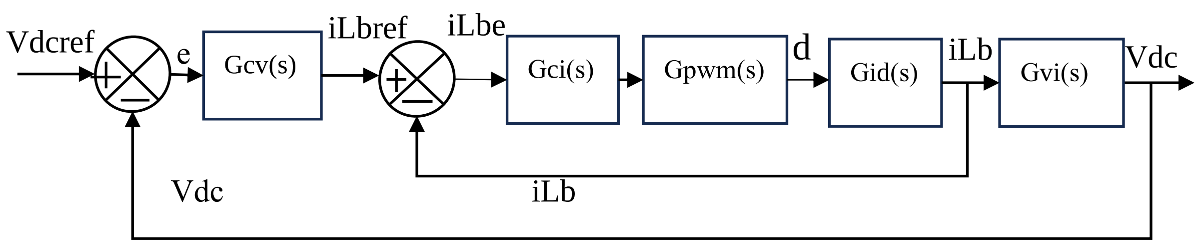

Figure 4.2: The two-loop control strategy block diagram

Where;

V_{dcref} represent reference DC-bus voltage, which is 72V, Vdc is actual DC-bus measured voltage. Gcv(s) is outer loop PI controller transfer function given as:

$$Gcv(s) = kp + \frac{ki}{s} \tag{4.15}$$

i_{Lbref} is reference inductor current, and i_{Lb} actual measured inductor current. i_{Lbe} inductor current error. Gci(s) inner loop PI current controller transfer function given as:

$$Gci(s) = kp + \frac{ki}{s} \tag{4.16}$$

Gpwm(s) is PWM gain taken as 1 in this paper, and d is duty cycle. Gid(s) is transfer function taken from control-inductor current as discussed in Equation (3.75). Gvi(s) represent transfer function defined as inductor current-output voltage as discussed so far in Equation (3.77). The optimal values of PI parameters in both controllers are obtained by Metaheuristic optimization Particle Swarm Optimization technique. The objective function used to optimize the PI parameters is integral of absolute error as mentioned in Equation (4.18), an error being the subtraction of measured DC-bus voltage from reference voltage (72V). By taking constraint as minimum and maximum range of Kp and Ki as [-10,000, 1000] and [-100, 100,000] respectively for outer voltage controller and [-100, 100] and [0, 10,000] for inner current controller the optimized values of Kp and Ki are Kp = 0.7 and 0.0242 and Ki = 100.2 and 99.9582 respectively.

4.4 Buck Converter Control

The buck converter system is intended to use a PID controller. The optimal values of PID parameters are obtained by Particle swarm optimization technique. Considering the steady state values of state variable and from the previously derived state space model of the buck-converter, the system's closed loop transfer function can be derived as below:

$$x(s) = (sI - A)^{-1} Bd(s) \tag{4.17}$$

Where:

$$A = \begin{bmatrix} 0 & \frac{-1}{L} \\ \frac{1}{C} & \frac{-1}{RC} \end{bmatrix} \quad and \quad B = \begin{bmatrix} \frac{d}{L} \\ 0 \end{bmatrix} \tag{4.18}$$

Then the input to output voltage transfer function can be written as:

$$G\,p(s) = \frac{\frac{V_{in}}{LC} Gc(s)}{s^2 + \frac{1}{RC}s + \frac{1}{LC} + \frac{V_{in}}{LC} Gc(s)} \tag{4.19}$$

Figure 4.2 below shows the buck converter closed loop control block diagram.

Where:

- ✓ e represents the error between reference voltage and output voltage
- ✓ u represents control signal generated by PID controller
- ✓ d represents duty cycle
- ✓ Gc(s) represent PID controller’s transfer function as mentioned in Equation (4.2)
- ✓ Gpwm(s) pulse width modulation’s gain, taken as unity.
- ✓ Gp(s) represent buck-converter’s transfer function as mentioned in Equation (4.19)

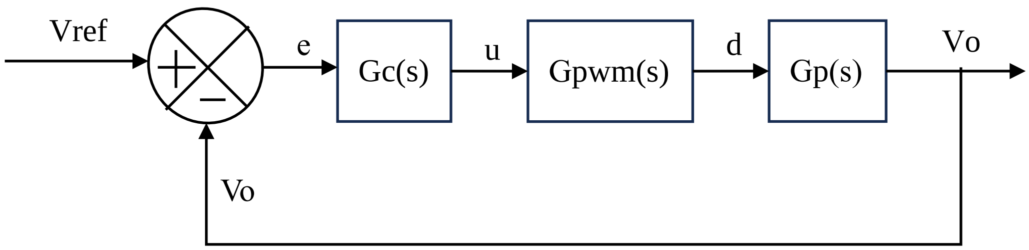

Figure 4.3: Closed loop control of buck-converter

The optimum parameters of the controllers are obtained by PSO-optimization algorithm. To obtain optimal parameters of the controller a swarm of particles is initialized randomly within the search space bounds of the parameters of the controller. Each particle represents a set of Kp and Ki values. The controller with these parameters is used in a system simulation. An error-based objective function integral of absolute error (IAE) is calculated to evaluate the fitness as mentioned in Equation (4.20) below.

$$F_1 = \min \left| \int_0^{\infty} |e(t)| \, dt \right| \tag{4.20}$$

An inertia weight (w) of PSO that balances exploration and exploitation typically starts at 0.9 and decreases linearly to 0.4 (Russell C. Eberhart, 2014). Good values of cognitive and social acceleration factors (C1 and C2) lie between 1 and 3 (Zhan et al., 2009). This paper implemented Particle Swarm Optimization using a linearly decreasing inertia weight schedule between 0.4 and 0.9. Specifically, 0.4 was used as the minimum inertia weight value and 0.9 as the maximum. Additionally, both the cognitive and social acceleration factors (C1 and C2 respectively) were set to the same value of 2. This setting for the inertia weight range and acceleration factors aims to balance the global and local search abilities of the particles over the course of the optimization process.

By taking constraint as minimum and maximum range of Kp, Ki and Kd as [-1000, 10,000,0] and [1000, 10,000, 10,000] respectively the tuned values of Kp, Ki and Kd found are Kp = 0.9, Ki = 9821.2 and Kd=5.4. Table 4.1 shows the optimal parameters of PID controllers used in bidirectional DC-DC converter control as well as buck-converter control.

Table 4.1: Optimal parameters of PID controllers

Bidirectional Converter			Buck-Converter
Inner Current Controller		Outer Voltage Controller	Voltage Controller
Kp	0.7	0.0242	0.9
Ki	100	99.9582	9821.2
Kd	-	-	5.4

CHAPTER FIVE

5. RESULT AND DISCUSSION

In this chapter, the validity of the thesis work is tested through simulation in MATLAB software and analyzed. The proposed maximum power point tracking (MPPT) technique is compared to conventional MPPT techniques under various solar radiation and temperature. The performance of the suggested MPPT technique is evaluated for different levels of solar intensity and cell temperature. In addition, the charging state control of the battery is assessed. Finally, the output voltage response is shown both when power is available from the photovoltaic (PV) system due to sunlight, and when no power is produced by the PV system in the absence of sunlight. The simulation results illustrate the successfulness of the suggested MPPT control strategy and battery management approach to keep the voltage at constant for the load over varying operating conditions. Figure 5.1 shows the general MATLAB Simulink model of the system.

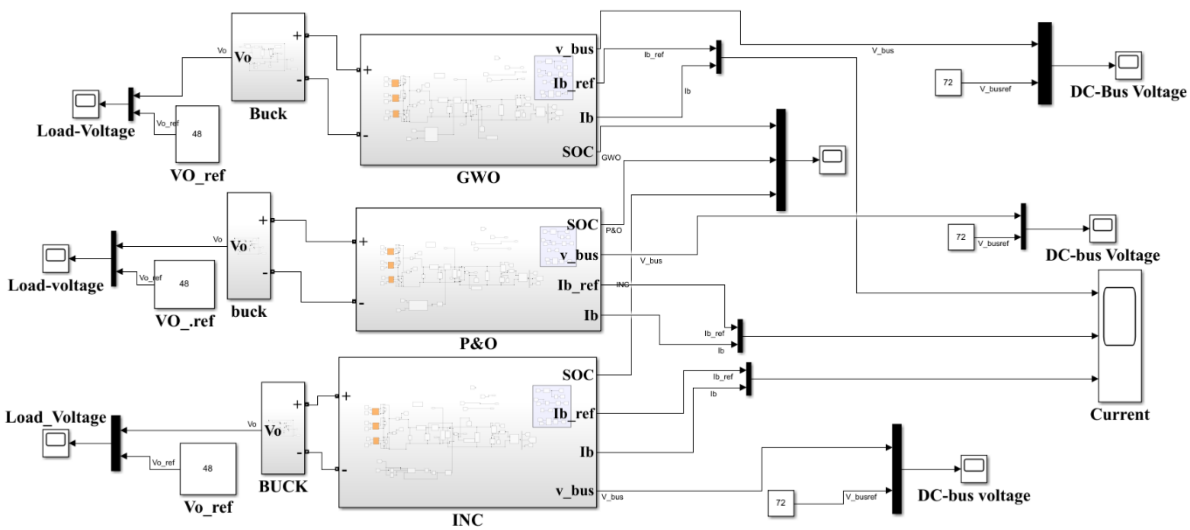

Figure 5.1: General MATLAB/Simulink model

5.1 Simulation Result of MPPT

The proposed grey wolf optimizer (GWO) algorithm was tested under various partial shading conditions in order to evaluate its performance. A photovoltaic (PV) module single diode model was simulated at nominal operating conditions for a single PV module with the following parameters: maximum power (Pmax) of 200.143 W, open circuit voltage (Voc) of 32.9 V, short circuit current (Isc) of 8.21 A, voltage at maximum power (Vmp) of 26.3 V, and current at maximum power (Imp) of 7.61 A. Three modules connected in series were configured to generate a maximum power output of approximately 600W.

Equation 5.1 was used to calculate the efficiency parameter and assess the tracking efficiency of the different MPPT algorithms under evaluation. This involved measuring the ratio of average output power to the maximum available power from the PV array under varying conditions, including partial shading. The simulation results provide insights into the performance and effectiveness of the proposed GWO-approach of MPPT.

$$\eta_{\max} = \frac{P_m}{P_{\max}} \tag{5.1}$$

To evaluate the performance of the proposed grey wolf optimizer (GWO) approach, the photovoltaic (PV) system was subjected to three different shading patterns. Under each shading pattern, the GWO-MPPT method was compared against conventional perturbation and observe (P&O) and incremental conductance (INC) algorithms in terms of output power, output voltage, and output current. The three shading patterns allowed for a comparative assessment of how effectively each MPPT technique could track the maximum power point and maximize the power output from the PV array when some modules in the string were partially shaded. This detailed evaluation under variable shading conditions provides insights into the relative tracking efficiencies and benefits of the GWO algorithm compared to traditional MPPT methods.

Pattern1: In Pattern 1, the GWO MPPT performance was tested under standard test conditions (STC) without shading. The environmental parameters were set to 1000 W/m^2 irradiance and 25°C for the three series-connected PV modules. The response of output power, voltage and current at these STC parameters was compared for GWO-algorithm versus conventional P&O and INC MPPT techniques.

Figure 5.2 shows the P-V characteristics at STC, while Figures 5.3 - 5.5 display the tracking performance comparison of PV output power, voltage and current for the GWO, P&O and INC algorithms. Equation (5.1) was utilized to calculate the tracking efficiency, which is important to validate the maximum output power extraction efficiency of the different MPPT techniques.

Under the non-shaded STC scenario, Figure 5.2 illustrates the peak power point. Figures 5.3-5.5 then allow comparison of how closely each MPPT method could track this maximum power level over time. This evaluation under ideal STC conditions without shading effects served as a benchmark for assessing the GWO algorithm's ability to perform effective MPPT.

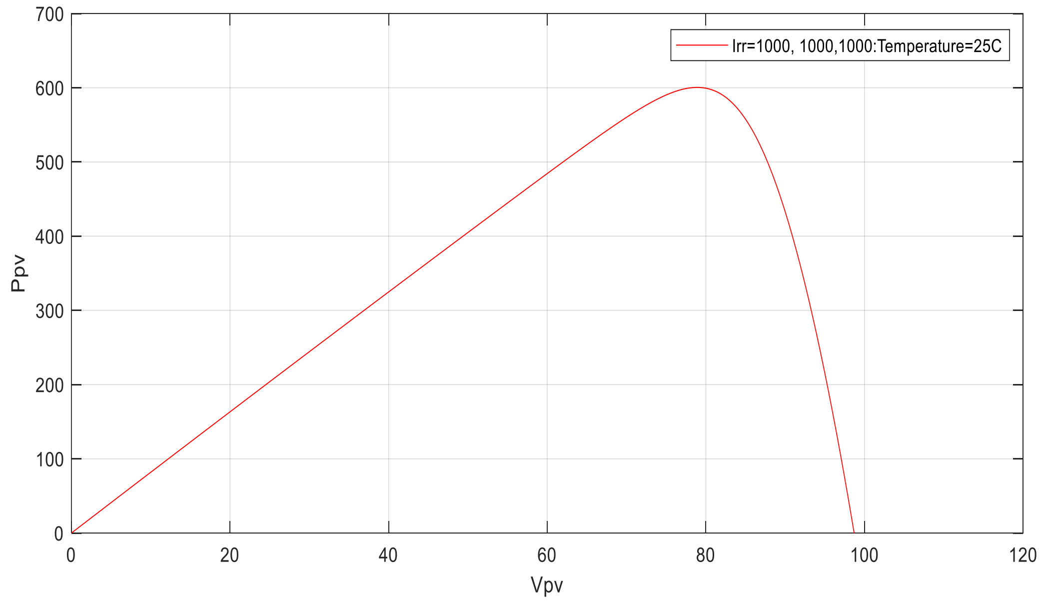

Figure 5.2: P-V Characteristics at STC

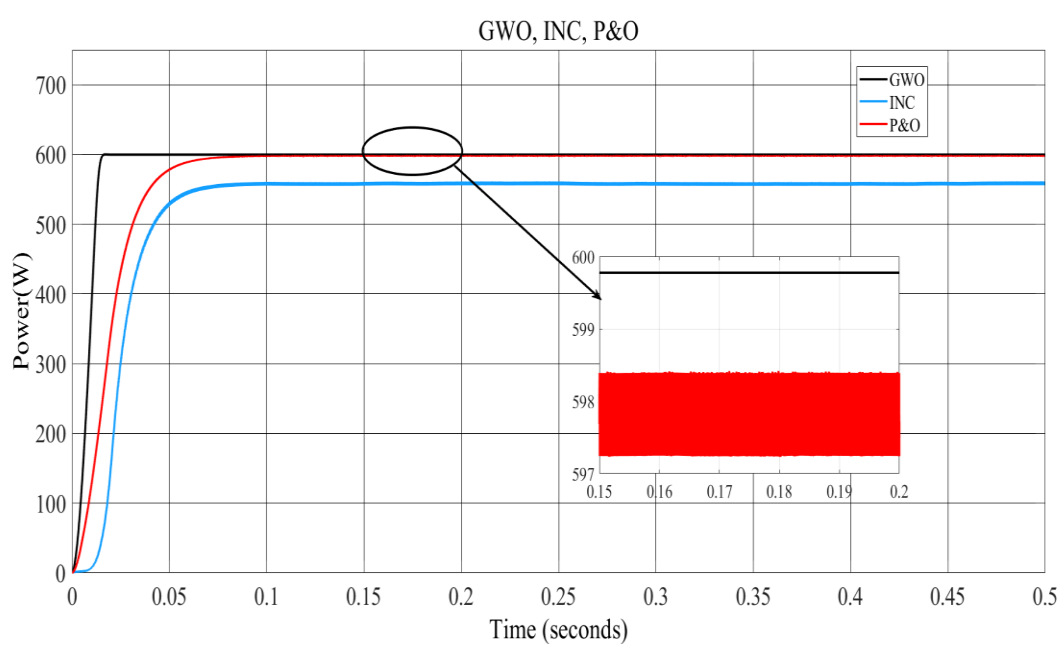

Figure 5.3: Output power response under constant irradiation and temerature (1000 W/m2 ,25°C)

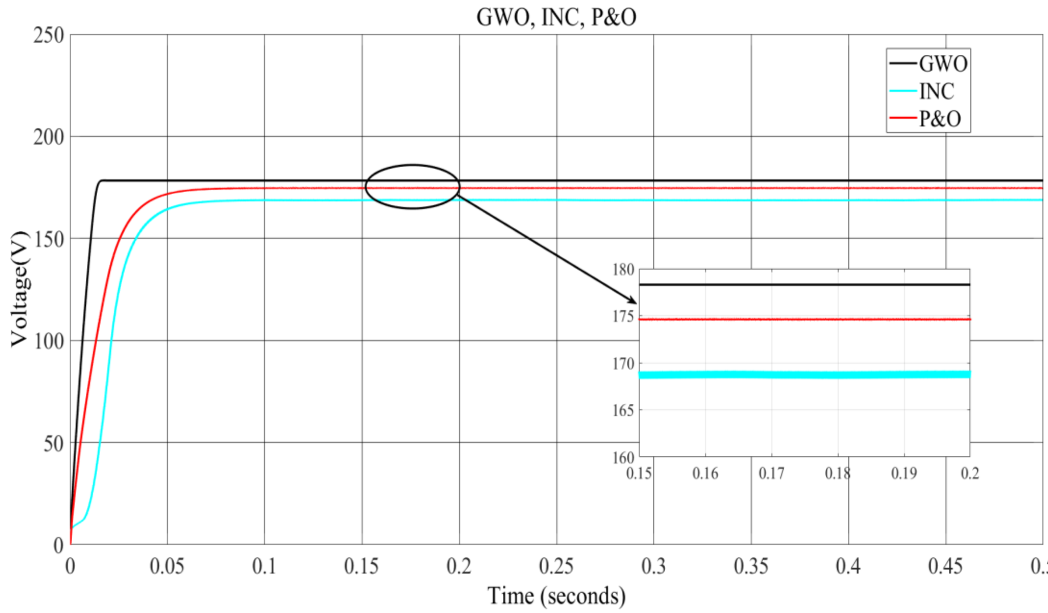

Figure 5.4: Output voltage response under constant irradiation and temerature (1000 W/m^2 ,25°C)

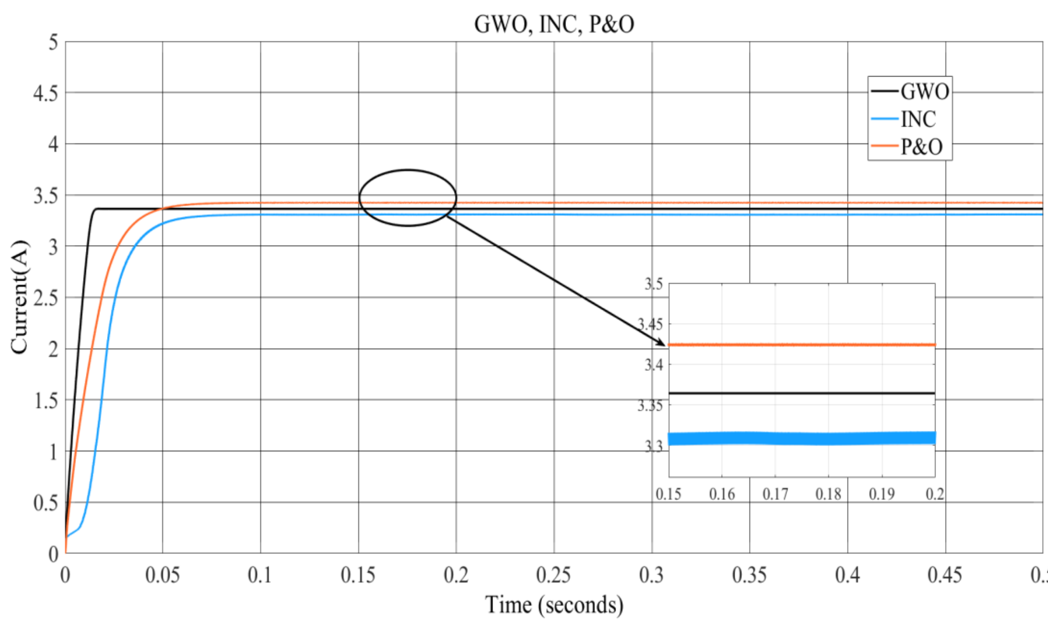

Figure 5.5: Output current response under constant irradiation and temerature (1000 W/m^2 ,25°C)

Numerical analysis was conducted to compare the performance of the INC, P&O, and GWO MPPT algorithms under constant irradiation and temperature conditions. Table 5.1 presents the numerical results from the optimization algorithms. The proposed GWO-approach controller performed superiorly compared to the other techniques. As shown, the GWO-approach achieved an efficiency of 99.98%. This was the highest efficiency observed amongst the different MPPT approaches. In terms of maximum output power (Pm), the GWO-approach produced the greatest value of 599.92 W. In contrast, the INC method generated the lowest Pm of 558.6 W.

These findings from Table 5.1 indicate the GWO-approach controller delivered optimized performance for maximizing the power extracted from the PV system under steady-state weather conditions. The proposed algorithm provided improved tracking efficiency and a higher power output level relative to conventional P&O and INC MPPT techniques under the same insolation and temperature parameters.

Table 5.1: Comparison of MPPT algorithms in pattern 1

MPPT method	G=1000W/m^2 and T=25°C		
	Power Oscillation	$P_{average}$	Efficiency (%)
GWO	599.83-600	599.92	99.98
INC	556.1-561.1	558.6	93.1
P&O	597.3-598.4	597.85	99.64

Pattern 2: In this scenario, the MPPT techniques were evaluated under partial shading conditions with the temperature kept constant at 25°C. Shading was applied such that the three PV modules received three different irradiance levels: 1000, 900, and 700 W/m^2. Under this non-uniform irradiance profile, there were two local maxima points and one global maximum power point. Figure 5.6 shows the P-V characteristic in this partial shading scenario. As shown on the curve, the global maximum power was 465.8908W.

The time response of output power, voltage and current was then compared for each MPPT technique (INC, P&O and GWO) and plotted in Figures 5.7 through 5.9. This provided insights into how effectively each algorithm could track the true maximum power point under uneven shading across the PV string, a more challenging scenario than uniform irradiance. It evaluated their ability to overcome convergence to local optima and instead lock onto the highest possible output from the non-uniform array.

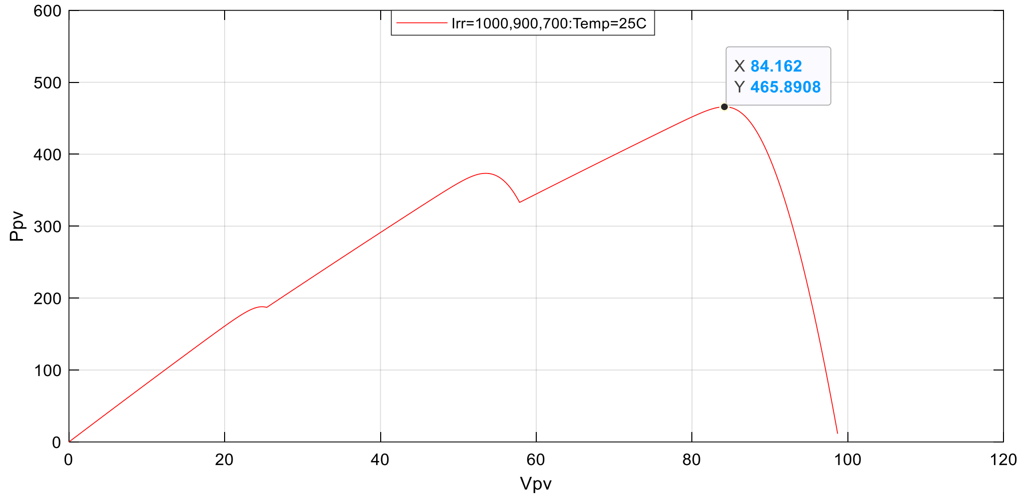

Figure 5.6: P-V Characteristic under pattern 2

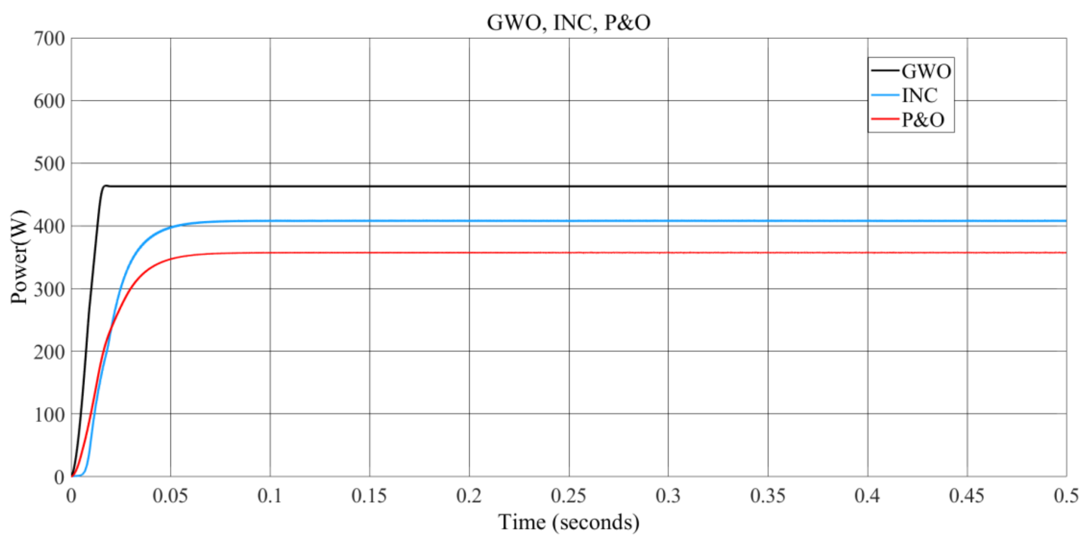

Figure 5.7: Output power for pattern 2

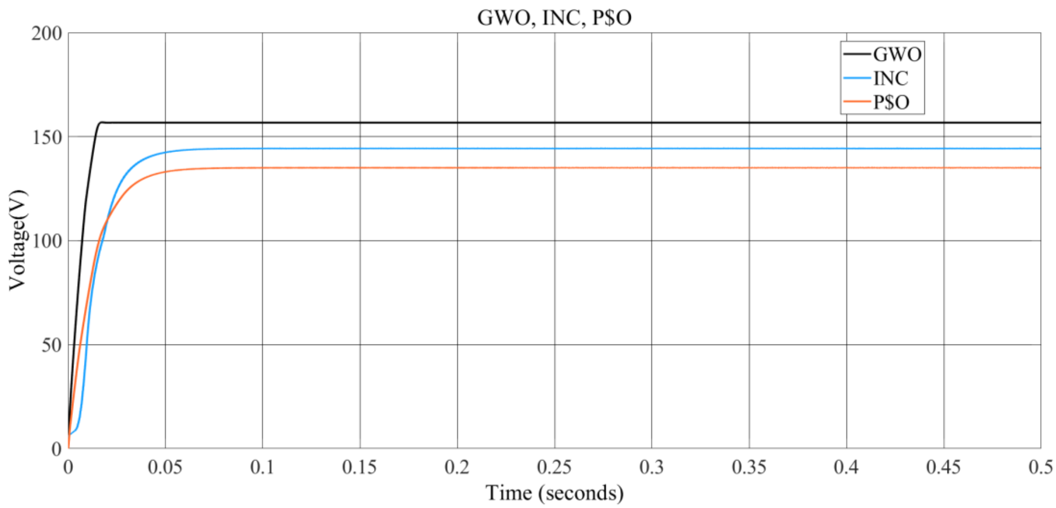

Figure 5.8: Output voltage for pattern 2

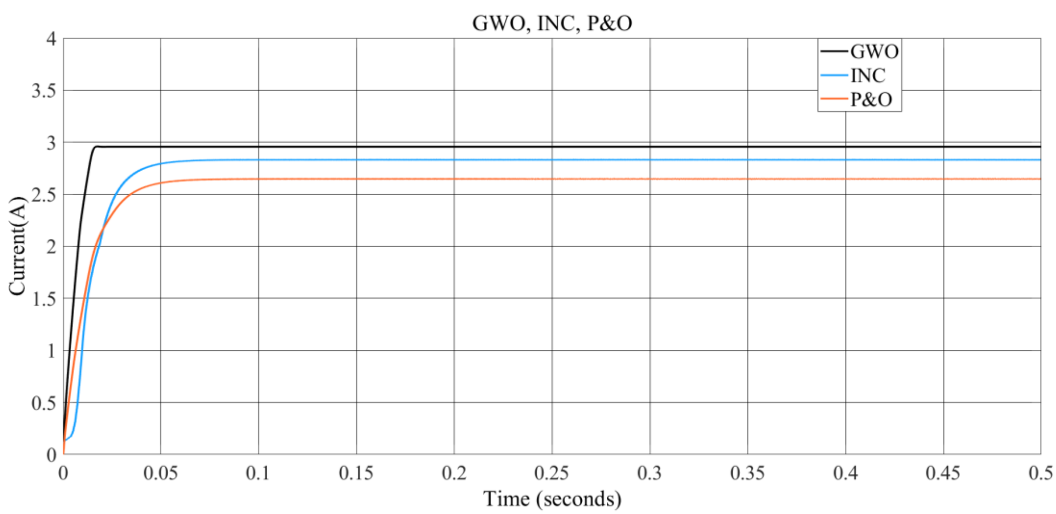

Figure 5.9: Output current for pattern 2

The numerical performance comparison of each algorithm is shown in Table 4. Here, the peak power tracking efficiency of each method is evaluated. The simulation results showed that the GWO approach achieved an efficiency of 99.83% by tracking 465.095W of power, which was very close to the absolute maximum achievable power of 465.8908W. In comparison, the INC method resulted in an efficiency of 87.63% and the P&O technique achieved 76.61% efficiency. This indicates that under non-uniform irradiance conditions, the GWO algorithm performed significantly better than the conventional INC and P&O MPPTs in terms of efficiency and its ability to lock onto the true global maximum power operating point of the PV array. The GWO-based approach more successfully overcame the trap of local optima to extract almost the full maximum deliverable output from the partially shaded panels. This demonstrates the advantages of the GWO technique for improved MPPT under shading scenarios.

Table 5.2: Comparison of MPP algorithms in pattern 2

MPPT method	G=1000, 900,700 W/m^2 and T=25°C		
	Power Oscillation	$P_{average}$	Efficiency (%)
GWO	464.9-465.29	465.095	99.83
INC	406.7-409.8	408.25	87.63
P&O	356-357.8	356.9	76.61

Pattern 3: Pattern 3 introduced variation in both irradiance and temperature to evaluate MPPT performance under more complex environmental conditions. The modules received irradiances of 1000, 400, and 600 W/m^2 and temperatures of 20, 18, and 19°C respectively for each module. GWO-approach is efficient by 99.8% and P&O and INC are 62.51% and 64% respectively. As depicted in Figure 5.10, there were two local maxima points and one global maximum under this pattern of non-uniform insolation and temperature. The output power, voltage and current tracking for each MPPT technique is shown in Figures 5.11- 5.13 respectively.

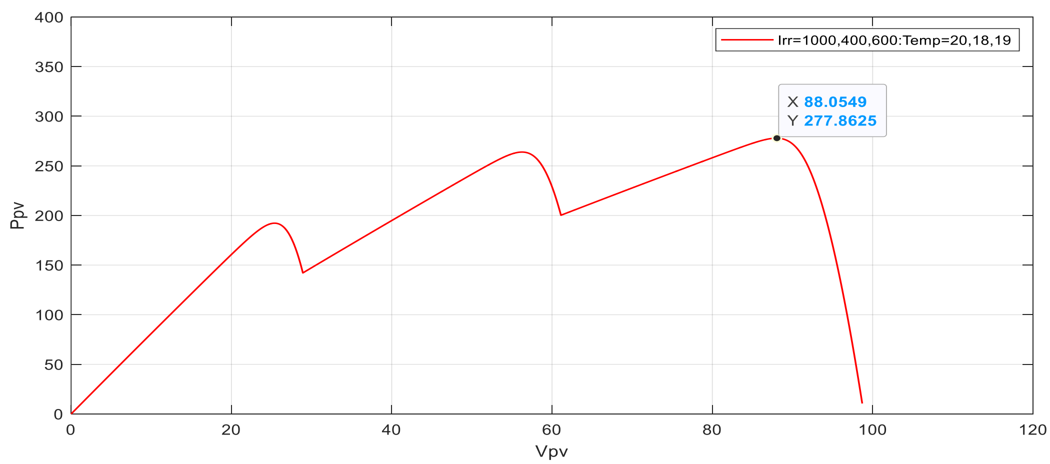

Figure 5.10: P-V characteristic under pattern 3

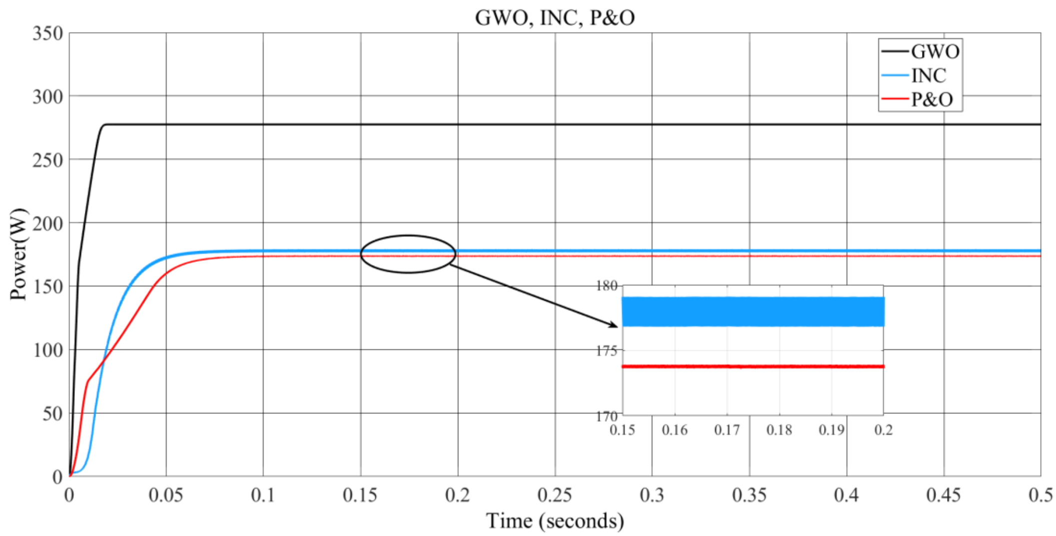

Figure 5.11: Output power response under pattern 3

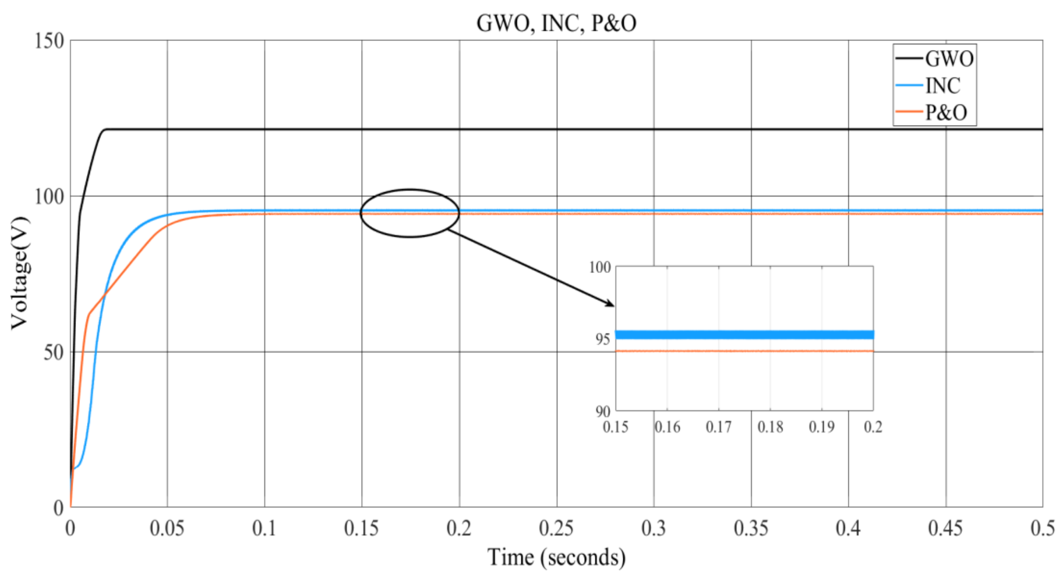

Figure 5.12: Output voltage response under pattern 3

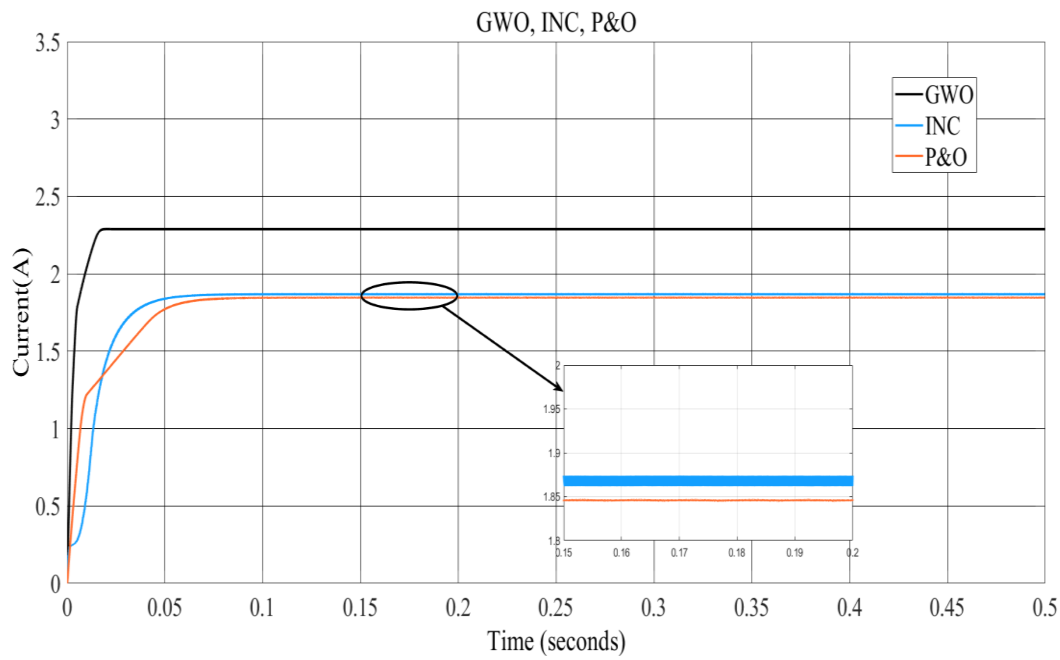

Figure 5.13: Output current response under pattern 3

Table 5.3: Comparison of MPP algorithms in pattern 3

MPPT method	G=1000, 400,600 W/m^2 and T=20, 18,19 °C		
	Power Oscillation	$P_{average}$	Efficiency (%)
GWO	277.6-277.02	277.31	99.8
INC	176.7-178.9	177.8	64
P&O	173.5-173.9	173.7	62.51

The response of each algorithm demonstrated that the GWO algorithm could effectively track the global peak power point, while the conventional INC and P&O MPPTs failed to do so under the partial shading scenario. In Maximum Power Point Tracking (MPPT) algorithms, the oscillation around the Maximum Power Point (MPP) is a common characteristic, especially for traditional algorithms like Perturb and Observe (P&O) and Incremental Conductance (INC). These oscillations occur due to the way these algorithms' function and their inherent design. P&O works by periodically perturbing (adjusting) the operating voltage of the PV system and observing the change in power output. When the system is at the MPP, any perturbation will cause a change in power that indicates moving away from the MPP. The algorithm then reverses the perturbation direction. This leads to a continuous back-and-forth adjustment, causing the system to oscillate around the MPP rather than settling precisely at it.

INC calculates the incremental changes in voltage and current to determine the direction in which the MPP lies. Similar to P&O, INC can also result in oscillations due to the discrete nature of its adjustments. The algorithm continuously adjusts the operating point based on the calculated slope of the power curve, which can cause oscillations around the MPP. GWO performs a global search for the MPP, considering multiple candidate solutions simultaneously. This helps in better convergence to the optimal point without frequent oscillations. The algorithm dynamically adjusts the position of candidates based on the best solutions found, leading to a smoother and more stable convergence.

5.2 Simulation Result for Voltage Control

5.2.1 Simulation Result for DC-bus Voltage Control

The battery acts as a buffer, balancing power between the solar panels (PV array) and load. Key parameters of battery and the bidirectional converter are presented in Table 6. The controller directs the bidirectional converter to charge/discharge the battery.

Table 5.4: Specification of battery and bidirectional converter

Bidirectional DC-DC converter specifications		Battery specifications	
Parameters	Magnitude	Parameters	Magnitude
C_b	0.001mF	V_{nom}	60V
L_b	0.576mH	Ah capacity	120
C_{dc}	0.4676mF	Initial SOC	50
f_{sw}	20khz		

The goal is to keep the load voltage V_{dc} at 48 volts in the presence of PV power disruptions brought on by variations in solar radiations and temperature. To achieve constant 48V supply for the load demand controlling the battery's charge and discharge is essential. Since an output voltage of PV is always varying it causes problem to directly connect it to the load. Hence, we need a DC-bus of voltage more than battery's voltage to control the battery's charge state. Accordingly, a DC-bus of 72V is chosen to be taken as DC-bus voltage, from which the load is supplied through buck converter. Therefore, control action is taken on bidirectional converter to keep the 72V DC-bus voltage constant when there is enough amount of power from PV system. The battery was designed to operate in two modes: charge and discharge, in accordance with the PV system's power availability. To assess the controller's performance for DC-bus voltage control the system was tested at STC of PV system.

Case one: Case one analyzed the 6 kW PV system at standard test conditions of irradiance and temperature to power the proposed load (MSAN) load. In this scenario, the system was capable of keeping the 72V DC bus voltage for all three MPPT algorithms (GWO, P&O, INC). However, Figures 5.14, 5.15 and 5.16 reveal that while all algorithms could regulate the DC link voltage, the P&O and INC techniques exhibited significant oscillation when tracking the reference value. In comparison, the GWO algorithm maintained the DC bus voltage with minimal oscillatory behavior.

This indicates that under uniform irradiance and cell temperature, the battery controller was effective at integrating the PV power output. But the GWO approach facilitated more stable control with reduced fluctuations in contrast to traditional P&O and INC. The results from Case one highlight that in an ideal scenario without shading or mismatches, the GWO approach MPPT algorithm delivered smoother DC bus voltage tracking through improved peak power harvesting from the PV array working with the battery control scheme.

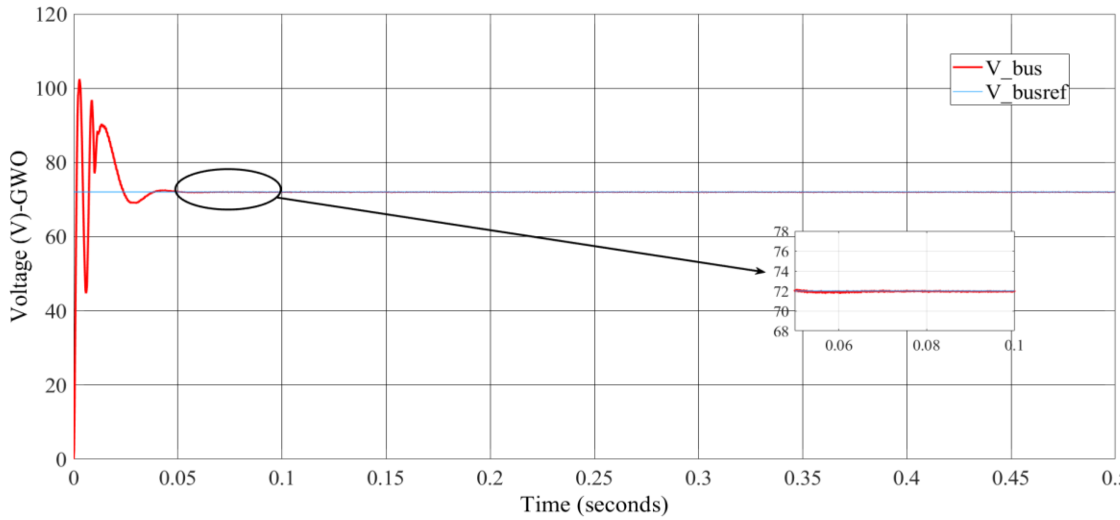

Figure 5.14: DC-bus voltage response with GWO-algorithm

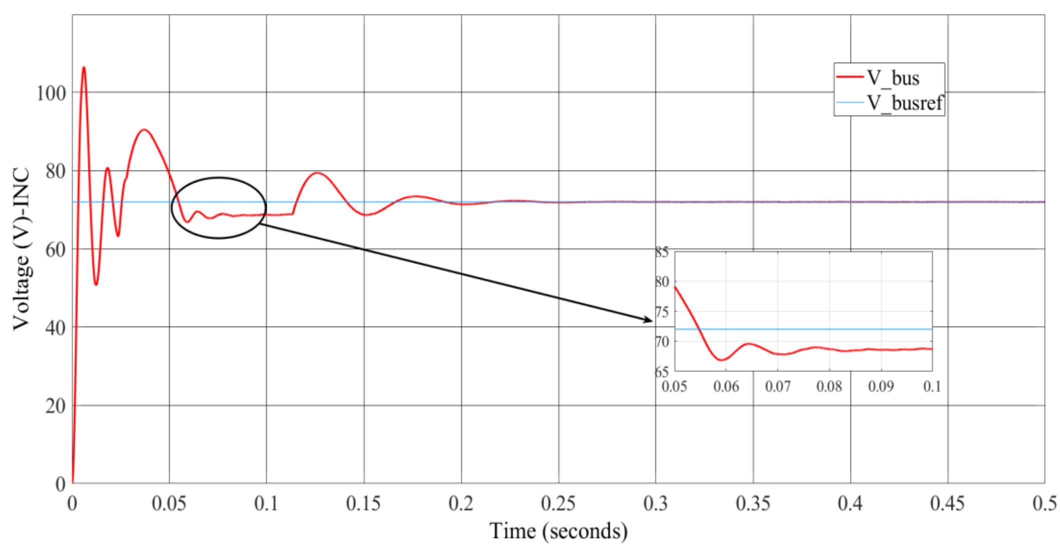

Figure 5.15: DC-bus voltage time response using INC algorithm

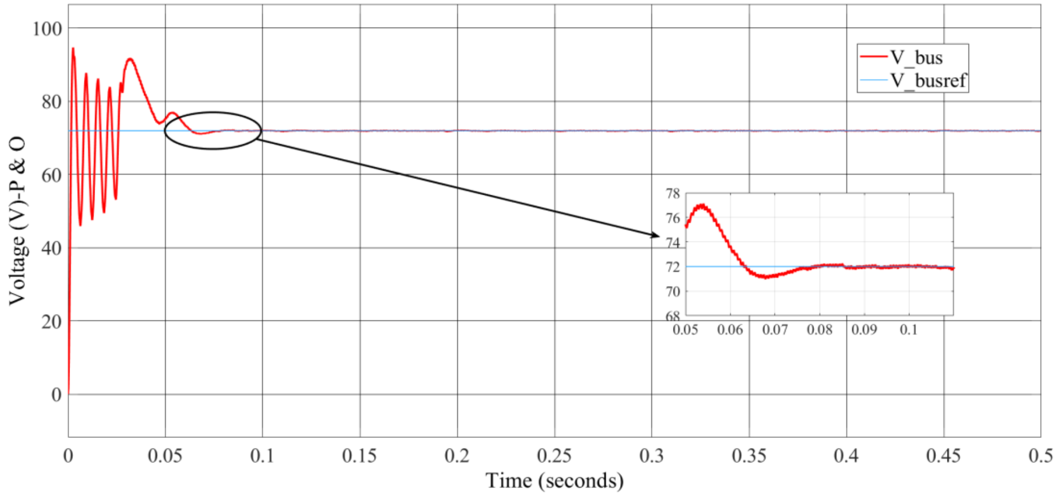

Figure 5.16: DC-bus voltage time response using P&O algorithm

The storage battery's mode of operation depends on voltage output obtained from the PV through the MPPT algorithm. A DC-bus voltage of 72V is maintained to determine whether the battery charges or discharges. If the PV output voltage is above 72V, the battery charges; if below, it discharges to provide a steady voltage to the load. This is achieved by a bidirectional DC-DC converter.

In Case 1, the storage battery operates in buck mode, charging from the PV power supply while maintaining the DC-bus voltage at 72V. A dual loop PI controller regulates the DC-DC converter to control this voltage. As shown, the output voltages obtained can maintain the required DC-bus level. Figure 5.17 also shows the battery charging state.

However, the output voltage tracking performance differs between algorithms. As seen, GWO-approach provides a much smoother time response compared to P&O and INC, which exhibit more oscillation about the peak power. Zooming out on 0.05-0.1 seconds reveals greater oscillation for P&O and INC around the reference value. To control the DC-bus voltage, a Proportional-Integral (PI) controller was used. However, when using a PI controller, the system's response initially exhibits a significant overshoot. While adding a Derivative (D) parameter to the controller can mitigate this overshoot, it introduces a trade-off by increasing the steady-state error. Given this trade-off, a PI controller is preferred to manage the DC-bus voltage, despite the initial overshoot, to maintain a better steady-state performance. The performance of the MPPT algorithms can also be seen from battery charging state. The battery also charges faster with GWO-algorithm. The GWO-approach tracks more power, this resulted in fast charging of the battery compared to the other algorithms.

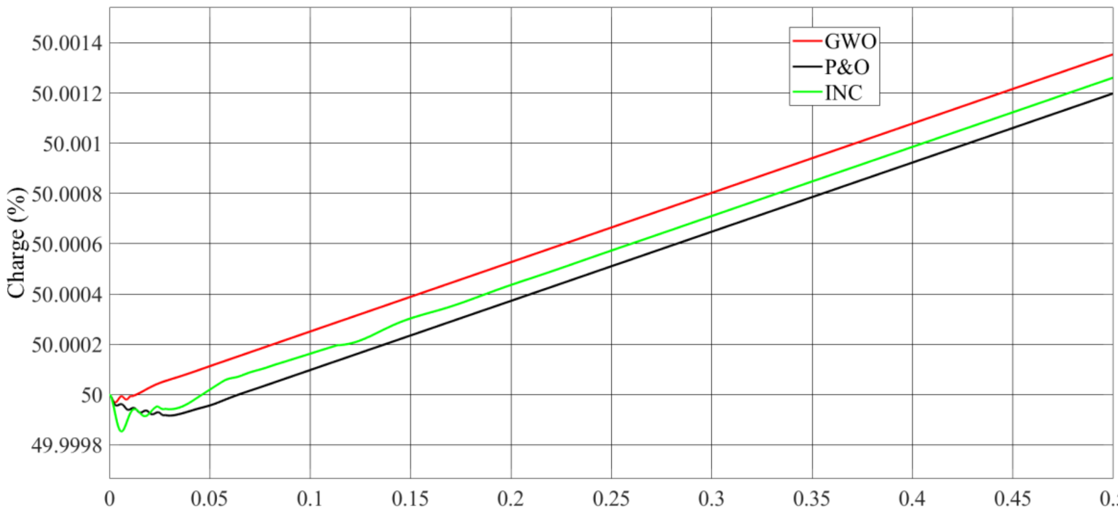

Figure 5.17: Battery state of charge

The bidirectional converter's inner current control loop determines battery current direction, which consequently defines whether it charges or discharges. This current direction regulation is performed via inner-loop current control. As a result, negative current values indicate the battery is charging, while positive currents mean it is discharging. Figure 5.18 below presents the simulation results for this inner current control in Case 1. The reference current for the inner loop is generated from the outer voltage controller loop. As can be seen, the currents remain negative, confirming the battery is charging under these conditions.

This valuable insight provided by the inner current control simulation results serves to validate the earlier findings. Namely, that with GWO-approach combined with the DC-DC converter's dual loop control scheme providing optimal and stable PV output voltage, the storage battery successfully charges.

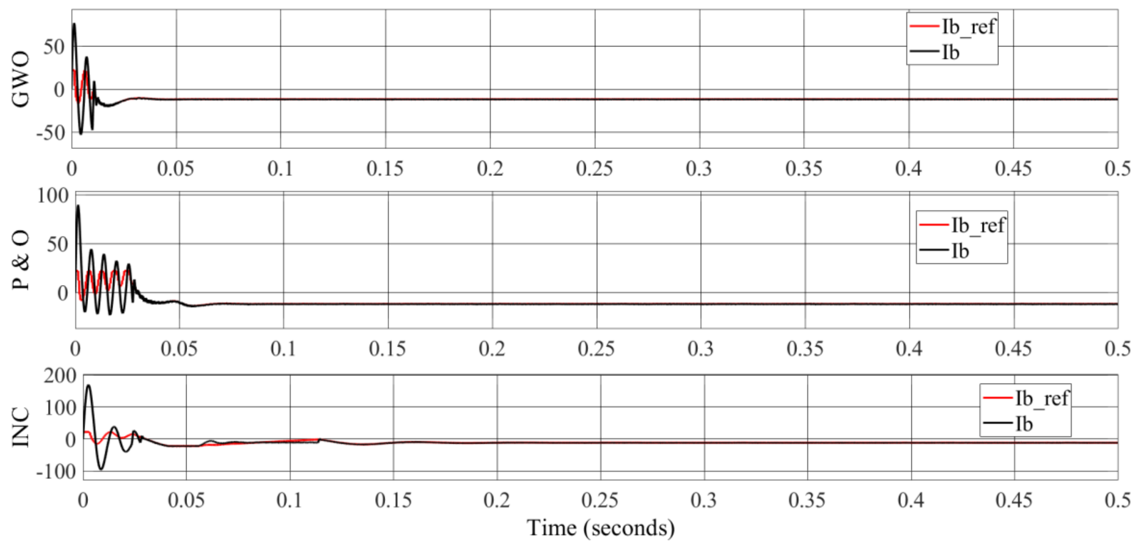

Figure 5.18: Inner loop control currents

5.2.2 Simulation Result for Load Voltage Control

The load has a connection to the DC-bus via a buck converter, as previously described. The required output voltage for the load from the buck converter is 48V, which must be supplied continuously from either the PV system or storage battery. Unlike the control of the DC-bus voltage, where some degree of overshoot can be tolerated, the system in question requires minimal to zero overshoot to prevent damage to the equipment. Therefore, the controller used in this scenario must incorporate a Derivative (D) parameter in addition to the existing Proportional-Integral (PI) controller. This enhancement results in a Proportional-Integral-Derivative (PID) controller, which effectively reduces overshoot. In the case of DC-bus voltage control, the PI controller proved advantageous by minimizing the steady-state error, thereby providing a stable DC-bus voltage response. This stability in the DC-bus voltage has facilitated the use of a PID controller for managing the voltage output of a buck converter connected to the DC-bus. The inclusion of the D parameter in the PID controller ensures that the output voltage of the buck converter is tightly regulated, with minimal overshoot, thereby protecting the connected equipment from potential damage. The results demonstrate that the optimal PID controller applied to the buck converter successfully regulates the output voltage at 48V. However, when considering the combined system with different MPPT algorithms, there is still some oscillation around the reference for P&O and INC compared to the GWO-MPPT approach. Figures 5.19, 5.20 and 5.21 present the simulation output voltages for Case 1 using the various MPPT techniques. Additionally, Figure 5.22 shows the unit step response of the buck converter with optimal PID control. The controller performance parameters indicate 0.78s rise time and settling time of 1.98 seconds. In summary, the optimal PID-controlled buck converter effectively maintained the required 48V load voltage. Nevertheless, the GWO-approach algorithm again provided superior stability with less fluctuation than P&O and INC under these test conditions.

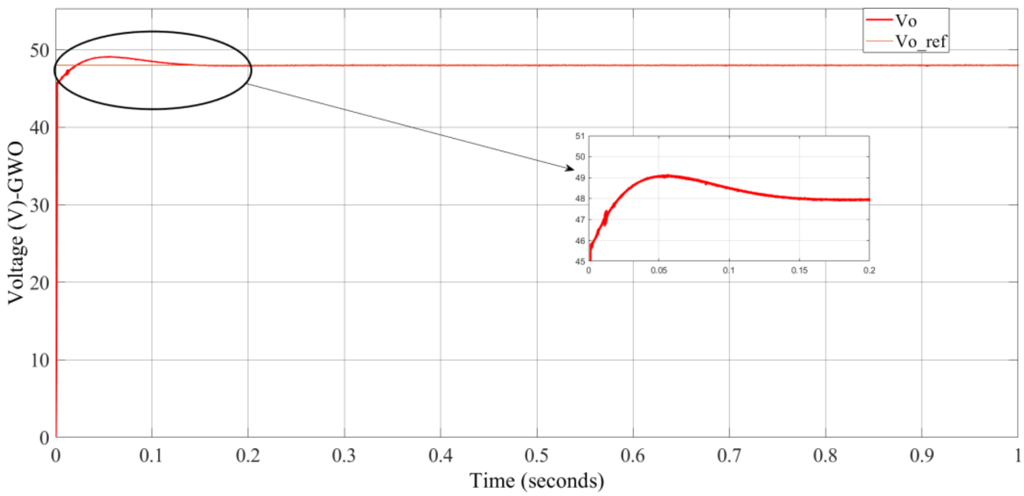

Figure 5.19: Response of output voltage using GWO-Algorithm

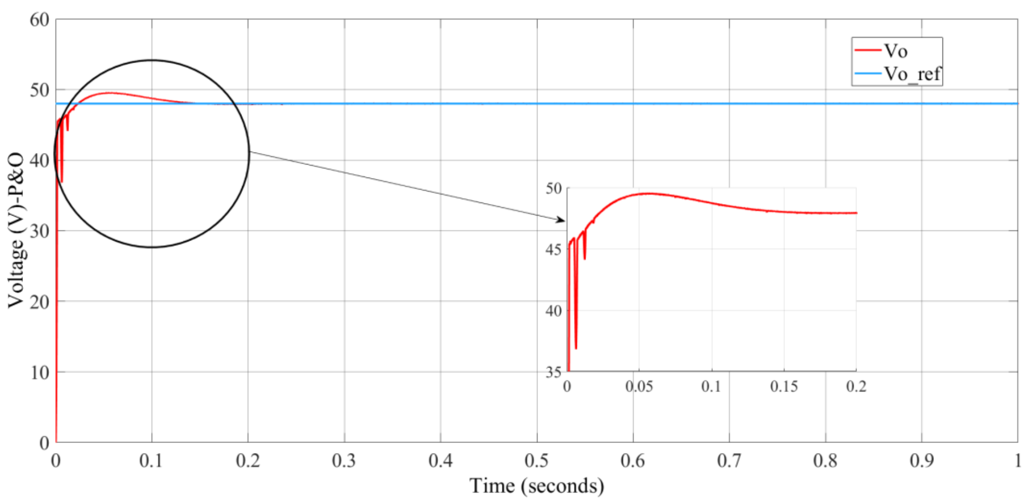

Figure 5.20: Response of output voltage using P&O-MPPT

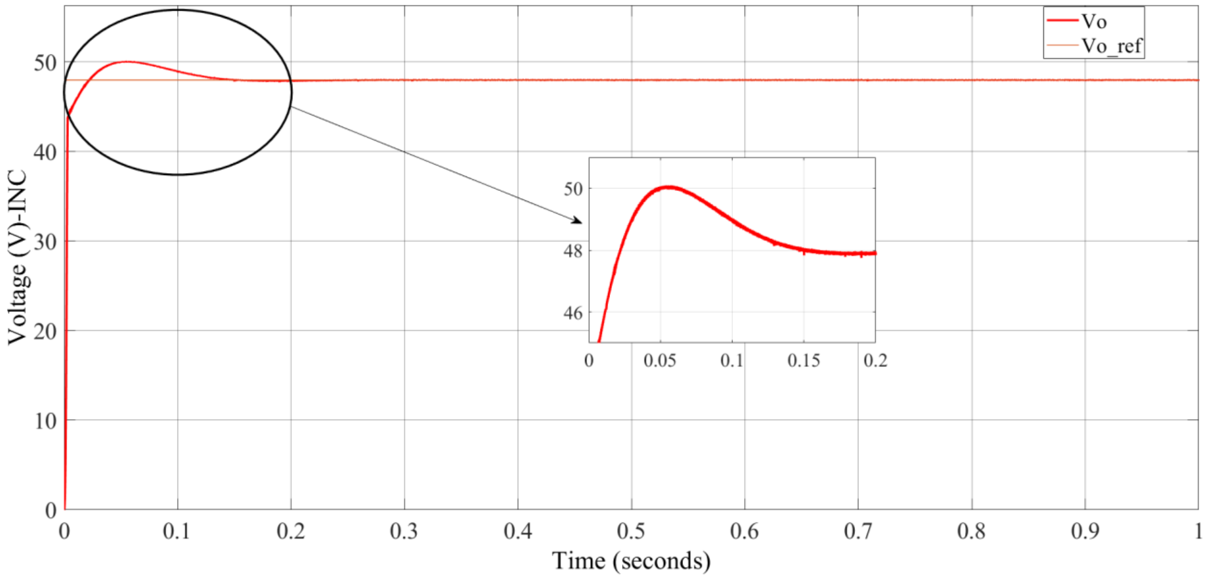

Figure 5.21: Output voltage response with INC-MPPT

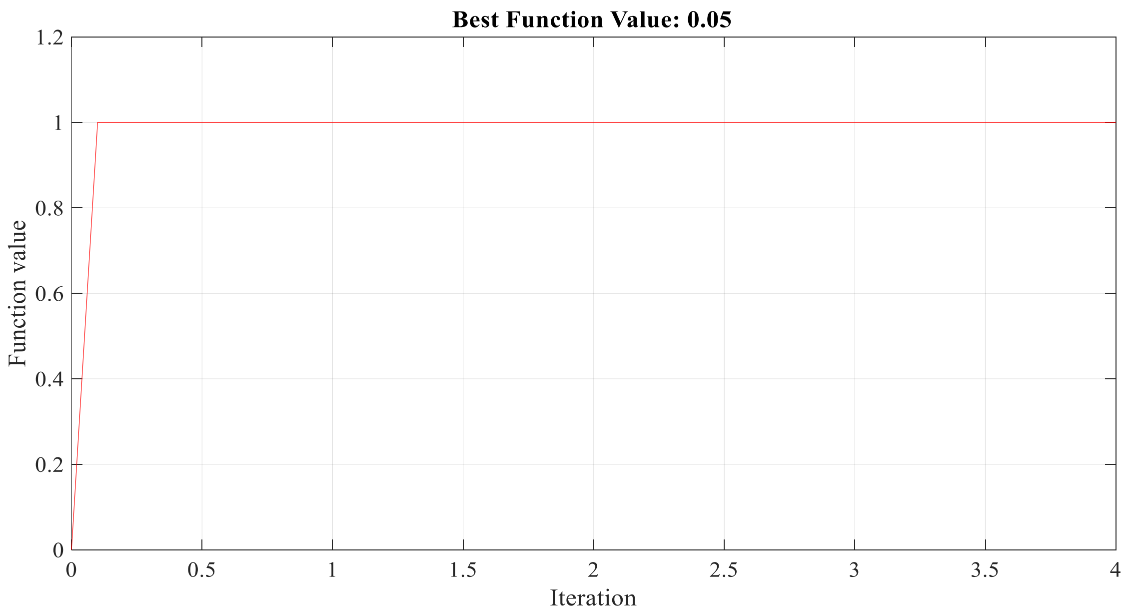

Figure 5.22: Step response of buck-converter

Case Two: There is no power supply from PV panel. During night time there will be no solar radiation to generate power for the load. As already mentioned in the document the load under consideration (MSAN) has to be active 24hrs/day to satisfy users needs. Therefore, during night time the storage battery will feed the load.

At this time the bi-directional converter is regulated by optimal PI controller to discharge the battery as per the requirement of the load. It operetes in boost-mode to discharge the storage battery. The buck converter then takes the battery voltage to reduce it to 48V. Figure 5.23 illustrates the performance of the buck converter to produce output voltage for the load.

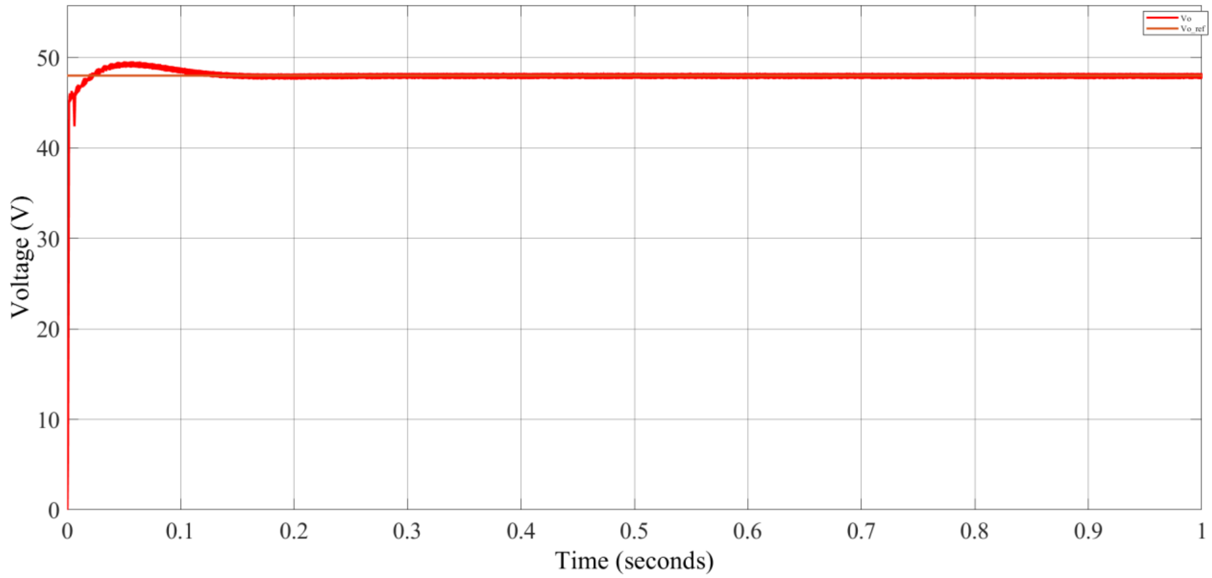

Figure 5.23: Buck-converter voltage output

As shown in Figure 5.24 the discharging of storage battery during the absence of PV panel is happening.

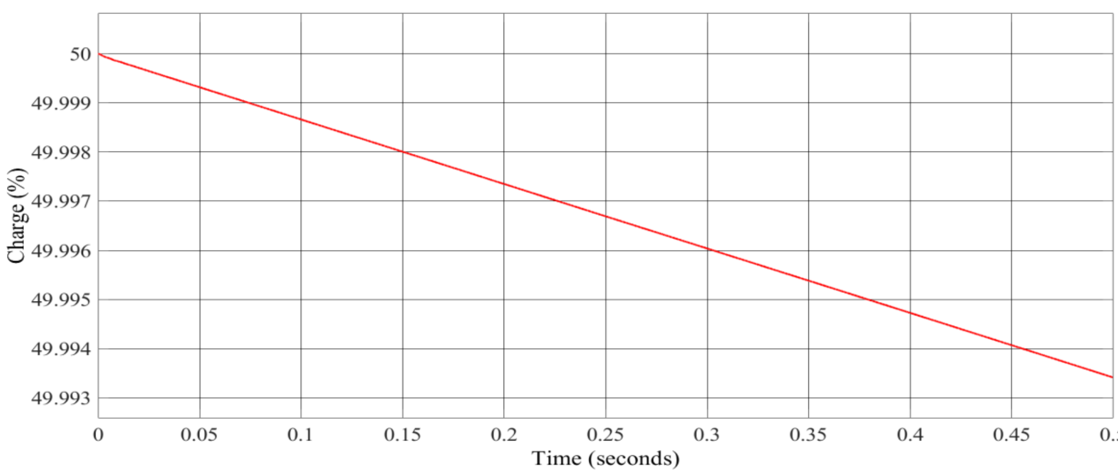

Figure 5.24: SOC during night time

CHAPTER SIX

6. CONCLUSION AND RECOMMENDATION

6.1 Conclusion

In this thesis a new grey wolf optimization based MPPT to track peak power of PV system, an optimal dual loop PI controller for bidirectional converter to control charge/discharge operation of battery and designed an optimal PID cotroller for voltage output control of buck-converter were discussed. For monitoring the PV system's peak power, grey wolf optimization algorithm is used. The algorithm takes PV volage and current as input and calculates the power. Depending on the power generated it calculates duty cycle to control the switching of boost converter. The PV is linked to DC-bus of 72V via boost converter. To store the energy generated from PV, storage battery is used. The charging and discharging of the battery takes place by non-isolated bidirectional converter. The converter is controlled by double loop PI controller. The exterior loop regulates DC-bus voltage, and the inner loop regulates battery/inductor current. Based on the PV system's power output the state of charge of the battery is decided. At load terminal multi-service access node, which consume a constant voltage of 48V, is connected to DC-bus via a buck-converter. The optimimized parameters of the controllers are calculated by PSO-algorithm. Two traditional MPPT algorithms are used to compare the GWO-MPPT algorithm's performance namely, P&O and INC and GWO-algorithm was found to be of a high efficiency under shading problem. The output voltage of buck-converter showed that each MPPT technique has significant impact on stablity of the voltage required by the load.

6.2 Recommendation

This study suggests that future researchers to work on hardware implementation of this work, consider the effect of temperature to design MPPT technique. To add dummy load to dump available extra-power when battery is fully charged.

REFERENCES

Aiguo Sun, W. Z., Xiaohong Lin, & Jingxin Li. (2014). Modeling and stability Analysis of High Voltage ratio Bidirectional DC/DC converter applied to electric vehicle. *IEEE, 1*(2014), 1–58.

Andres Ramos-Paja, C., David Bastidas-Rodriguez, J., Julian Saavedra-Montes, A., & Design and, A. (2021). Design and Control of a Battery Charger/Discharger Based on the Flyback Topology. *Discharger Based on the Flyback Topology. Appl. Sci, 2021*, 10506. https://doi.org/10.3390/app

Belhachat, F., & Larbes, C. (2017). Global maximum power point tracking based on ANFIS approach for PV array configurations under partial shading conditions. In *Renewable and Sustainable Energy Reviews* (Vol. 77, pp. 875–889). Elsevier Ltd. https://doi.org/10.1016/j.rser.2017.02.056

Betha Karthik Sri Vastav, Savita Nema, Pankaj Swarnkar, & https://www.researchgate.net/scientific-contributions/Doppllapudi-Rajesh-2121630418?_tp=eyJjb250ZXh0Ijp7ImZpcnN0UGFnZSI6InB1YmxpY2F0aW9uIiwicGFnZSI6InB1YmxpY2F0aW9uIn19. (2017). Automatic Solar Tracking System using DELTA PLC. *IEEE*, *1*(1), 1–90.

Burcu Gundogdu and Daniel Thomas Gladwin. (2018). Bi-directional Power Control of Grid-tied Battery Energy Storage System Operating in Frequency Regulation. *IEEE*, *1*(2018), 1–90.

Chaieb & Sakly. (2015). Comparison between P&O and P.S.O Methods Based MPPT Algorithm for Photovoltaic Systems. *IEEE*, *1*(1), 1–90.

Chao-Ming Huang, & Shin-Ju Chen. (2020). Parameter Estimation of a Single-Diode PV Model Using a Hybrid Charged System Search Algorithm. *IEEE*, *1*(30,July,2020), 1–80.

Chen, Z., Wu, L., Lin, P., Wu, Y., & Cheng, S. (2016). Parameters identification of photovoltaic models using hybrid adaptive Nelder-Mead simplex algorithm based on eagle strategy. *Applied Energy*, *182*, 47–57. https://doi.org/10.1016/j.apenergy.2016.08.083

Chinna Kullay Reddy, D., Satyanarayana, S., & Ganesh, V. (2018). Design of hybrid solar wind energy system in a microgrid with MPPT techniques. *International Journal of Electrical and Computer Engineering*, *8*(2), 730–740. https://doi.org/10.11591/ijece.v8i2.pp730-740

Curevac, S., Kavaz, A., Hodžić, S., Hubana, T., Ćurevac, S., Đozić, N., Merzić, H., Tanković, H., Dervišević, K., Alihodžić, E., Sikira, E., Rahić, D., Kavazović, N., Tanković, F., & Šestan, B. (2014). *Solar Tree Project*. https://www.researchgate.net/publication/322628682

Dehghani, M., Taghipour, M., Gharehpetian, G. B., & Abedi, M. (2021). Optimized Fuzzy Controller for MPPT of Grid-connected PV Systems in Rapidly Changing Atmospheric Conditions. *Journal of Modern Power Systems and Clean Energy*, *9*(2), 376–383. https://doi.org/10.35833/MPCE.2019.000086

Elkholy, A., & Abou El-Ela, A. A. (2019). Optimal parameters estimation and modelling of photovoltaic modules using analytical method. *Heliyon*, *5*(7). https://doi.org/10.1016/j.heliyon.2019.e02137

Evren Isen. (2021). Modeling and Simulation of DC-DC Converters. *IEEE, 1*(2021), 1–50.

Gomathi B, & Sivakami P. (2021). An Incremental Conductance Algorithm based Solar Maximum Power Point Tracking System. *IEEE, 1*(2021), 1–90.

Hamza Sahraoui, Said Drid, Larbi Chrifi-Alaoui, & Mohammed Hamzaoui. (2015). Voltage control of DC-DC Buck Converter using Second Order Sliding Mode Control. *Https://Ieeexplore.Ieee.Org/Xpl/Conhome/7194873/Proceeding*, *1*(2), 1–90.

Jayaprakash, S., & Ramakrishnan, V. (2015). Analysis of solar based closed loop DC-DC converter using PID and fuzzy logic control for separately excited motor drive. *Proceedings - NCET NRES EM 2014: 2nd IEEE National Conference on Emerging Trends in New and Renewable Energy Sources and Energy Management*, 118–122. https://doi.org/10.1109/NCETNRESEM.2014.7088751

Jie Mei, & James L.Kirtley. (2018). A Non-Cooperative Game Theory Based Controller Tuning Method for Microgrid DC-DC Converters. *IEEE*, *1*(2018), 1–78.

Jirada, G., Duy-Dinh, N., & Goro, F. (2018). Partial Shading and Global Maximum Power Point Detections Enhancing MPPT for Photovoltaic Systems Operated in Shading Condition. *Semantic Scholar*, *2018*, 10–60.

Kchaou, A., Naamane, A., Koubaa, Y., & M'Sirdi, N. K. (2017). Comparative study of different MPPT techniques for a stand-Alone PV system. *2016 17th International Conference on Sciences and Techniques of Automatic Control and Computer Engineering, STA 2016 - Proceedings*, 629–634. https://doi.org/10.1109/STA.2016.7952092

Khan, M. J., Mathew, L., Alotaibi, M. A., Malik, H., & Nassar, M. E. (2022). Fuzzy-Logic-Based Comparative Analysis of Different Maximum Power Point Tracking Controllers for Hybrid Renewal Energy Systems. *Mathematics*, *10*(3). https://doi.org/10.3390/math10030529

Kumar, S., Kumar, R., & Singh, N. (2017). Performance of closed loop SEPIC converter with DC-DC converter for solar energy system. *2017 4th International Conference on Power, Control and Embedded Systems, ICPCES 2017*, *2017-January*, 1–6. https://doi.org/10.1109/ICPCES.2017.8117668

Laxman, B., Annamraju, A., & Srikanth, N. V. (2021). A grey wolf optimized fuzzy logic based MPPT for shaded solar photovoltaic systems in microgrids. *International Journal of Hydrogen Energy*, *46*(18), 10653–10665. https://doi.org/10.1016/j.ijhydene.2020.12.158

L.H.P.N.Gunawardena, & D.R.Nayanasiri. (2019). Battery Charger Based on Bi-directional High Step-Up/Down DC-DC Converter. *IEEE*, *1*(1), 1–79.

Li, X., Hui, D., & Lai, X. (2013). Battery energy storage station (BESS)-based smoothing control of photovoltaic (PV) and wind power generation fluctuations. *IEEE Transactions on Sustainable Energy*, *4*(2), 464–473. https://doi.org/10.1109/TSTE.2013.2247428

Ling, R., Shu, Z., Hu, Q., & Song, Y. D. (2018). Second-Order Sliding-Mode Controlled Three-Level Buck DC-DC Converters. *IEEE Transactions on Industrial Electronics*, *65*(1), 898–906. https://doi.org/10.1109/TIE.2017.2750610

Louassaa, K., Chouder, A., & Rus-Casas, C. (2023). Robust Nonsingular Terminal Sliding Mode Control of a Buck Converter Feeding a Constant Power Load. *Electronics (Switzerland)*, *12*(3). https://doi.org/10.3390/electronics12030728

Malarvili, S. M., Mageshwari, S. M., & Vinothkumar. (2021). Artificial Intelligent Parameter based PSO for Maximum Power Point Tracking of PV Systems under PSC. *Proceeding - 2021 IEEE 17th International Colloquium on Signal Processing and Its Applications, CSPA 2021*, 86–91. https://doi.org/10.1109/CSPA52141.2021.9377286

Masood, B., Siddique, M. S., Asif, R. M., & Zia-Ul-Haq, M. (2015). Maximum power point tracking using hybrid perturb & observe and incremental conductance techniques. *2014 4th International Conference on Engineering Technology and Technopreneuship, ICE2T 2014*, *2014-August*, 354–359. https://doi.org/10.1109/ICE2T.2014.7006277

Mirza Fuad Adnan, Mohammad Abdul Moin Oninda, Mirza Muntasir Nishat, & Nafiul Islam. (2017). Design and Simulation of a DC - DC Boost Converter with PID Controller for Enhanced Performance. *Research Gate*, *6*(09, September-2017), 1–90.

Mirza Fuad Adnan, Mohammad Abdul Moin Oninda, & Nafiul Islam. (2017). Design and Simulation of a DC - DC Boost Converter with PID Controller for Enhanced Performance. *IEEE*, *6*(09, September-2017), 1–90.

Mohamed, S. A., & Abd El Sattar, M. (2019). A comparative study of P&O and INC maximum power point tracking techniques for grid-connected PV systems. *SN Applied Sciences*, *1*(2). https://doi.org/10.1007/s42452-018-0134-4

Nazeri, M. Z., Hanis, N., & Rahman, A. (2022). Maximum Power Point Tracking Using Perturb and Observe Technique. In *Journal of Engineering Technology* (Vol. 10, Issue 1).

Pal, R. S., & Mukherjee, V. (2020). Metaheuristic based comparative MPPT methods for photovoltaic technology under partial shading condition. *Energy*, *212*. https://doi.org/10.1016/j.energy.2020.118592

Park, H. H., & Cho, G. H. (2014). A DC-DC converter for a fully integrated PID compensator with a single capacitor. *IEEE Transactions on Circuits and Systems II: Express Briefs*, *61*(8), 629–633. https://doi.org/10.1109/TCSII.2014.2327351

Pattathu, R. L., Subhransu, S., & Rajat, K. D. (2020). Design and Implementation of Perturb & Observe MPPT Algorithm under Partial Shading Conditions (PSC) for DC-DC Boost Converter by Simulation analysis. *IEEE Xplore*, *2020*, 1–80.

Pavan Singh Tomar, Ashok Kumar Sharma, & Kanak Hada. (2018). Energy Storage in DC Microgrid System Using Non-Isolated Bidirectional Soft-Switching DC/DC Converter. *IEEE*, *1*(2018), 1–89.

Pavan Singh Tomar, Manaswi Srivastava, & Arun Kumar Verma. (2018). An Efficient Bi-directional DC/DC Charger for Electric Vehicle Battery Charging. *IEEE*, *1*(2018), 1–80.

Premkumar, M., Sowmya, R., Umashankar, S., & Pradeep, J. (2020). An Effective Solar Photovoltaic Module Parameter Estimation Technique for Single-Diode Model. *IOP Conference Series: Materials Science and Engineering*, *937*(1). https://doi.org/10.1088/1757-899X/937/1/012014

Putri, R. I., Nata, S., & Priyadi, B. (2022). Battery charging control using photovoltaic with sepic converter. In *International Journal of Frontier Technology and Engineering (IJFTE)* (Vol. 01, Issue 01). http://jurnal.polinema.ac.id/index.php/IJFTE/index

R. D. Bhagiya, & R. M. Patel. (2019). PWM based Double loop PI Control of a Bidirectional DC-DC Converter in a Standalone PV/Battery DC Power System. *IEEE*, *1*(2019), 1–80.

Radosavljević, J., Jevtić, M., & Klimenta, D. (2016). Energy and operation management of a microgrid using particle swarm optimization. *Engineering Optimization*, *48*(5), 811–830. https://doi.org/10.1080/0305215X.2015.1057135

Rajvir Kaur. (2020). Mathematical Modelling of Buck Converter. *IEEE*, *2*(5), 1–80.

Ramos-Paja, C. A., Gonzalez Montoya, D., & Bastidas-Rodríguez, J. D. (2020). Sliding-mode control of a CuK converter for voltage regulation of a dc-bus. *Sustainable Energy Technologies and Assessments*, *42*. https://doi.org/10.1016/j.seta.2020.100807

Santra, S., Chatterjee, D., & Liang, T. J. P. (2021). High Gain and High-Efficiency Bidirectional DC-DC Converter with Current Sharing Characteristics Using Coupled Inductor. *IEEE Transactions on Power Electronics*, *36*(11), 12819–12833. https://doi.org/10.1109/TPEL.2021.3077584

Sathishkumar, S., Preethi, G., & Kamatchi Kannan, V. (2020). An Overview of Different Topologies of DC/DC Bidirectional Converter for Different Applications. *Smart Innovation, Systems and Technologies*, *169*, 721–730. https://doi.org/10.1007/978-981-15-1616-0_70

Satyam Kumar Singh, Anand Kumar, & Pradip Kumar Sadhu. (2019). A novel instantaneous mode switching Bi-directional dc-dc converter for dc grid voltage control. *IEEE*, *1*(2019), 1–100.

Senapati, M. K., Pradhan, C., Samantaray, S. R., & Nayak, P. K. (2019). Improved power management control strategy for renewable energy-based DC micro-grid with energy storage integration. *IET Generation, Transmission and Distribution*, *13*(6), 838–849. https://doi.org/10.1049/iet-gtd.2018.5019

Shivendra Singh. (2020). Implementation of Perturb & Observe MPPT Technique using Boost converter in PV System. *IEEE*, *1*(3), 1–70.

Shreelakshmi M. P, & Moumita Das and Vivek Agarwal. (2014). High Gain, High Efficiency Bi-Directional DC-DC Converter for Battery Charging Applications in Stand-Alone Photo-Voltaic Systems. *IEEE*, *1*(2024), 1–90.

Sulligoi, G., Bosich, D., Giadrossi, G., Zhu, L., Cupelli, M., & Monti, A. (2014). Multiconverter medium voltage DC power systems on ships: Constant-power loads instability solution using linearization via state feedback control. *IEEE Transactions on Smart Grid*, *5*(5), 2543–2552. https://doi.org/10.1109/TSG.2014.2305904

Taguchi, M., Suzuki, A., Ueoka, N., & Oku, T. (2019). Effects of poly(methyl methacrylate) addition to perovskite photovoltaic devices. *AIP Conference Proceedings*, *2067*. https://doi.org/10.1063/1.5089451

Tang, L., Wang, X., Xu, W., Mu, C., & Zhao, B. (2021). Maximum power point tracking strategy for photovoltaic system based on fuzzy information diffusion under partial shading conditions. *Solar Energy*, *220*, 523–534. https://doi.org/10.1016/j.solener.2021.03.047

Vieira, R. G., de Araújo, F. M. U., Dhimish, M., & Guerra, M. I. S. (2020). A comprehensive review on bypass diode application on photovoltaic modules. In *Energies* (Vol. 13, Issue 10). MDPI AG. https://doi.org/10.3390/en13102472

W.J. Gil-Gonzalez. (2019). Output Voltage Regulation For dc–dc Buck Converters: a Passivity–Based PI Design. *IEEE*, *1*(2019), 1–90.

Yuan, X., Xiang, Y., & He, Y. (2014). Parameter extraction of solar cell models using mutative-scale parallel chaos optimization algorithm. *Solar Energy*, *108*, 238–251. https://doi.org/10.1016/j.solener.2014.07.013

Zhao, Z., Cheng, R., Yan, B., Zhang, J., Zhang, Z., Zhang, M., & Lai, L. L. (2020). A dynamic particles MPPT method for photovoltaic systems under partial shading conditions. *Energy Conversion and Management*, *220*. https://doi.org/10.1016/j.enconman.2020.113070

APPENDIXES

Appendix A1: Simulink model of various shading pattern

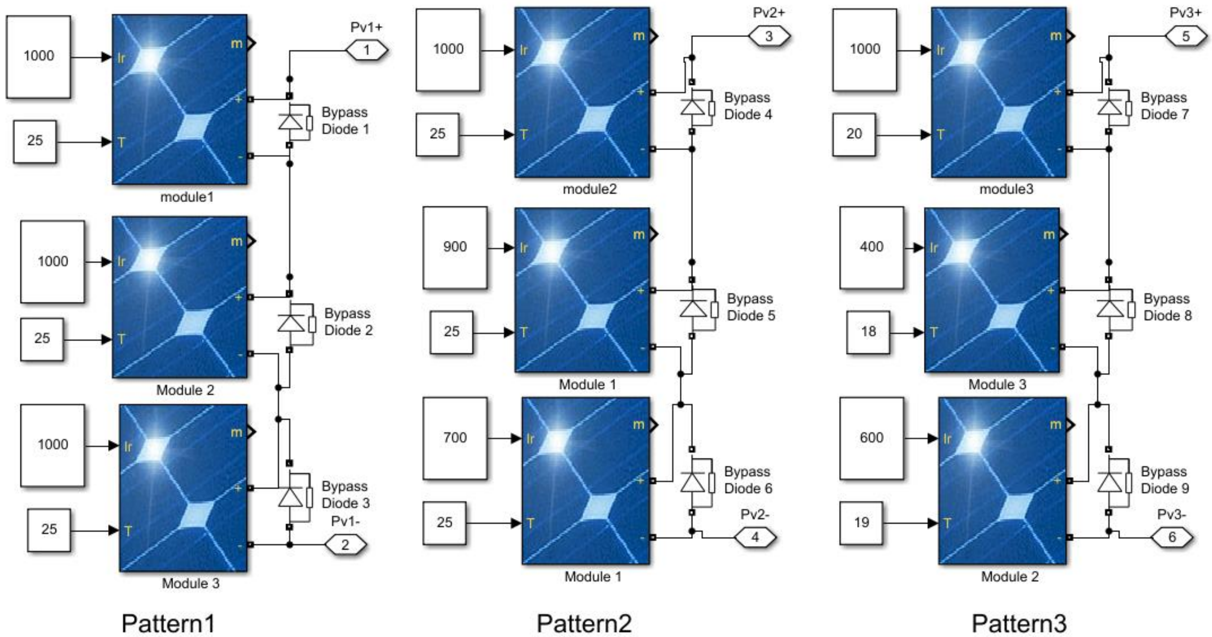

Appendix A2: Simulink model of INC

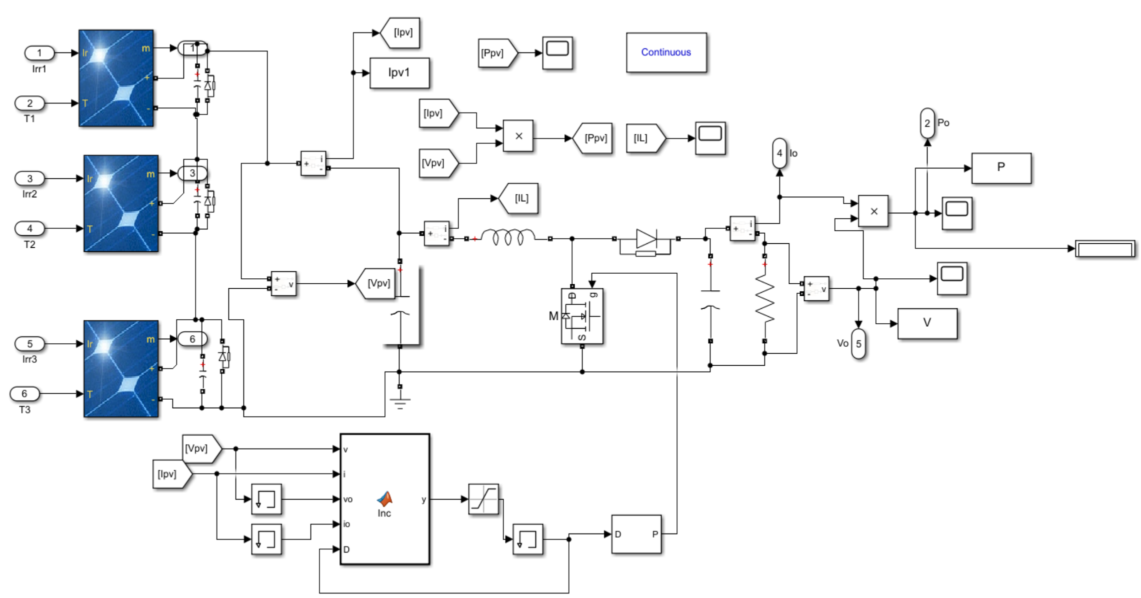

Appendix A3: Simulink model of P&O

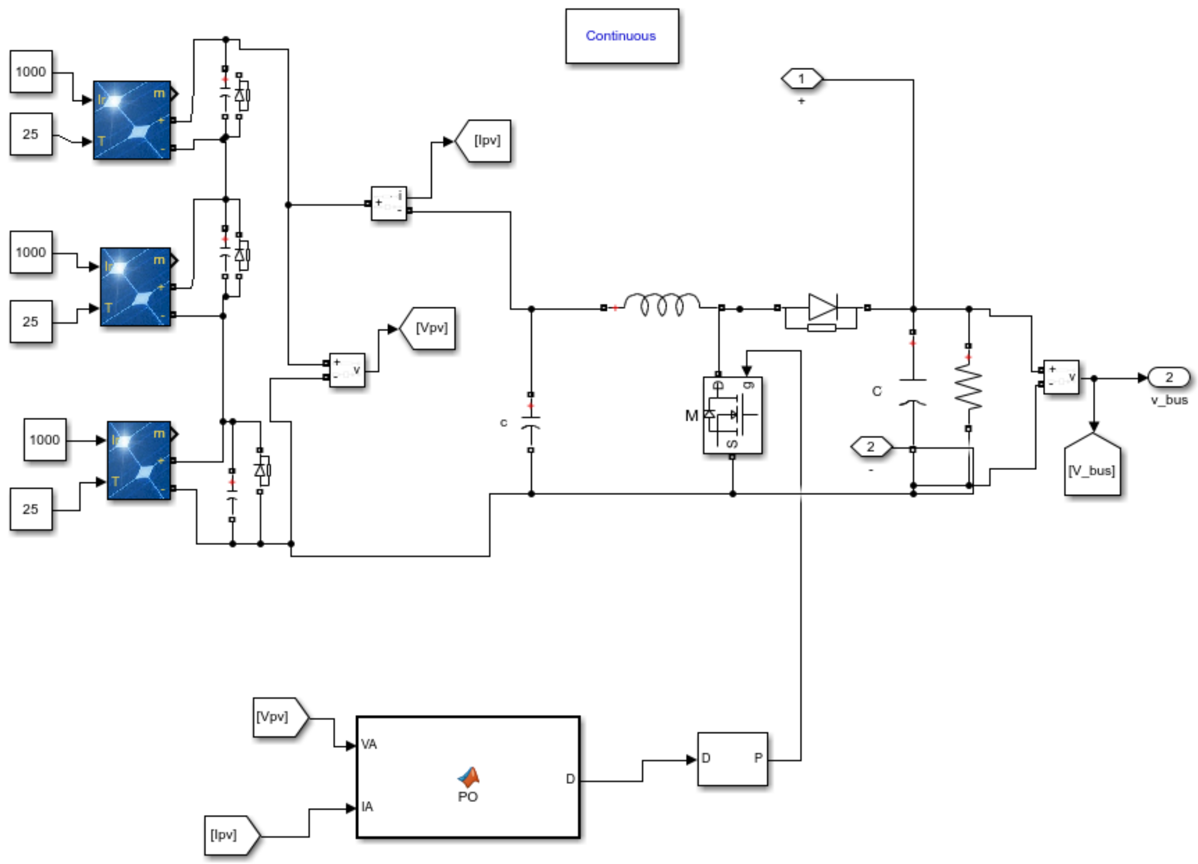

Appendix A4: Simulink model of GWO

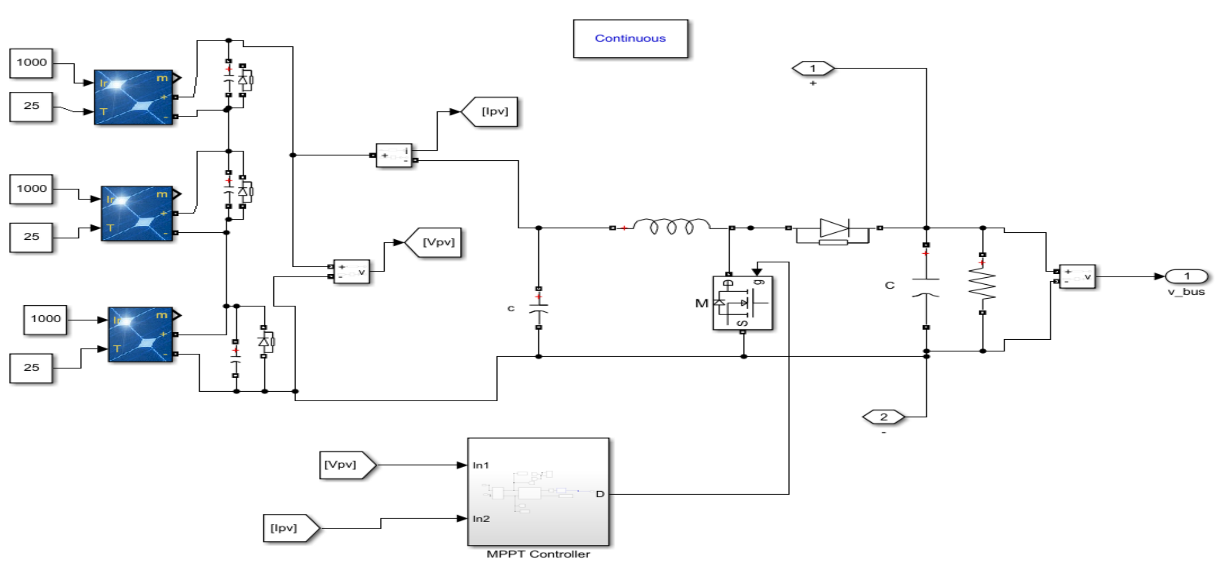

Appendix A5: Simulink diagram of PVsystem with battery

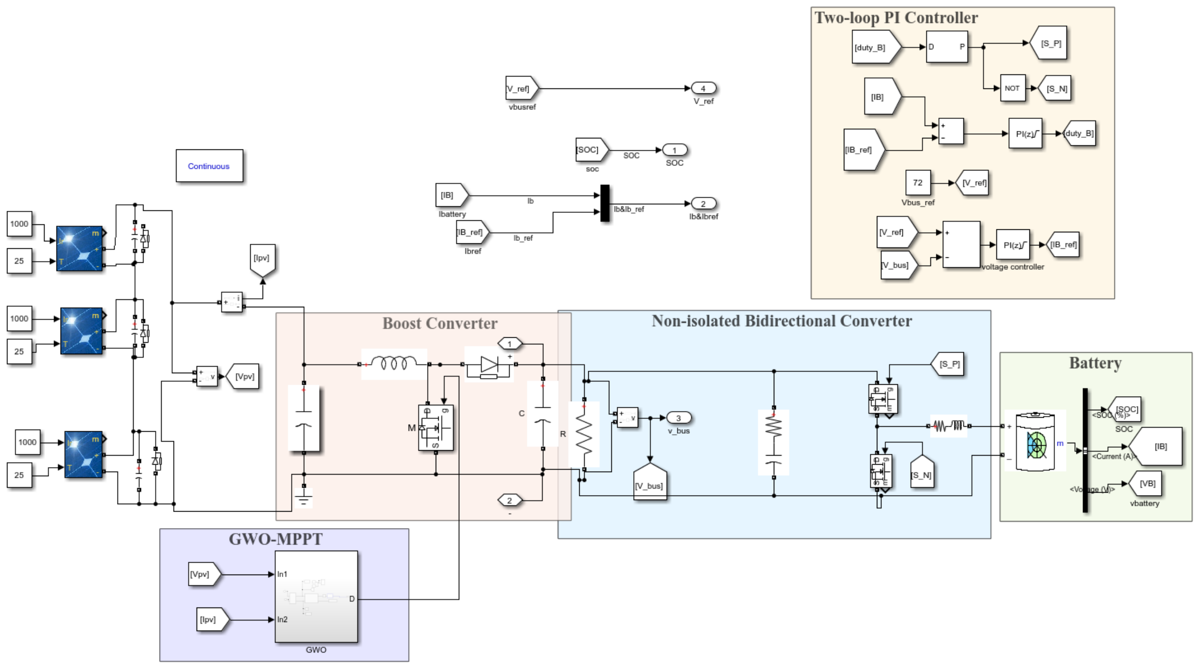

Appendix B1

MATLAB code

rng default options = optimoptions('particleswarm'); options. PlotFcn= 'pswplotbestf'; options.MaxIterations= 100;nvar= 2; LB= [-1000 1000]; UB= [10000 10000]; [x,fval]= particleswarm(@EvalObj_PSOPI1D,nvar,LB,UB,options) function J= EvalObj_PSOPI1D(x) Kp= x(1); Ki= x(2);s=tf('s'); Gbuck=5.4e10/(s^2+6.51e5*s+5.5e10) Gc= Kp+Ki/s G= feedback (Gbuck*Gc,1)t=0:0.01:4;r=1;y=step(Gpl,t)e=abs(ry);J=0.5*h*(e(1)+2*sum(e(2:end-1))+e(end)); plot(t,y,'r')stepinfo(y)endrngdefaultoptions = optimoptions('particleswarm'); options.PlotFcn= 'pswplotbestf';options.MaxIterations= 100;nvar= 2;LB= [-100 0]; UB= [1000 10000];

[x,fval]=particleswarm(@E_PSO_PI,nvar,LB,UB,options)

function J= E_PSO_PI(x)Kp= x(1); Ki= x(2);Cdc=100*10^-6;;Lb=120*10^-6;Zdc=0.015;X2=60;Vb=36;

D=0.5;X1=Vb/(((1-D)^2)*Zdc);
s=tf('s')num=(Zdc*Cdc*X2)*s+X2+(1-D)*Zdc*X1;
den=(Zdc*Cdc*Lb)*s^2+Lb*s+Zdc*(1-D)^2;
Gid=num/den
Gc= Kp+Ki/s
G= feedback(Gid*Gc,1)

```
h= 0.01; t= 0:h:40; r= 1;
y= step(G,t)
e= abs(r-y);
J= 0.5*h*(e(1)+2*sum(e(2:end-1))+e(end));
plot(t,y,'r')
stepinfo(y)
end
rng default
options = optimoptions('particleswarm');
options.PlotFcn= 'pswplotbestf';
options.MaxIterations= 100;
nvar= 2;
LB= [-10000 -100];
UB= [1000 100000];
[x,fval]= particleswarm(@E_PSO_PI,nvar,LB,UB,options)
function J= E_PSO_PI(x)
Kp= x(1); Ki= x(2);
Cdc=100*10^-6;;Lb=120*10^-6;Zdc=0.015;X2=60;Vb=36;
 D=0.5;X1=Vb/(((1-D)^2)*Zdc);
 s=tf('s');
num1=(X2*(1-D)*Zdc);
den1=(X2*Zdc*Cdc)*s+X2+(1-D)*X1*Zdc;
Gvi=num1/den1
Gc= Kp+Ki/s;
Gv= feedback(Gvi*Gc,1);
h= 0.01; t= 0:h:40; r= 1;
y= step(Gv,t);
e= abs(r-y);
J= 0.5*h*(e(1)+2*sum(e(2:end-1))+e(end));
stepinfo(y)
end

function out= GWOMPPT_mf(A,P)persistent Alfa_pstn Betapstn Deltapstn a A1 A2 A3 C1
C2 C3 X1 X2 X3 Dofalfa Dofbeta Dofdelta Flag4ub Flag4lb Nexi NexiOld f Stab
mean_power Reg c Cycle  MaxCycle Pbest  pass fin test
PN dc dc_Fitness Alfascore Betscore Deltscore...
   w c1 c2 r1 r2 Xmin Xmax...
   D Partical_Best_Fittnness Global_best_position Global_best_fittnness;
dataType = 'double';
if ACT==0 || fin==1 Nexi=0;NexiOld=0;
   f=0; Reg=1;
   Cycle=1;
   Pbest=zeros(1,5);
   pass=0;
   test=0;
   mean_power=-inf;c=0;
```

```
end

if ACT==0 clc
   save=1;
   robustness=0;
end
if ACT==0 || fin==1
Stab=1;
MaxCycle=30;PN=6; dc=zeros(1,PN);
dc_Fittnness=zeros(1,PN);

Alfa=0;
Betscore=0;
Deltscore=0;
Alfapstn=0;
Betapstn=0;
Deltapstn=0;
r1=rand;
r2=rand;
Xmin=0.05;
Xmax=0.95;
dc=Xmin + rand(1,PN)*(Xmax-Xmin);
fin=0;
end
Nexi=Nexi+1;
if NexiOld==0
   f=1;
else
   f=0;
end
if Nexi== (NexiOld+Stab+f)
   NexiOld=Nexi;
   Reg=Reg+1;
end
if Reg<=PN && Cycle==1
   D=dc(1,Reg);
end
if Reg>1 && Reg<=PN+1 && Nexi== NexiOld && Cycle==1
   dc_Fitness(1,Reg-1)=P;
end
if Reg==PN+1 && Nexi== NexiOld && Cycle==1
  for i=1:PN
       if dc_Fittnness(1,i)>Alfa
          Alfa=dc_Fittnness(1,i);
          Alfapstn=dc(1,i);
       end
```

```
        if dc_Fittnness(1,i)<Alfa && dc_Fittnness(1,i)>Betscore
            Betscore=dc_Fittnness(1,i);
            Betapstn=dc(1,i);
        end

        if dcFittnness(1,i)<Alfa && dc_Fitness(1,i)<Bet && dc_Fitness(1,i)>Delt
            Delt=dc_Fittnness(1,i);
            Deltpstn=dc(1,i);
        end
 end        a=2-Cycle*((2)/MaxCycle);
 for i=1:PN

            r1,  r2 = rnd;

            A1=2*a*r1-a;            C1=2*r2;
            Dofalfa=abs(C1*Alfapstn-dc(1,i));
            X1=Alfapstn-A1*Daoflfa;
            r1=rnd;
            r2=rnd
            A2=2*a*r1-a; C2=2*r2
            Dofbeta=abs(C2*Betapstn-dc(1,i));
            X2=Betpstn-A2*Dofbeta;

            r1=rnd;
            r2=rnd;

            A3=2*a*r1-a; C3=2*r2
            Dofdelta=abs(C3*Deltapstn-dc(1,i));
            X3=Deltpstn-A3*Dofdelta;
            dc(1,i)=(1/3)*(X1+X3+X2)
                  Flag4ub=dc(1,i)>Xmax;
                  Flag4lb=dc(1,i)<Xmin;
dc(1,i)=(dc(1,i).*(~(Flag4ub+Flag4lb)))+Xmax.*Flag4ub+Xmin.*Flag4lb;
 end
end
if Cycle<=MaxCycle

if Reg>=PN+1 && Reg<=2*PN
    D=dc(1,Reg-PN);
end
if Reg>PN+1 && Reg<=(2*PN)+1 && Nexi== NexiOld
    dc_Fitness(1,Reg-PN-1)=P;
end

if Reg==(2*PN)+1 && Nexi== NexiOld
for i=1:PN
        if dc_Fittnness(1,i)>Alfa
```

```
            Alfa=dc_Fittnness(1,i);
            Alfapostn=dc(1,i);
        end

        if dc_Fittnness(1,i)<Alfa&& dc_Fitness(1,i)>Beta
            Beta=dc_Fitness(1,i);
            Betpstn=dc(1,i);
        end

        if dc_Fittnness(1,i)<Alfa&& dc_Fitness(1,i)<Beta && dc_Fittnness(1,i)>Delta
            Delta=dc_Fittnness(1,i);
            Deltpstn=dc(1,i);
        end
end
    a=2-Cycle*((2)/MaxCycle);
for i=1:PN
            r1=rnd;
            r2=rnd;

            A1=2*a*r1-a;
            C1=2*r2;

            Dofalfa=abs(C1*Alfapstn-dc(1,i));
            X1=Alfapstn-A1*Dofalfa;

            r1  r2 = rnd;
            =rnd
            A2=2*a*r1-a;
            C2=2*r2;

            Dofbeta=abs(C2*Betapstn-dc(1,i));
            X2=Betpstn-A2*D_beta;

            r1=rnd
            r2=rnd

            A3=2*a*r1-a;
            C3=2*r2;

            Dofdelta=abs(C3*Deltpstn-dc(1,i));
            X3=Deltpstn-A3*D_delta;

            dc(1,i)=(X1+X3+X2)/3;

                Flag4ub=dc(1,i)>Xmax;
                Flag4lb=dc(1,i)<Xmin;
                dc(1,i)=(dc(1,i).*(~(Flag4ub+Flag4lb)))+Xmax.*Flag4ub+Xmin.*Flag4lb;
```

```
 end
Reg=PN;
D=Alfapstn;

Cycle=Cycle+1;
Pbest(1,1:4)=Pbest(1,2:5);
Pbest(1,5)=Alpha_score;
STD=std(Pbest);
mean_power=mean(Pbest);

if (Cycle>=MaxCycle || STD<=0.5)
    pass=0;
    Cycle=MaxCycle+1;
    D=Alfapstn;
    STD=100;
    c=1;
end
end
end test=(P-mean_power)/mean_power;

if (test>0.1 || test<-0.1) && c==1 && pass>=5
    fin=1;
end
pass=pass+1;
out=D;

end
```